Universität Hamburg
DER FORSCHUNG | DER LEHRE | DER BILDUNG

CHyN
Centre for Hybrid Nanostructures

Microcapsule-Mediated Delivery Platform for Independent Investigations of Intracellular Nanodrugs Diffusion Kinetics and Nanoplastic Biodegradation

Dissertation

zur Erlangung des Doktorgrades

and der Fakultät für Mathematik, Informatik und Naturwissenschaften

Fachbereich Physik

Der Universität Hamburg

vorgelegt von

Xin Liu

Hamburg

2025

Gutachter/innen der Dissertation: (Supervisor)	Prof. Dr. Wolfgang J. Parak Prof. Dr. Dorota Koziej
Zusammensetzung der Prüfungskommission: (Examination Board)	Prof. Dr. Wolfgang J. Parak Prof. Dr. Dorota Koziej Prof. Dr. Wolfgang Streit Prof. Dr. Gabriel Bester Dr. Florian Schulz
Vorsitzende/r der Prüfungskommission: (Head of Examination Board)	Prof. Dr. Dorota Koziej
Datum der Disputation: (Date of Disputation)	09.07.2025
Vorsitzender des Fach-Promotionsausschusses PHYSIK: (Chairman of the Doctoral Committee Physics)	Prof. Dr. Wolfgang J. Parak
Leiter des Fachbereichs PHYSIK: (Chairman of the Faculty Physics)	Prof. Dr. Markus Drescher
Dekan der Fakultät MIN: (Dean of the MIN-Faculty)	Prof. Dr.-Ing. Norbert Ritter

Eidesstattliche Versicherung

Hiermit versichere ichEides statt, die vorliegende Dissertationsschrift selbst verfasst und keine anderen als die angegebenen Hilfsmittel und Quellen benutzt zu haben.

Sofern im Zuge der Erstellung der vorliegenden Dissertationsschrift generative Künstliche Intelligenz (gKI) basierte elektronische Hilfsmittel verwendet wurden, versichere ich, dass meine eigene Leistung im Vordergrund stand und dass eine vollständige Dokumentation aller verwendeten Hilfsmittel gemäß der Guten wissenschaftlichen Praxis vorliegt. Ich trage die Verantwortung für eventuell durch die gKI generierte fehlerhafte oder verzerrte Inhalte, fehlerhafte Referenzen, Verstöße gegen das Datenschutz- und Urheberrecht oder Plagiate.

01.04.2025 Xin Liu

Datum Unterschrift der Doktorandin / des Doktoranden

I. Table of Contents

II. List of Publications

Published manuscripts

[1] Ahmed, A. A., Alegret, N., Almeida, B., Alvarez-Puebla, R., Andrews, A. M., Ballerini, L., ... **Liu, X.,** ... & Parak, W. J. (2025). Interfacing with the Brain: How Nanotechnology Can Contribute. *ACS nano*, *19*(11), 10630-10717.

[2] Zhang, J., Werner, S., Köppen, A., **Liu, X.,** Shen, C., Bertram, F., ... & Sun, X. (2024). Unraveling the synthesis and assembly of gold-iron oxide hybrid nanoparticles. *Nano Today*, *57*, 102384.

[3] Chen, L., Klemeyer, L., Ruan, M., **Liu, X.,** Werner, S., Xu, W., ... & Chakraborty, I. (2023). Structural Analysis and Intrinsic Enzyme Mimicking Activities of Ligand-Free PtAg Nanoalloys. *Small*, *19*(19), 2206772.

Submitted manuscripts

[1] Xin Liu, Jennifer Chow, Wenbo Wang, Robert Dierkes, Neus Feliu, Florian Schulz, Wolfgang Streit*, Wolfgang J. Parak*. Enzyme-loaded microcapsules as intracellular organelles for the degradation of nanoplastics by cells. *Advanced materials*, under review.

Manuscripts in preparation

[1] Xin Liu‡, Fusheng Zhang‡, Florian Schulz, Neus Feliu, Wolfgang J. Parak*. An intriguing polymeric modification strategy for solid nanoparticles to investigate endosomal escape of cargos from polyelectrolyte microcapsule.

III. List of Figures

IV. List of Tables

V. List of Abbreviations

AA	Ascorbic acid
$AgNO_3$	Silver nitrate
AIBN	2,2′-Azobis(2-methyl-propionitrile)
APDs	Avalanche photodiodes
A_{ROI}	Area of the region of interest
ATT	6-Aza-2-thiothymine
Au NC	Gold nanoclusters
Au NPs	Gold Nanoparticles
BSA	Bovine serum albumin
FITC	Fluorescein Isothiocyanate
$CaCl_2 \cdot 2H_2O$	Calcium chloride dihydrate
$CaCO_3$	Calcium carbonate
caps	Polyelectrolyte microparticles
CHT	Chitosan
CLSM	Confocal laser scanning microscopy
CNP	Nanoparticle concentration
ddH_2O	Ultrapure double distilled water
DEXS	Dextran sulfate sodium salt
DLS	Dynamic light scattering
DMEM	Dulbecco's Modified Eagles Medium
DS	Dextran sulfate
EDC	N-(3-Dimethylaminopropyl)-N′-ethylcarbodiimide hydrochloride
EDTA	Ethylenediamine-tetra-acetic acid
EG	Ethylene glycol
EPR	Enhanced permeability and retention
FBS	Fetal bovine serum
Fe_2O_3	Maghemite
Fe_3O_4	Magnetite
fs	Femtosecond
$FeSO_4 \cdot 7H_2O$	Iron(II) sulfate heptahydrate
FTIR	Fourier transformed infrared

GNPs	Gold nanoparticles
GNSs	Gold nanostars
H_2O_2	Hydrogen peroxide
HA	Hyaluronic acid
$HAuCl_4 \cdot 3H_2O$	Gold(III) chloride trihydrate
HCl	Hydrochloric acid
HFIP	Hexafluoroisopropanol
HNO_3	Nitric acid
HOTP	2-hydroxyterephthalate
IRB	Rhodamine B (RB) fluorescence intensity
itp	Include toplogy
KH_2PO_4	Potassium phosphate monobasic
LbL	Layer-by-layer
LSPR	Longitudinal surface plasmon resonance
$M(HET)_2$	Methyl bis(2-hydroxyethyl terephthalate)
$M(HET)_3$	Methyl tris(2-hydroxyethyl terephthalate)
MD	Molecular dynamics
MF	Melamine formaldehyde
MNPs	Micro- and nanoplastics
MS	Mesoporous silica
Na_2CO_3	Sodium carbonate
Na_2HPO_4	Sodium phosphate dibasic
$NaBH_4$	Sodium borohydride
NaCl	Sodium chloride
nano–bio	Nanoparticle–biological
NaOH	Sodium hydroxide
$N_{caps/cell}$	Capsule-to-cell ratio
NDD	Non-descanned detection
NHS	N-hydroxysuccinimide
NIR	Near-infrared
NPs	Nanoparticles
P/S	Penicillin/streptomycin
PAA	Polyacrylic acid

PAH	Poly(allylamine hydrochloride)
PAMAM	Poly(amidoamine)
PARG	Poly-L-arginine hydrochloride
PB	Phosphate buffer
PBS	Phosphate buffered saline
PDADMAC	Polydimethyldiallylammonium chloride
PDMS	Poly(dimethylsiloxane)
PEG	Poly(ethylene glycol)
PEI	Poly(ethylenimine)
PET	Polyethylene terephthalate filament
PET NPs	Polyethylene terephthalate nanoparticles
PI-b-PEG	Amphiphilic diblock copolymers polyisoprene-block-poly(ethylene oxide)
PLA	Polylactic acid
PLL	Poly-L-lysine
PMTs	Photomultiplier tubes
PNIPAAm	Poly(N-isopropylacrylamide)
PS beads	Polystyrene fluorophores
PSS	Poly(sodium 4-styrenesulfonate)
PVCL	Poly(vinyl caprolactam)
PVP	Polyvinylpyrrolidone
PVS	Polyvinyl siloxane
Q	Overall delivery efficiency
QA	Delivery efficiency of accumulation
QC	Delivery efficiency of circulation
QDs	Quantum dots
QEq	Charge equalization
QI	Delivery efficiency of internalization
QP	Delivery efficiency of penetration
QR	Delivery efficiency of drug release
RB	Rhodamine B
RES	Reticuloendothelial system
ROI	Region of interest

RT	Room temperature
SD	Standard deviations
SEM	Scanning electron microscope
SPR	Surface plasmon resonance
TA	Thioctic acid
TEM	Transmission electron microscope
THF	Tetrahydrofuran
TPA	Terephthalic acid
TPEM	Two-photon excitation microscopy

VI. Acknowledgments

I am profoundly grateful to my esteemed supervisor, Prof. Dr. Wolfgang J. Parak, for the extraordinary privilege of joining his distinguished research group. Your exceptional mentorship has not only cultivated my skills in rigorous scientific inquiry but has fundamentally shaped my capacity for critical analysis and deep conceptual thinking. The countless hours you invested in guiding me through iterative revisions and late-night discussions represent an intellectual debt I can never fully repay. The research philosophy and methodologies I have acquired in the Parak group will undoubtedly serve as enduring foundations for my academic career.

My sincere appreciation extends to Dr. Florian Schulz for his generous intellectual engagement and thought-provoking dialogues that consistently expanded my scientific horizons. I am particularly indebted to Prof. Dr. Wolfgang Streit and Dr. Jennifer Chow for their expert contributions regarding enzymatic systems, which proved pivotal to this research. The foundational guidance provided by Prof. Dr. Indranath Chakraborty, Prof. Dr. Dingcheng Zhu, and Dr. Lizhen Chen during my initial transition into the laboratory environment was instrumental to my professional development.

I would like to acknowledge Dr. Gerwin Chilla, Marten Rittner, and Yang Ye for their technical assistance and scientific discussions.

I am indebted to Jinrui, Yuxuan, and Jili for their help with ICP measurements, Kaiwei for SEM imaging, and Stefan Werner for TEM imaging. My thanks also go to Prof. Dr. Shahin and Dr. Hessam for their valuable advice and support in cell-based experiments.

To my dear friends, Wenbo, Dr. Fusheng, Dr. Ruixia, and Prof. Dr. Min Lin, I am deeply thankful for the inspiring discussions and intellectual exchanges we shared. I also extend my warmest appreciation to my friends and colleagues, Dr. Miao, Dr. Chenxi, Dr. Juan, Shihao, Ben, Martin, Sarodi, Maya, …, for bringing joy and camaraderie to my scientific journey.

I owe my deepest gratitude to my beloved parents and family for their unconditional love and support. I also acknowledge the Guangzhou Elite Program for its financial backing, which made this research possible.

In closing, I express my profound appreciation to Germany for hosting my academic journey.

VII. Vita

2017 Bachelor of Science in Biomedical Engineering, Jinan University

2020 Master of Science in Biomedical Engineering, Jinan University

2025 Doctor of Philosophy in Physics, University of Hamburg

Abstract

This study presents a groundbreaking microcapsule-mediated delivery platform that addresses two critical challenges in cellular nanomaterial engineering: (i) strategies for enhancing intracellular transport kinetics of rigid nanoparticles following endosomal escape, and (ii) development of biodegradation approaches for internalized environmental nanoplastics. By employing layer-by-layer (LbL) assembled polyelectrolyte capsules with stimuli-responsive release capabilities (photothermal or pH-triggered), we have established a robust spatiotemporal control system for nanodrug delivery while simultaneously enabling enzymatic degradation of plastic particulates within endolysosomal compartment.

On one hand, we systematically investigated the cytoplasmic diffusion behavior of rigid nanoparticles (core diameter: 1.5-100 nm) following photoinduced release from microcapsules. High-resolution confocal laser scanning microscopy (CLSM) with superior temporal resolution revealed four significant findings regarding intracellular transport: (a) PEGylation effects: Compared to non-PEGylated rigid nanoparticles, those with PEG coatings exhibited markedly enhanced diffusion, as confirmed by molecular dynamics simulations demonstrating stronger interaction forces between PEG-coated nanoparticles and water molecules; (b) Size-dependent transport characteristics: Smaller nanoparticles displayed significantly greater diffusion capacity than their larger counterparts; (c) Terminal group chemistry: Experimental results demonstrated that methoxy-terminated PEG coatings facilitated faster diffusion compared to carboxyl-terminated equivalents; (d) Co-loading phenomenon: Calcein co-encapsulation within the capsules enhanced nanoparticle-water interactions through unstable calcein-mediated binding, suggesting that calcein-doped PEGylated nanoparticles could overcome low diffusion performance. Consequently, calcein-mediated PEGylated nanoparticle delivery may represent a potential solution to the cytosolic delivery bottleneck, enhancing intracellular release of nanoparticles from endosomes to target sites and further improving nanoparticle delivery efficiency.

On the other hand, we demonstrated that enzyme-loaded capsules (PETase@caps) can effectively degrade internalized PET nanoparticles, providing proof-of-concept for cellular-level plastic clearance. The capsule-based system enabled enzyme enrichment and intracellular delivery, achieving co-localization of enzymes and plastic nanoparticles within endolysosomal compartments. The PEI-mediated proton buffering effect

successfully neutralized the acidic lysosomal environment, facilitating intracellular plastic nanoparticle degradation. These findings suggest the potential for translating this plastic degradation capability into cellular systems.

Zusammenfassung

Diese Studie stellt eine bahnbrechende, mikrokapselvermittelte Lieferplattform vor, die zwei kritische Herausforderungen in der zellulären Nanomaterialtechnik adressiert: (i) Strategien zur Verbesserung der intrazellulären Transportkinetik starrer Nanopartikel nach dem endosomalen Entkommen und (ii) die Entwicklung von Biodegradationsansätzen für internalisierte Umwelt-Nanoplastikpartikel. Durch den Einsatz von Schicht-für-Schicht (LbL) assemblierten Polyelektrolytkapseln mit stimuli-responsiven Freisetzungsfähigkeiten (photothermisch oder pH-getriggert) haben wir ein robustes raumzeitliches Kontrollsystem für den Nanowirkstofftransport etabliert, das gleichzeitig die enzymatische Degradation von Plastikpartikeln im endolysosomalen Kompartiment ermöglicht.

Einerseits untersuchten wir systematisch das zytoplasmatische Diffusionsverhalten starrer Nanopartikel (Kerndurchmesser: 1,5-100 nm) nach der photoinduzierten Freisetzung aus Mikrokapseln. Hochauflösende konfokale Laser-Scanning-Mikroskopie (CLSM) mit überlegener zeitlicher Auflösung enthüllte vier bedeutende Erkenntnisse zum intrazellulären Transport: (a) PEGylierungseffekte: Im Vergleich zu nicht-PEGylierten starren Nanopartikeln zeigten PEG-beschichtete Nanopartikel eine deutlich verbesserte Diffusion, was durch Molekulardynamiksimulationen bestätigt wurde, die stärkere Wechselwirkungskräfte zwischen PEG-beschichteten Nanopartikeln und Wassermolekülen demonstrierten; (b) Größenabhängige Transporteigenschaften: Kleinere Nanopartikel wiesen eine signifikant größere Diffusionskapazität auf als ihre größeren Gegenstücke; (c) Endgruppenchemie: Experimentelle Ergebnisse zeigten, dass methoxy-terminierte PEG-Beschichtungen eine schnellere Diffusion ermöglichten als carboxy-terminierte Äquivalente; (d) Co-Loading-Phänomen: Die Co-Encapsulation von Calcein in den Kapseln verstärkte die Nanopartikel-Wasser-Wechselwirkungen durch instabile Calcein-vermittelte Bindungen, was darauf hindeutet, dass Calcein-dotierte PEGylierte Nanopartikel die geringe Diffusionsleistung überwinden könnten. Folglich könnte die Calcein-vermittelte PEGylierte Nanopartikel-Lieferung eine potenzielle Lösung für den zytosolischen Lieferengpass darstellen, indem sie die intrazelluläre Freisetzung von Nanopartikeln aus Endosomen zu Zielorten verbessert und die Nanopartikel-Liefereffizienz weiter steigert.

Andererseits zeigten wir, dass enzymbeladene Kapseln (PETase@caps) internalisierte PET-Nanopartikel effektiv abbauen können, was einen

Machbarkeitsnachweis für die plastikabbauende Wirkung auf Zellebene liefert. Das kapselbasierte System ermöglichte eine Enzymanreicherung und intrazelluläre Lieferung, wodurch eine Kolokalisation von Enzymen und Plastiknanopartikeln innerhalb endolysosomaler Kompartimente erreicht wurde. Der PEI-vermittelte Protonenpuffereffekt neutralisierte erfolgreich das saure lysosomale Milieu und erleichterte so den intrazellulären Abbau von Plastiknanopartikeln. Diese Ergebnisse deuten auf das Potenzial hin, diese Plastikabbaufähigkeit in zelluläre Systeme zu übertragen.

1 Introduction

1.1 Nanodrugs

The targeted delivery of therapeutic agents to specific diseased tissues or cellular compartments is a critical objective in modern diagnostics and treatment strategies [1]. Nanomedicine has emerged as a highly promising platform for the precise delivery of a diverse range of therapeutic and diagnostic agents, including drugs, contrast agents, immunotherapies, and gene-editing tools [2-4]. By leveraging nanotechnology, these delivery systems can be meticulously engineered to exhibit tailored physical and chemical properties, which govern their interactions with biological environments and determine their ultimate delivery destinations [5, 6]. This capability enables nanotechnology to address the inherent limitations of conventional drug delivery systems, such as poor bioavailability, non-specific distribution, and suboptimal cellular uptake, by facilitating the transport of cell-specific targeting molecules to precise organelles or tissues [7, 8].

Nanodrugs represent a significant and rapidly advancing frontier in the field of modern drug delivery [9, 10]. Within this domain, nanoparticles (NPs) are categorized into multiple subclasses, each with distinct structural and functional characteristics [11, 12]. Among these, several subclasses have garnered substantial attention due to their unique properties and therapeutic potential. These include lipid-based NPs [13], polymeric NPs [14], and inorganic NPs [15], each of which can be further subdivided into specialized categories tailored for specific applications. Each subclass offers unique advantages in terms of biocompatibility, payload capacity, and targeting efficiency, making them indispensable tools in the development of next-generation nanomedicines [16-18].

1.1.1 Lipid-based nanoparticles (NPs)

Lipid-based NPs encompass a diverse array of nanostructures, predominantly characterized by spherical configurations featuring at least one lipid bilayer enveloping an internal aqueous compartment (Figure 1.1) [19]. These NPs are highly regarded as drug delivery systems due to their formulation simplicity, self-assembly properties,

biocompatibility, high bioavailability, and capacity to carry substantial payloads [20-22]. Additionally, their physicochemical properties can be finely tuned to modulate biological interactions, making them the most prevalent class of FDA-approved nanomedicines [23, 24].

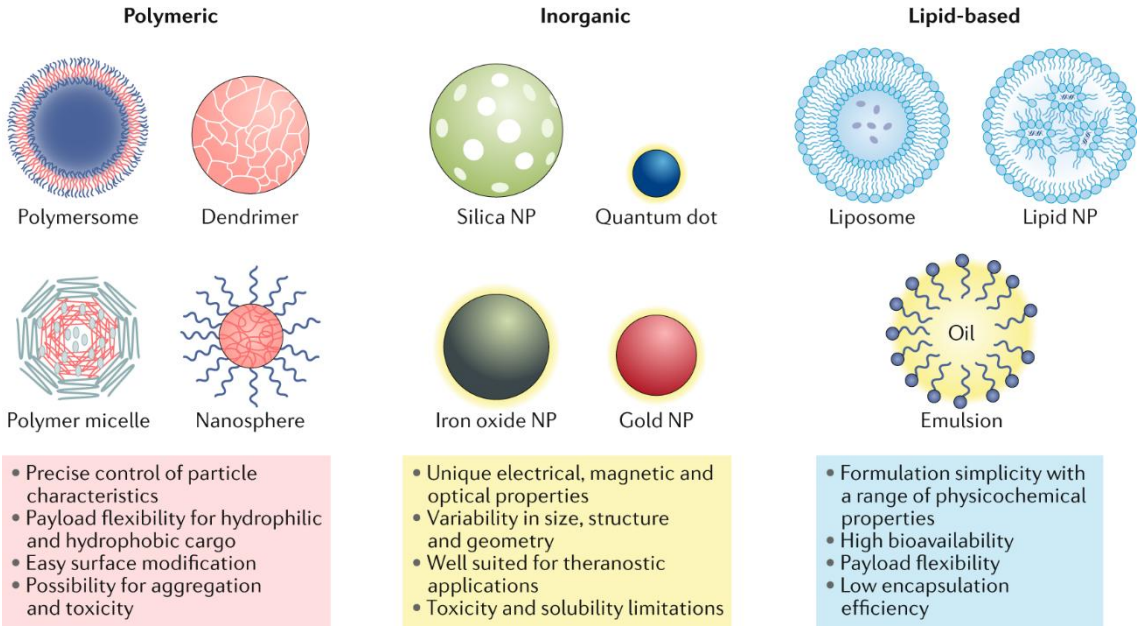

Figure 1.1. Each class of nanoparticle (NP) features multiple subclasses, with some of the most common highlighted here. Each class has numerous broad advantages and disadvantages regarding cargo, delivery, and patient response [19].

Liposomes

Liposomes, a prominent subset of lipid-based NPs, are primarily composed of phospholipids, forming unilamellar or multilamellar vesicular structures. This architecture enables the encapsulation and delivery of hydrophilic, hydrophobic, and lipophilic drugs, often simultaneously within the same system, thereby broadening their therapeutic applications [25, 26]. The stability of liposomes, both in vitro and in vivo, is influenced by factors such as NP size, surface charge, lipid composition, lamellae number, and surface modifications (e.g., ligands or polymers), which can be precisely controlled during synthesis [27-30]. To mitigate rapid uptake by the reticuloendothelial system (RES), liposomes are often surface-modified to prolong circulation time and enhance targeted delivery, facilitating their clinical utility [30, 31].

Lipid nanoparticles (LNPs)

LNPs, another significant subset, are liposome-like structures primarily utilized for nucleic acid delivery parameters [32, 33]. Unlike traditional liposomes, LNPs form micellar structures within their core, a morphology that can be adjusted based on formulation parameters [34, 35]. LNPs typically consist of four key components: (1) cationic or ionizable lipids for complexing with negatively charged genetic material and facilitating endosomal escape, (2) phospholipids for structural integrity, (3) cholesterol for stability and membrane fusion, and (4) PEGylated lipids to enhance stability and circulation [36, 37]. Their efficacy in nucleic acid delivery, coupled with straightforward synthesis, small size, and serum stability, has positioned LNPs as critical tools in personalized genetic therapies [38, 39]. Ionizable LNPs, in particular, exhibit a near-neutral charge at physiological pH but become charged in acidic endosomal environments, promoting intracellular delivery [40]. However, challenges such as low drug loading and preferential biodistribution to the liver and spleen remain limitations [41, 42].

1.1.2 Polymeric nanoparticles (NPs)

Polymeric NPs are synthesized from natural or synthetic materials, including monomers or preformed polymers, enabling a wide range of structures and functionalities (Figure 1.1) [43, 44]. These NPs are highly versatile, offering precise control over physicochemical properties, biocompatibility, and straightforward formulation parameters [14, 45]. Synthesis techniques such as emulsification, nanoprecipitation, ionic gelation, and microfluidics yield NPs with distinct characteristics [46-49]. Polymeric NPs can encapsulate therapeutics within their core, entrap drugs in the polymer matrix, chemically conjugate payloads to the polymer, or bind drugs to the NP surface [50, 51]. This versatility allows for the delivery of hydrophobic and hydrophilic compounds, as well as macromolecules such as proteins, vaccines, and genetic material making them ideal for co-delivery applications [52, 53]. By modulating properties like composition, stability, responsivity, and surface charge, drug loading efficiency and release kinetics can be finely controlled) [11, 54].

Nanocapsules and nanospheres

Polymeric NPs are broadly categorized into nanocapsules (featuring a polymeric shell surrounding a cavity) and nanospheres (solid matrix systems) [55]. Subcategories include polymersomes, micelles, and dendrimers [56]. Polymersomes, composed of amphiphilic block copolymers, resemble liposomes but exhibit enhanced stability and cargo retention, making them effective for cytosolic delivery [57]. Common polymers used include poly(ethylene glycol) (PEG) [58] and poly(dimethylsiloxane) (PDMS) [59]. Polymeric micelles, formed from responsive block copolymers, self-assemble into nanospheres with a hydrophilic core and hydrophobic coating, protecting aqueous drug cargo and extending circulation times. These micelles have been employed in clinical trials for cancer therapeutics [60, 61].

Dendrimers

Dendrimers are hyperbranched polymers with highly controllable mass, size, shape, and surface chemistry [62]. Their exterior functional groups enable conjugation of biomolecules or contrast agents, while drugs can be loaded within their interior. Dendrimers are particularly explored for nucleic acid and small molecule delivery, with charged polymers like poly(ethylenimine) (PEI) and poly(amidoamine) (PAMAM) being commonly used [63-65]. Several dendrimer-based products are in clinical trials for applications such as theranostics, transfection, and contrast imaging [66]. Polyelectrolytes, another class of charged polymers, exhibit pH-dependent charge and are used to enhance bioavailability and mucosal transport [67, 68].

Despite their advantages, polymeric NPs face challenges such as particle aggregation and potential toxicity. While only a limited number of polymeric nanomedicines are FDA-approved, numerous candidates are under clinical investigation [69].

1.1.3 Inorganic nanoparticles (NPs)

Inorganic NPs, synthesized from materials such as gold, iron, and silica, are engineered for drug delivery and imaging applications (Figure 1.1). These NPs exhibit

unique physical, electrical, magnetic, and optical properties, enabling niche applications unattainable with organic materials.

Gold nanoparticles (Au NPs)

Au NPs, the most extensively studied inorganic NPs, are utilized in various forms, including nanospheres, nanorods, nanostars, nanoshells, and nanocages [70, 71]. Their surface plasmon resonance, resulting from oscillating free electrons, confers photothermal properties, making them valuable for imaging and photothermal therapy [72]. Au NPs are also easily functionalized, enhancing their delivery capabilities [73-75].

Iron oxide nanoparticles

Iron oxide NPs, primarily composed of magnetite (Fe_3O_4) or maghemite (Fe_2O_3), exhibit superparamagnetic properties at specific sizes, making them effective as contrast agents, drug delivery vehicles, and thermal-based therapeutics [76]. They constitute the majority of FDA-approved inorganic nanomedicines [77, 78].

Other inorganic NPs

Calcium phosphate and mesoporous silica NPs are also widely used for gene and drug delivery [79]. Quantum dots, typically composed of semiconducting materials like silicon, are primarily employed in in vitro imaging but show promise for in vivo diagnostics [80, 81].

While inorganic NPs offer unique advantages for diagnostics, imaging, and photothermal therapies, their clinical application is limited by low solubility and toxicity concerns, particularly with heavy metal-based formulations [82, 83].

Despite significant advancements in nanomedicine, the efficacy of therapeutic delivery is often compromised by formidable biological systems that impede the therapeutic effect of nanotherapeutic agents at diseased sites [12]. Although substantial research efforts have been directed toward the integration of multifunctional components into nanoparticle design to enhance their delivery capabilities, many of these strategies remain insufficient in overcoming the complex biological challenges inherent in vivo [84]. Understanding the intricate interplay between nanoparticles and biological environments is essential to address these challenges and optimize therapeutic outcomes [6, 85].

1.2 The fate of delivery drugs in biological systems

The primary objective of drug delivery is the delivery of drugs in the form of free molecules into targeted cells, thereby exerting their pharmaceutical effects [13, 86]. Nanoparticle delivery systems undergo a series of complex interactions with various biological components, including molecules, cells, tissues, and organs, as they traverse the body (Figure 1.2) [87, 88]. These interactions, collectively referred to as nanoparticle–biological (nano–bio) interactions, critically determine the fate and behavior of nanomaterials within biological systems [6, 85].

The hierarchical nature of nano-bio interactions presents a series of formidable biological barriers that significantly impede the targeted delivery of nanoparticles to their intended site of action [12, 89]. At each physiological interface, nanoparticles are susceptible to various elimination mechanisms, including reticuloendothelial system (RES) sequestration, enzymatic degradation, protein corona formation, and immune-mediated clearance, which collectively contribute to a substantial attrition rate throughout the delivery trajectory [90, 91]. A comprehensive understanding of the complex interplay between nanoparticle physicochemical properties (size, shape, surface charge, and hydrophobicity) and biological components (plasma proteins, endothelial cells, extracellular matrix, and cellular membranes) at each hierarchical level is crucial for the rational design of advanced nanocarriers [5, 92]. The optimization of nanoparticle characteristics specifically navigates the intricate biological milieu of the delivery pathway, thereby enhancing targeting efficiency and therapeutic outcomes [7].

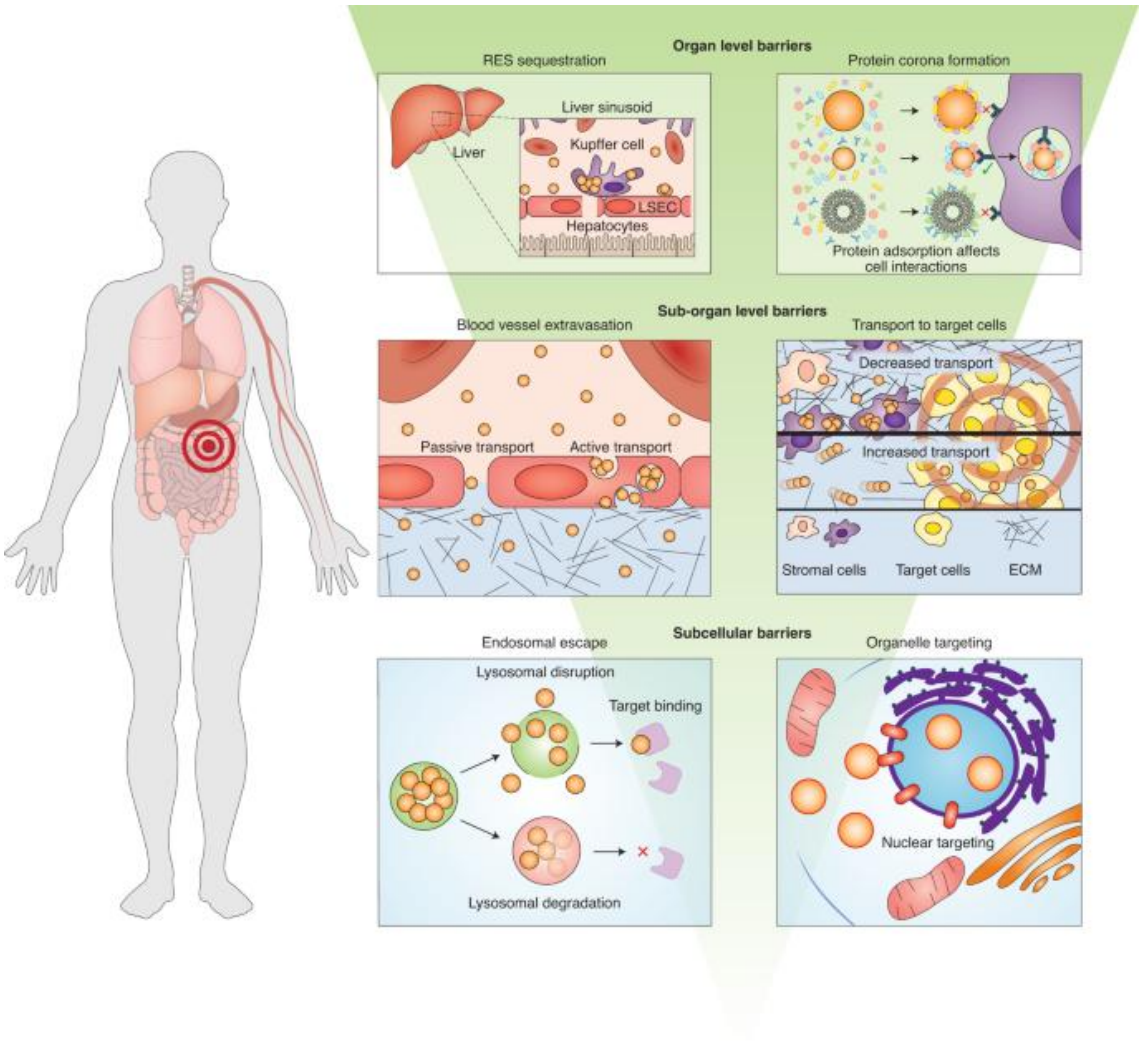

Figure 1.2. Biological levels of nanoparticle barriers [88].

In a seminal work on nanomedicine-based cancer therapeutics, Sun et al. introduced the conceptual framework of the CAPIR cascade, which delineates the sequential biological barriers encountered in tumor-targeted drug delivery systems [93, 94]. The fundamental objective of anticancer nanomedicine delivery is to facilitate the transport and subsequent liberation of therapeutic agents as bioactive molecules within the intracellular compartment of malignant cells to exert their pharmacological activity. From a pharmacokinetic perspective, systemically administered nanomedicines must successfully navigate through five critical physiological stages: (1) systemic circulation within vascular compartments, (2) extravasation and tumor-specific accumulation mediated by the enhanced permeability and retention (EPR) effect through the aberrant, hyperpermeable neovasculature, (3) interstitial transport and deep tissue penetration

within the tumor microenvironment to reach target cells, (4) cellular internalization via endocytic pathways, and (5) intracellular drug release from the nanocarrier system - collectively termed the CAPIR cascade (Figure 1.3). Consequently, the overall delivery efficiency (Q), defined as the percentage ratio of intracellularly liberated drug molecules to the total administered dose, can be expressed as the product of individual efficiencies at each stage ($Q_C \times Q_A \times Q_P \times Q_I \times Q_R$). This multiplicative relationship underscores the critical importance of maintaining optimal efficiency at each sequential step, as any single efficiency approaching zero would constitute a rate-limiting bottleneck, dramatically compromising the entire delivery cascade.

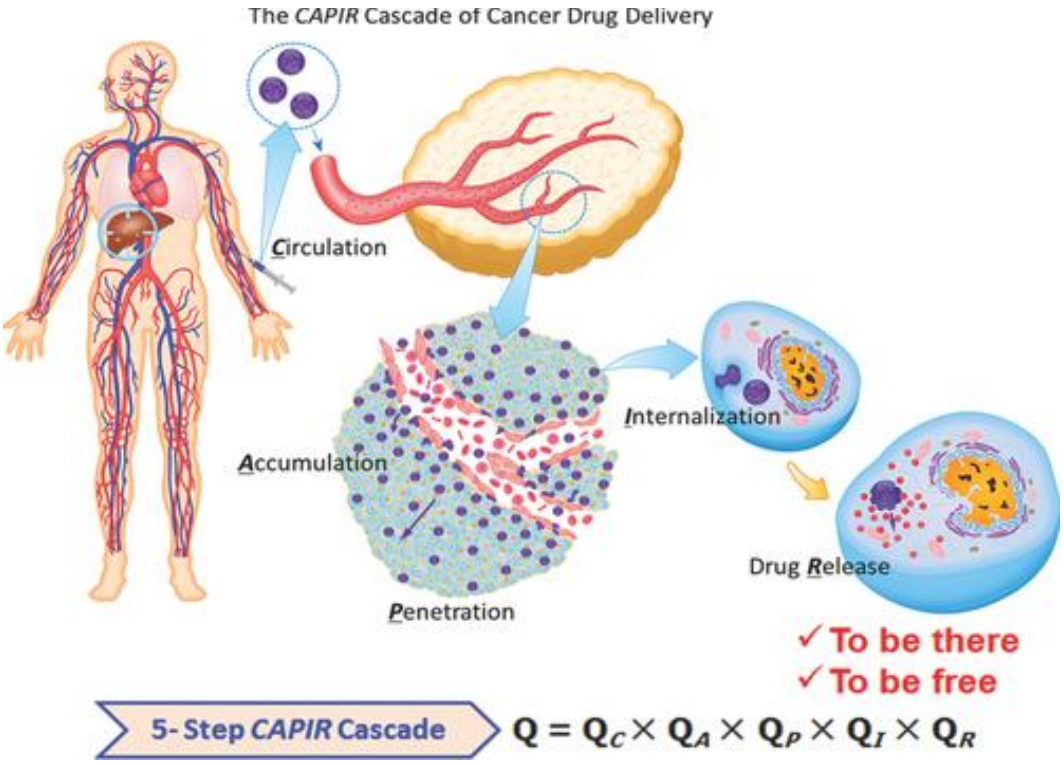

Figure 1.3. A sketch of the CAPIR cascade of nanomedicine to deliver a free drug into cancer cells: circulation in the blood compartments, tumor accumulation and penetration, and subsequent cellular internalization and intracellular drug release. Reproduced with permission. The overall efficiency Q is the product of the five steps' efficiencies [94].

The intracellular liberation of therapeutic payloads from nanocarrier systems represents a critical determinant in optimizing therapeutic efficacy and constitutes an essential component of the drug delivery cascade [8, 95]. Following receptor-mediated endocytosis or other internalization pathways, nanocarriers must demonstrate remarkable stability against lysosomal degradation while preserving the structural integrity and pharmacological activity of their encapsulated cargo within the acidic (pH 4.5-5.5) and enzyme-rich endosomal compartment [96]. Subsequently, successful endosomal escape, mediated through mechanisms such as the proton sponge effect, membrane fusion, or photochemical disruption, is prerequisite for the nanocarriers to access their designated subcellular targets, whether in the cytosol, nucleus, or specific organelles, thereby enabling precise spatiotemporal control of drug release at the intended site of pharmacological action [97].

1.3 Nanoplastics

The widespread use of plastics has led to the pervasive presence of micro- and nanoplastics (MNPs) in the environment, making human exposure inevitable (Figure 1.4) [98]. These particles enter the human body through multiple pathways, including inhalation (e.g., airborne MNPs in urban and indoor environments, with concentrations up to four orders of magnitude higher than in aquatic systems) [99, 100], ingestion (e.g., contaminated seafood, bottled water, and even fruits and vegetables) [101, 102], dermal absorption (e.g., personal care products containing <100 nm nanoplastics that penetrate the skin) [103, 104], and medical exposure (e.g., drug delivery systems and plastic-based medical devices) [105]. Notably, studies have detected MNPs in human tissues, including lungs, blood, and even the placenta, confirming systemic distribution [106].

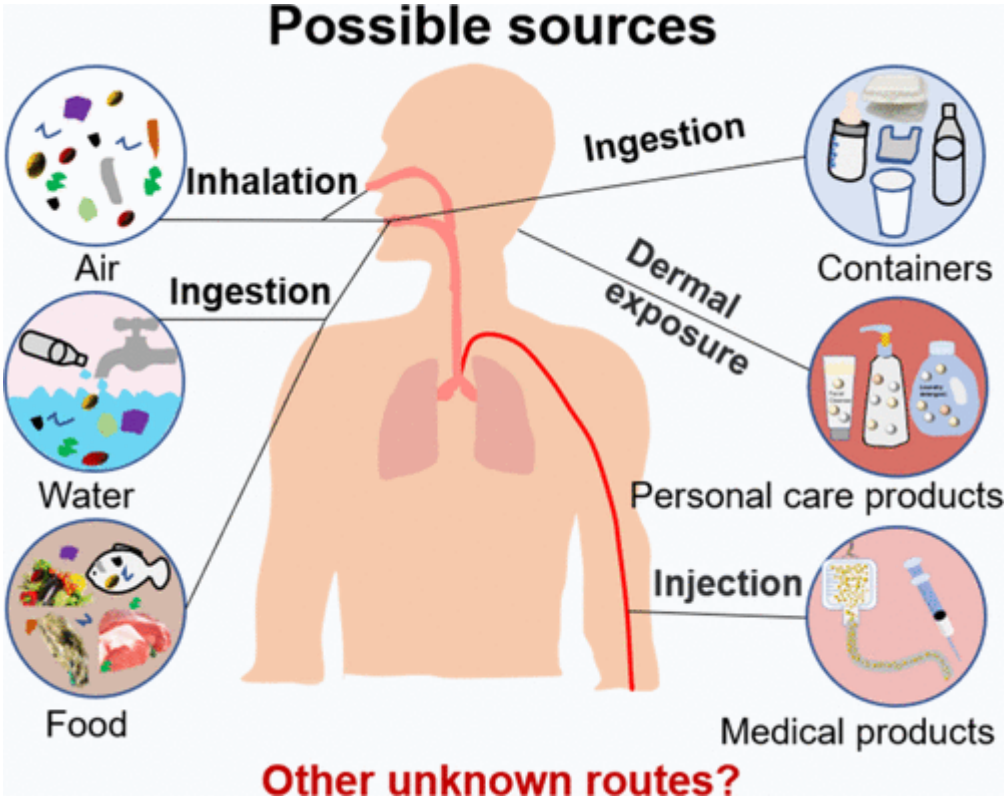

Figure 1.4. Potential sources of microplastics in the human body [98].

Once inside the body, nanoplastics pose significant health risks due to their ability to cross biological barriers (e.g., blood-brain and placental barriers) and induce oxidative stress, inflammation, and cellular damage [107-109]. For instance, inhaled 100 nm polystyrene nanoplastics were found to accumulate in the liver, kidneys, and heart of rats within just 2 h of exposure [110, 111]. Chronic exposure may lead to metabolic disorders, cardiovascular diseases, and even carcinogenesis, exacerbated by adsorbed pollutants (e.g., heavy metals and persistent organic pollutants) and leaching plastic additives (e.g., bisphenol A and phthalates) [112-114].

Current strategies to mitigate nanoplastics in humans remain limited [115]. While enzymatic degradation (e.g., PETase for polyethylene terephthalate) shows promise in environmental contexts, its application in human physiology is constrained by challenges such as low endocytosis efficiency, lysosomal pH incompatibility, and enzyme stability [116, 117]. For example, free enzymes are poorly internalized by cells, and their activity often diminishes in the acidic environment of lysosomes [118]. Additionally, the spatial segregation of enzymes and nanoplastics within cells further reduces degradation efficiency [119].

Given these limitations, there is an urgent need to develop bioinspired intracellular degradation systems, mimicking organisms like waxworms and bacteria that naturally digest plastics. For instance, the superworm Zophobas morio can degrade polystyrene via gut microbiota-derived enzymes [120, 121]. Translating this mechanism into human cells—such as by engineering lysosomal enzymes or utilizing nanoparticle-encapsulated biodegradation agents—could offer a breakthrough in mitigating nanoplastic toxicity. Future research should focus on optimizing enzyme delivery, stability, and compatibility with human cellular environments to achieve effective in situ degradation [122, 123].

1.4 Polyelectrolyte microcapsules

Initially conceptualized in 1998 as a novel physicochemical phenomenon, polyelectrolyte microcapsules have undergone significant technological evolution, emerging as sophisticated delivery platforms for diverse molecular payloads, including therapeutic agents and diagnostic probes [124, 125]. These microcapsules, fabricated through the layer-by-layer (LbL) assembly technique, involve the sequential deposition of oppositely charged polyelectrolytes onto a sacrificial template core, followed by core decomposition, resulting in hollow structures with precisely engineered shells for targeted drug delivery and diagnostic applications (Figure 1.5) [126-128]. The LbL assembly process, fundamentally driven by electrostatic interactions between alternately adsorbed charged species, offers unparalleled advantages in terms of fabrication simplicity and multifunctional versatility [129, 130]. This technique enables precise surface engineering through the incorporation of various functional groups, lipid bilayers, and nanoparticles, allowing for tailored physicochemical and biological properties [131, 132].

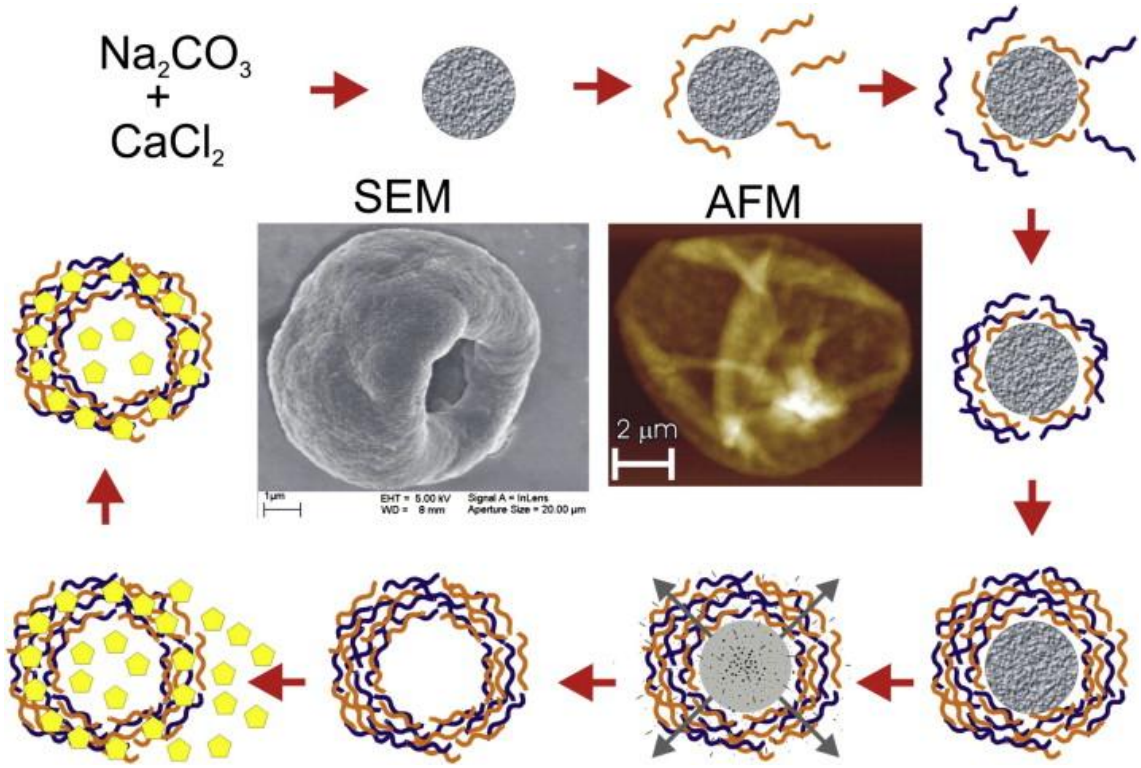

Figure 1.5. Polyelectrolyte multilayers microcapsules are obtained as described in [128]. Consecutive adsorption of layer-by-layer assembled polyelectrolyte multilayers (red and blue) onto calcium carbonate microspheres (gray) is followed by dissolution of core templates by EDTA, and successive incubation with anticancer drug (IM, in yellow) in water solution for drug loading in the polymeric shells. SEM (left) and AFM (right) images of typically folded and air-dried hollow capsules are shown herein [128].

The morphological and functional characteristics of polyelectrolyte multilayer (PEM) capsules are predominantly determined by the template core architecture, making core selection a critical parameter in capsule development [133, 134]. The choice of template significantly influences key parameters such as core dissolution kinetics, shell stability, and colloidal behavior, which collectively determine the capsules' performance in specific applications [135, 136]. Template materials can be broadly categorized into nonporous and porous architectures, each with distinct advantages and limitations. Nonporous templates include organic variants such as melamine formaldehyde (MF) and polystyrene (PS), as well as inorganic materials like nonporous silica [124, 137]. Porous templates, particularly inorganic materials such as mesoporous silica (MS) and calcium carbonate ($CaCO_3$), offer unique advantages due to their high surface area and nanoporous structures. Calcium carbonate templates have garnered significant attention

due to their cost-effectiveness, biocompatibility, and biodegradability, coupled with relatively straightforward synthesis protocols (Figure 1.6) [138]. However, challenges in precise size control and aggregation behavior of $CaCO_3$ particles may limit their application in certain scenarios requiring narrow size distributions and colloidal stability [139]. The dissolution kinetics of these templates under mild conditions, without compromising the integrity of encapsulated biomaterials in biomedical applications [140]. In addition to above mentioned templates, one also has other classes: Anisotropic templates; Biological templates: cells, viruses, and lipid-based; Gel, microgel and nanogel templates; Emulsions like oil-in-water and hydrophobic templates; Air-bubble based capsules for different application [141-143].

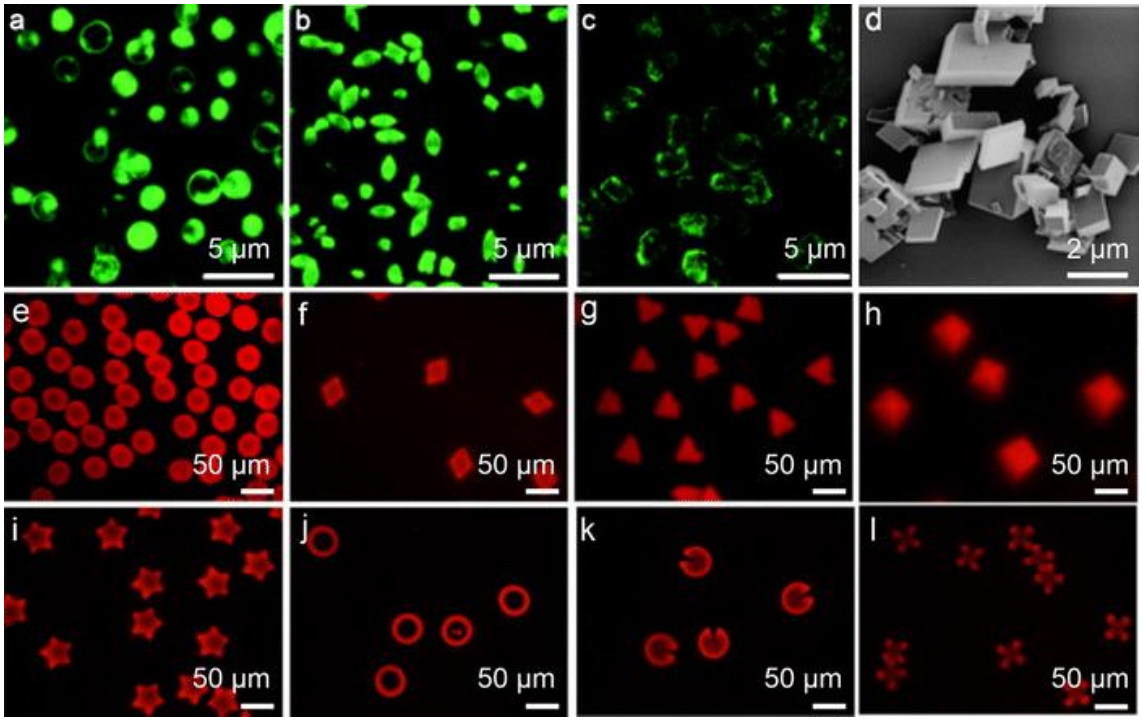

Figure 1.6. Confocal laser scanning fluorescence images of spherical (a), ellipsoid-like (b) and square (c) $CaCO_3$ microparticles. The microparticles were embedded with fluorescein isothiocyanate (FITC)–dextran molecules by co-precipitation and subsequently covered by several oppositely charged polyelectrolyte layers through the LbL assembly; (d) SEM images of $CaCO_3$ rhombohedral microcrystals (calcite); (e–l) fabrication of microparticles of different geometries using the hydrogel template approach [144-146].

The fabrication of polyelectrolyte microcapsules has evolved significantly through the utilization of diverse polyelectrolyte systems, as illustrated in Figure 1.7, with distinct developmental phases reflecting advancements in materials science and biomedical applications [125, 129]. In the initial phase, synthetic polyelectrolytes such as polyallylamine hydrochloride (PAH), polystyrene sulfonate (PSS), polydimethyldiallylammonium chloride (PDADMAC), and subsequently polyacrylic acid (PAA), polyvinyl siloxane (PVS), polyvinylpyrrolidone (PVP), poly(N-isopropylacrylamide) (PNIPAAm), polyethylene glycol (PEG), poly(vinyl caprolactam) (PVCL), and poly(N,N-dimethylacrylamide) (PDMAAm) were predominantly employed [147]. These materials, initially developed for LbL assembly on planar surfaces, provided fundamental insights into capsule formation mechanisms and enabled precise control over capsule properties, including surface charge, permeability, and mechanical stability [148].

The subsequent phase witnessed a paradigm shift towards biologically relevant applications, driving the adoption of biocompatible and biodegradable polyelectrolytes. This included natural and synthetic biopolymers such as poly-arginine (PARG), poly-L-lysine (PLL), polylactic acid (PLA), hyaluronic acid (HA), chitosan (CHT), and dextran sulfate (DS) [149, 150]. Recent advancements have incorporated multifunctional biomolecules such as tannic acid and bovine serum albumin, enhancing the clinical translatability of these systems [151, 152].

In parallel, the integration of nanoparticles into capsule walls has emerged as a transformative approach, enabling the creation of hybrid nanostructures with enhanced functionality. Nanoparticles, including metallic (e.g., gold, silver) [153], magnetic (e.g., iron oxide) [154], and quantum dots [155], can be incorporated into the polyelectrolyte layers or adsorbed onto the capsule surface. These nanoparticle-functionalized capsules exhibit unique properties such as stimuli-responsiveness (e.g., pH, temperature, magnetic field), enhanced mechanical strength, and optical or magnetic properties for imaging and targeted delivery. The strategic incorporation of nanoparticles into the capsule architecture has expanded the potential applications of these systems in theranostics, where diagnostic and therapeutic functions are combined within a single platform [156, 157]. Dingcheng et al. demonstrate the use of photothermal heating mediated by plasmonic nanoparticle-mediated polymer capsules to precisely trigger localized cytosolic calcium release, enabling controlled investigation of intra- and intercellular

calcium wave propagation in biological systems [158]. The approach offers spatiotemporal precision in modulating calcium signaling, with potential applications in neurological research and targeted therapeutic delivery. Sathi et al. provide the first single-particle-level evidence of PEI's proton buffering capacity in lysosomes by co-encapsulating polyethyleneimine (PEI) with pH-sensitive fluorescent probes in polyelectrolyte microcapsules, conclusively demonstrating its "proton sponge effect" mechanism through inhibition of lysosomal acidification to enhance nucleic acid delivery [159].

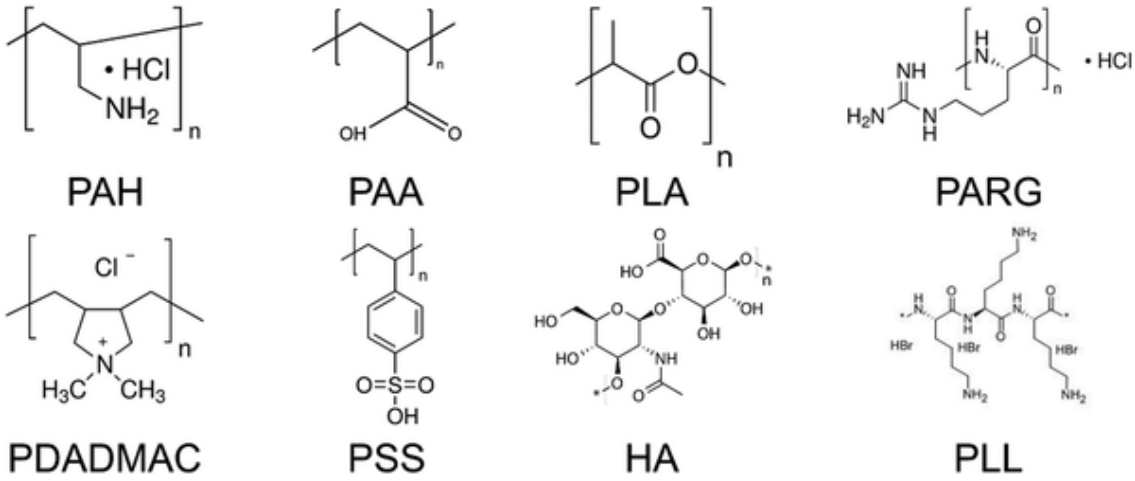

Figure 1.7. Structure of some polyelectrolytes showing polyallylamine hydrochloride (PAH), polyacrylic acid (PAA), polylactic acid (PLA), poly-arginine (PARG), polydimethyldiallylammonium chloride (PDADMAC), polystyrene sulfonate (PSS), hyaluronic acid (HA) and poly-L-lysine (PLL) [144].

1.5 Two-photon microscopes for single-cell imaging

The growing demand for high-fidelity visualization of nanoparticle dynamics in biological systems has driven the adoption of two-photon excitation microscopy (TPEM) as a premier imaging modality [160, 161]. Its unique optical characteristics enable deep-tissue, low-phototoxicity, and high-resolution imaging, making it indispensable for studying cellular uptake, intracellular trafficking, and nanomaterial interactions [162]. TPEM addresses these requirements through several key advantages: 1) Enhanced tissue penetration depth: Utilizing near-infrared (NIR) excitation wavelengths (typically 700–

1100 nm), TPEM significantly reduces light scattering in biological tissues compared to single-photon microscopy. This allows for imaging depths exceeding several hundred micrometers, making it particularly suitable for in vivo and ex vivo studies of thick specimens, such as brain tissue or tumor microenvironments. In brain tissue, TPEM achieves ~500–1000 μm imaging depth, whereas single-photon confocal microscopy is typically limited to ~100–200 μm [163].

For tumor spheroids, TPEM permits 3D reconstruction up to ~300–500 μm, compared to ~50–150 μm with single-photon methods [164]. 2) Reduced phototoxicity and photodamage: The lower energy per NIR photon (~1.2–1.8 eV) minimizes single-photon absorption by endogenous fluorophores (e.g., NADH, flavins), thereby decreasing photoinduced cellular stress [165, 166]. Empirical studies demonstrate that TPEM improves cell viability by 3–5-fold compared to conventional confocal microscopy under equivalent imaging conditions [167]. 3) Spatially confined photobleaching: The nonlinear nature of two-photon absorption (proportional to the square of excitation intensity) restricts fluorescence excitation to a highly localized focal volume (~0.1–1 fL) [168]. This intrinsic optical sectioning not only reduces out-of-focus photobleaching but also enhances axial resolution (1–2 μm), enabling prolonged time-lapse imaging with ~60–80% less signal degradation than widefield techniques [169].

A standard TPE microscopy system shares fundamental components with a conventional laser-scanning confocal microscope, with the critical distinction being the absence of a confocal pinhole (Figure 1.8) [161]. The system employs a high-intensity, pulsed near-infrared (NIR) laser source, typically a mode-locked Ti:sapphire laser emitting femtosecond (fs) pulses, which is raster-scanned across the specimen using a pair of galvanometer-driven mirrors (galvos). This scanning mechanism sequentially illuminates discrete spatial points within the focal plane, with emitted fluorescence signals being detected pixel-by-pixel to reconstruct a high-resolution optical section. Detection is achieved using high-sensitivity photodetectors such as photomultiplier tubes (PMTs), avalanche photodiodes (APDs), or hybrid detectors (e.g., GaAsP), which are optimally positioned in a non-descanned configuration immediately behind the objective lens. Unlike one-photon confocal systems, where fluorescence must be rescanned through the galvanometer mirrors and filtered through a pinhole, TPE microscopy employs non-descanned detection (NDD). This configuration minimizes photon losses by: 1) Eliminating the pinhole, thereby maximizing signal collection efficiency. 2) Reducing the

number of optical interfaces (e.g., scan lenses, tube lenses, and additional mirrors) that could attenuate the emitted fluorescence. 3) Capturing scattered emission photons that would otherwise be rejected in a confocal system. Furthermore, in a microscope setup, fluorescence can be collected epi-detected (i.e., through the same objective used for excitation), allowing efficient capture of both ballistic and scattered photons propagating along the optical axis. This approach enhances signal collection by utilizing photons that would be lost in traditional descanned confocal detection scheme [170, 171].

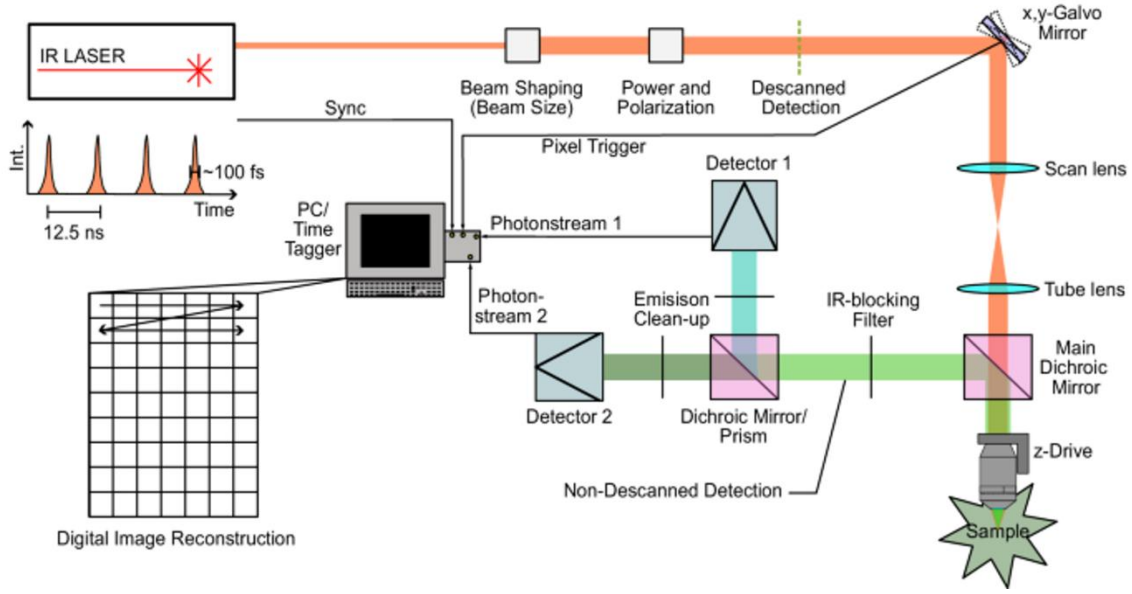

Figure 1.8. Scheme of a typical TPE laser scanning microscope. Depicted are beam path, TPE laser properties, non-descanned detection, and digital image reconstruction. For comparison with conventional confocal LSM, the position of the descanned detection (before the galvo mirror) is indicated by a green dashed line (meaning in descanned detection the main dichroic mirror and the detectors would be moved to this position) [161].

2 An intriguing polymeric modification strategy for solid nanoparticles to investigate endosomal escape of cargos from polyelectrolyte microcapsule

2.1 Introduction

In recent years, new methods based on nanomaterials have shown great promise in disease treatment, nanoparticles have therefore been extensively investigated to improve the delivery efficiency of therapeutic [19, 172, 173]. Although the main pathway for cellular entry of nanoparticles is through endocytosis (initially captured within vesicles [174-176]), cytosolic delivery of nanoparticles via these vehicles is still a complicated cascade [177, 178]. Basically, endosomal escape is the major bottleneck in the delivery of therapeutics within cells [179], and becomes a critical success factor for delivery strategies involving intracellular targets [180-182]. The mechanism of endosomal escape and enhancement of endosomal escape approaches for nanoparticles have been extensively studied, such as fusion with the endosomal membrane [183], or endosomal membrane rupture [184], dissociation/instability in the endosome's acidic cavity [185]. However, since the therapeutic activity of these nanoparticles often occurs in other subcellular compartments outside the cytoplasm or the lysosome (i.e., cytoskeleton, nuclei, mitochondria, etc [186]), the delivery systems remain limited by inefficient trafficking of the particles to the active regions [177, 187]. Unfortunately, the impact of intracellular diffusion process on delivery efficiency for nanoparticles is not sufficiently appreciated.[5] So far, robust design guidelines for nanoparticles to improve intracellular diffusion and a methodology for spatially and temporally controlling and monitoring the release kinetics are lacking. Hence, it is important to note that the intracellular diffusion process of nanoparticles escaping and reaching the target position must be taken into consideration when focusing on endosomal escape studies. A new strategy to investigate and improve the intracellular diffusion of nanoparticles is highly sought.

To improve the outcomes of intracellular diffusion of nanoparticles and improve the delivery efficiency of therapeutic, combining fundamental nanoparticle studies with the design of better techniques to sense endosomal escape events is indispensable [188-190]. One approach is based on polymer capsules assembled from polyelectrolytes in a

layer-by-layer (LbL) fashion [124, 147, 191]. It was presented recently, that by incorporating plasmonic nanoparticles into the capsule walls, a light-triggered release with micrometer spatial resolution can be achieved [177]. Successful intracellular release was demonstrated with > 40 different molecules, ranging from small fluorophores to proteins. With confocal laser scanning microscopy (CLSM), the diffusion of the cargos in the cells could then be tracked with ~100 ms temporal resolution. The design of the capsules and the experiments were optimized to ensure cell viability, maximum loading and a robust controlled release. The feasibility of the approach was demonstrated in 2D mono- and co-cultures as well as in 3D cell spheroids [158]. Taken together, the approach is very promising for spatiotemporally controlled release of molecular cargos into the cytosol. This ability would also be useful to study the structure, dynamics and effects of nanomaterials inside living cells. However, the approach described above failed for all particles tested (gold nanocluster (Au NC) with a core diameter d_{core} ~ 1.5 nm, quantum dot (QD), d_{core} ~ 7 nm, and Fluorospheres, d_{core} ~ 20 nm). Considering that the high diffusion coefficient and the complexity of surface ligands of those nanoparticles cause the interaction attractive interactions with components of the capsules or lysosome, the rapid diffusion of nanoparticles to the final target location within the cell is a grand challenge. The capability to improve nanoparticles' stealth properties is a key issue.

PEGylation provides stability and stealth effects to nanoparticles through steric inhibition and the formation of an aqueous layer around the nanoparticle due to its hydrophilic nature [192]. In addition, PEG backfilling can prevent nanoparticle targeting moieties from sterically blocking the binding of the biorecognition molecule to the receptor target [193]. The initial goal of our study therefore was to study that the feasibility of PEGylated nanoparticles that can be released within the cell upon photothermal heating and develop a quantitative analysis, investigate the tailored surface-chemistry that can enable control cytosolic delivery of nanomaterials to reverse the resistance caused by low diffusion coefficients of nanomaterials.

In this work, we tested the triggered release of PEGylated nanoparticles with core diameters ranging from d_{core} ~ 1.5 nm – 100 nm. A robust and controlled release was achieved with all tested nanomaterials with a PEG coating and the intracellular diffusion was quantified. Interestingly, we observed a clear dependence of the diffusion on the co-loading of additional molecular cargo. The intracellular diffusion of PEGylated nanoparticles was faster when the PEG-polymers were terminated methoxy-groups (-

OCH_3) compared to carboxylic acid termini (-COOH). Calcein co-encapsulation significantly enhanced the intracellular release of the PEGylated nanoparticles. The work provides a valuable quantitative tool for intracellular studies addressing the fate of nanomaterials on diffusion and a reliable basis for developing design guidelines to improve the crucial diffusion issues in cytosolic delivery of nanoparticles.

2.2 Experimental section

2.2.1 Regents and materials

Hydrochloric acid (HCl, #4625.1), sodium hydroxide (NaOH, #6771.1), trisodium citrate dihydrate (#3580.4) and Sodium chloride (NaCl, #HN00.2) were purchased from Carl Roth (Germany). 6-Aza-2-thiothymine (ATT, #A14167.06) was purchased from ThermoFisher (Germany). Isoprene (#I19551), 2,2′-Azobis(2-methyl-propionitrile) (AIBN, #441090), nitric acid (HNO_3, #30709), calcein (#C0875), gold(III) chloride trihydrate ($HAuCl_4 \cdot 3H_2O$, #520918), thioctic acid (TA, #63320), sodium borohydride ($NaBH_4$, #71320), N-hydroxysuccinimide (NHS, #130672), N-(3-Dimethylaminopropyl)-N′-ethylcarbodiimide hydrochloride (EDC, #03450), silver nitrate ($AgNO_3$, #204390), ascorbic acid (AA, #33034), Poly(sodium 4-styrenesulfonate) (PSS, Mw = 70 kDa, #243051), poly(allylamine hydrochloride) (PAH, Mw = 56 kDa, #283223), calcium chloride dihydrate ($CaCl_2 \cdot 2H_2O$, #223506), sodium carbonate (Na_2CO_3, #S7795) and ethylenediamine-tetra-acetic acid disodium salt dihydrate (EDTA disodium salt, #E5134) were purchased from Sigma-Aldrich (Germany). Tetrahydrofuran (THF, #32468.K2), *n*-hexane (#326920010) and ethanol (#07025.1700) were purchased from VWR. NH_2-$PEG_{2k}OCH_3$ (Mw = 2 kDa, #122000-2), HSC_2H_4CONH-$PEG_{3k}OC_3H_6COOH$ (Mw = 3 kDa, #133000-4-32) and HSC_2H_4CONH-$PEG_{2k}OC_3H_6OCH_3$ (Mw = 2 kDa, #122000-40) were purchased from Rapp Polymere. Ultrapure double distilled water (ddH_2O, MilliQ) with a resistivity greater than 18.2 MΩ cm^{-1} was used for all experiments.

.

2.2.2 Synthesis of non-PEGylated and PEGylated solid nanoparticles

ATT-Au NCs

According to the published protocol [194], ATT-Au NCs were prepared for the introduction of 15 mL of $HAuCl_4$ (10 mg/mL) aqueous solution into 15 mL of ATT solution containing 0.2 M NaOH. The solution was kept vigorous stirring at 1,000 rpm in the dark at room temperature for more than 6 h. To remove excess ATT, the as-synthesized ATT-Au NCs were purified by ultrafiltration (Millipore, 3 kDa). Finally, the

result ATT-Au NCs were re-dispersed in water and stored at 4 °C in the dark until further use.

TA-Au NCs

According to the published protocol [195], TA-Au NCs were prepared for the introduction of 10.2 μL of $HAuCl_4 \cdot 3H_2O$ (470 mg/mL) aqueous solution into the mixture solution of 7.8 mg of thioctic acid (TA), 60 μL of NaOH (2 M) and 23.4 mL of ultrapure water. The solution was kept vigorous stirring at 1,500 rpm in the dark at room temperature for 15 min, followed by the addition of 480 μL of freshly prepared $NaBH_4$ (1.9 mg/mL) under vigorous stirring at 1,500 rpm overnight. To remove excess TA, the as-synthesized TA-Au NCs were purified by ultrafiltration (Millipore, 3 kDa). Finally, the result TA-Au NCs were re-dispersed in water and stored at 4 °C in the dark until further use.

PEG-Au NCs

The synthesis of PEG-Au NCs is predicated on TA-Au NCs as the precursor in 1.2.1.2). The TA-Au NCs solution was added 15.6 mg of HSC_2H_4CONH-$PEG_{2k}OC_3H_6OCH_3$ and adjusted the pH to 7-7.5 under gently stirring at 500 rpm overnight. To remove excess PEG, the as-synthesized PEG-Au NCs were purified by ultrafiltration (Millipore, 3 kDa). Finally, the result PEG-Au NCs were re-dispersed in water and stored at 4 °C in the dark until further use.

QDs

QdotTM 565 (#Q21331MP) and QdotTM 655 (#Q21321MP) ITKTM carboxyl quantum dots were purchased from ThermoFisher (Germany).

PEG-QDs

QDs [196] and amphiphilic diblock copolymers polyisoprene-*block*-poly(ethylene oxide) (PI-*b*-PEG) [197] were synthesised according to the protocols used earlier. QDs were incubated with a 2000-fold excess of polymer ligand PI-DETA in n-hexane for more than 20 h. Then, the QDs were precipitated with ethanol and centrifuged, followed by solving in THF and mixed with a 500-fold excess of PI-b-PEG and AIBN (1/3 of isoprene units present in the diblock copolymer) in THF. The QDs-polymer-

AIBN-THF solution was slowly injected into the 12-fold excess of water and heated up to 80 °C. After 4 h, the QDs solution was washed with water by purified by ultrafiltration (Millipore, 100 kDa). Subsequently, the QDs were performed by a sucrose gradient centrifugation to remove empty micelles and to separate different QDs micelle fractions. Finally, the QDs were washed with water three times by ultrafiltration (Millipore, 100 kDa) to remove the sucrose and re-dispersed in water, and stored at 4 °C in the dark until further use [198].

Polystyrene (PS) Beads

FluoSpheresTM carboxylate-modified microspheres 0.02 μm red fluorescent (FluoSphere, #F8786) were purchased from ThermoFisher (Germany).

PEG-PS beads

The synthesis of PEG-PS beads is predicated on PS beads as the precursor in 1.2.3.1). PEG-PS beads were prepared by adding 0.5 mL of PS-COOH (1 mg/mL) aqueous solution into 4.5 mL of water, followed by the addition of 226 μL of EDC aqueous solution (75 mM) under gently stirring at 500 rpm at room temperature for 5 min. Subsequently, 13 μL of NHS aqueous solution (15 mM) was added and stirred at 500 rpm for 30 min. The mixture solution was added 1 mL of HSC_2H_4CONH-$PEG_{2k}OC_3H_6OCH_3$ aqueous solution (10 mg/mL) under gently stirring at 500 rpm at room temperature overnight. To remove excess PEG, the as-synthesized PEG-PS beads were purified by ultrafiltration (Millipore, 50 kDa). Finally, the result PEG-PS beads were resuspended in water and stored at 4 °C in the dark until further use. EDC/NHS/PEG/PS=20:25:25:1.

2.2.3 Synthesis of Au NPs

Gold nanostars (GNSs) were synthesized according to the protocol used earlier by a seed-mediated growth method [199]. All glassware was washed with Aqua Regia, HCl: HNO_3 = 3:1 (v:v), and rinsed with ethanol and Milli-Q water. Firstly, the gold nanoparticles (GNPs) as seed were synthesized as following: trisodium citrate dihydrate (0.15 g, 0.51 mmol) was added to 110 ml of boiling water under reflux under vigorous

stirring at 1,500 rpm. After 15 min of boiling, the solution was added 4 mL of freshly prepared 25 mM $HAuCl_4$ (25 mM, 9.845 mg/mL) and kept stirring for 15 min. This colorless solution turned into red within ca. 1 min, indicating the formation of larger gold nanospheres. Afterward, the solution was cooled to room temperature and filtered by a 0.22 μm nitrocellulose membrane. The seed solution was stored at 4 °C until further use. The as-prepared sample was directly used as seeds for the preparation of gold nanostars. Secondly, gold nanostars were synthesized as following: 1 mL of the seed solution was mixed with 180 μL of 1 M HCl, 2 mL of $HAuCl_4 \cdot 3H_2O$ solution and 110 mL of water thoroughly under vigorous stirring at 1,500 rpm. Then 1 mL of freshly prepared $AgNO_3$ solution (2 mM, 0.340 mg/mL) and 1 mL of ascorbic acid solution (100 mM, 17.612 mg/mL) were simultaneously added to the above mixture under vigorous stirring at 1,500 rpm for 30 s, and immediately cooled in an ice bath to stop growth. To initiate ligand exchange, 2.0 mL of $HSC_2H_4CONH\text{-}PEG_{3k}OC_3H_6COOH$ (3.3 mM, 10 mg/mL) and 250 μL of NaOH solution (2 M, 80 mg/mL) were added to the above solution. The solution was kept gently stirring in the dark at room temperature for more than 6 h. To remove residual PEG, the as-synthesized GNSs were purified by centrifugation at 6000 rpm at room temperature for 10 min. Subsequently, the supernatant was removed, and the GNSs were resuspended in 15 mL of water. This process was repeated three times, with the supernatant discarded and fresh water added each time. Finally, the GNSs were resuspended in 15 mL of water and stored at 4 °C until further use.

2.2.4 Synthesis of photo-triggered released polyelectrolyte capsules

Photo-triggered released polyelectrolyte capsules were synthesized according to the protocol used earlier. In a typical synthesis [177], the first micrometer-sized $CaCO_3$ template cores were fabricated. 615 μL of 0.33 M Na_2CO_3 solution was mixed with 400 μL of 5 mg/mL molecular cargo in a 20 mL glass vial. The above solution was mixed thoroughly by vigorous stirring at 900 rpm. Followed by 615 μL of 0.33 M $CaCl_2 \cdot 2H_2O$ solution, the vial was kept at room temperature under stirring for 30 s, and then left standing for 3 min to stop $CaCO_3$ growth. The $CaCO_3$ cores were collected by centrifugation at 3000 rpm for 30 s and then washed with water three times by centrifugation at 3000 rpm for 30 s at room temperature, discarding the supernatant, and

adding fresh water. Then, polyelectrolyte capsules were synthesized by layer-by-layer assembly of oppositely charged polymers based on the template cores. The $CaCO_3$ cores were resuspended in 1 mL of negatively charged PSS (10 mg/mL, 0.1 M NaCl, pH 6.5), sonicated for 2 min, kept under continuous shaking for 10 min, and washed with water three times by centrifugation at 3000 rpm for 30 s at room temperature, discarding the supernatant, and adding fresh water. After washing, 1 mL of positively charged PAH (10 mg/mL, 0.1 M NaCl, pH 6.5) was added to the particles, and a similar procedure was followed as described for PSS shell generation. With the same steps, additional layers of PSS and PAH layers were formed, resulting in 2 (PSS/PAH) bilayers. To provide light-responsiveness to capsules, the negatively charged GNSs were deposited between the polyelectrolyte layers. 1.5 mL of GNSs were added to the template cores with 2 (PSS/PAH) bilayers, and a similar procedure was followed as described for PSS shell generation, resulting in $(PSS/PAH)_2$/GNSs layers. The last bilayers were made by PAH and PSS, leading to a final layer geometry of $(PSS/PAH)_2$/GNSs/PAH/PSS ($caps^-$). Subsequently, the polymer-coated $CaCO_3$ template plastics were incubated in 2 mL of EDTA (0.1 M, pH 6.5) overnight at 4 ℃ to dissolve the $CaCO_3$ core. The hollow capsules were collected by centrifugation at 1800 rpm for 10 min and then washed with water three times to remove the excess EDTA, by centrifugation at 3000 rpm for 30 s at room temperature, discarding the supernatant, and adding fresh water. Finally, the capsules were resuspended in 1 mL of water and stored at 4 °C until further use. In addition, the capsules with PAH/PSS/PAH/GNSs/PAH/PSS shell geometry ($caps^+$) were formulated using the same approach.

For calcein, molecular cargos with molecular weight Mw less than 10 kDa were encapsulated by postloading and heat-shrinking [177]. In one set of experiments, hollow capsules without cargoes were synthesized, while all other parameters were kept the same. The hollow capsules were introduced to 500 µL of calcein (10 mg/mL, pH 5.5-6) at room temperature for 90 min and then heat-shrunken at 75 ℃ for 2 h. The capsules were collected by centrifugation at 1800 rpm for 10 min and then washed with water three times, by centrifugation at 3000 rpm for 30 s at room temperature, discarding the supernatant, and adding fresh water. Finally, the capsules were resuspended in 1 mL of water and stored at 4 °C until further use.

The category, size, and excitation/emission wavelength of cargos are listed in Table 1.

Table 1. Information about encapsulated molecular cargos

Loading method	Category		Cargo	Size [nm]	Excitation/Emission wavelength $\lambda_{Ex}/\lambda_{Em}$ [nm]
Postloading	Small molecules		Calcein	Mw = 622.6 g/mol	495/517
Preloading	Solid nanoparticles	Au nanoclusters	ATT-Au nanoclusters	1-1.5	400, 480/528
			TA-Au nanoclusters	~1.0	348/680
		PEG-Au nanoclusters	PEG-Au nanoclusters	~2.5	348/680
		QDs	QDs 565	3.0-3.5	405/565
			QDts 655	7	405/654
		PEG-Qdots	QDs 263-PEG-OCH_3	15-20	350/560
			QDs 359-PEG-OCH_3	15-20	359/628
			QDs 359-PEG-COOH	15-20	359/630
		Fluospheres	PS beads	100	350/440
		PEG-Fluospheres	PEG-PS beads	100	350/440

2.2.5 Characterization of nano- and microparticles

The morphology of the solid nanoparticles was determined with a transmission electron microscope (TEM, JEM 1011, JEOL) on dried samples.

The UV/Vis spectra were collected in MilliQ water using a UV/Vis Spectrometer (Cary 60, Agilent). The fluorescence emission spectra were collected in MilliQ water using a Fluorescence Spectrometer (Cary Eclipse, Agilent).

The morphology of gold nanoparticles (GNPs) and gold nanostars (GNSs) was determined with a transmission electron microscope (TEM, JEM 1011, JEOL) on dried samples.

The UV/Vis spectra of GNPs and GNSs were collected in MilliQ water using a UV/Vis Spectrometer (Cary 60, Agilent).

Hydrodynamic diameter d_h and Zeta potential ζ of the particles in MilliQ water were obtained using a Malvern Zetasizer Particle Analyzer (ZEN3600, Malvern).

The morphology of the $CaCO_3$ cores and capsules was determined with a scanning electron microscope (SEM, Gemini 1550, Zeiss) and a fluorescence microscopy (LSM880 system, Zeiss; the continuous wave laser was generated by a two-photon generator (Ti:Sa Laser Mai Tai, Spectra Physics)).

2.2.6 Cell culture techniques

Human cervical cancer cells (HeLa cells) were cultured in Dulbecco's Modified Eagles Medium (DMEM, #11965092, ThermoFisher Scientific) with 4.5 g/L glucose supplemented with 10% fetal bovine serum (FBS, Biochrom, Germany, #S0615), 1% penicillin/streptomycin (P/S, #15070063, Thermo Fisher Scientific) at 5% CO_2 and 37°C.

2.2.7 Monitoring the diffusion kinetics of encapsulated molecular cargo

100,000 Hela cells in 2 mL of culture medium supplemented with 10% FBS were seeded in per µ-Dish (#81156, ibidi; bottom area: 3.5 cm^2). The cells were kept overnight at 5% CO_2 and 37 °C. Afterwards, cells were incubated with capsules at a concentration of $N_{caps/cell}$ = 1.5 capsules per seeded cell overnight. After 24 h incubation of cells with capsules, these cells were washed three times with PBS and 2 mL of culture medium supplemented with 10% FBS was added. Subsequently, the cells were imaged using an upright confocal laser scanning microscope (LSM880 system, Zeiss). The continuous wave laser was generated by a two-photon generator (Ti:Sa Laser Mai Tai, Spectra Physics) for photothermal opening. Images were acquired by the software ZEN 2.3 (blue edition, operation software for LSM880). Refer to Table 1 for a comprehensive overview of the excitation and emission settings for fluorescence molecular cargos.

2.2.8 Molecular dynamics (MD) simulation

Molecular dynamics (MD) simulations were performed based on the Gromacs 2021.2 [200] and Amber force field (amber 14sb_OL15) [201]. Molecular structures and kinetic trajectories were viewed in VMD [202]. Gold clusters models with different ligands were initially packed in a 12 × 12 × 12 nm cubic box by the Packmol [203], in which the gold clusters were placed in the center of the box. Similarly, the Cal adsorption model was also constructed, with gold cluster model in the center and Cal randomly placed inside the box. The atomic charges of different terminal-group modified PEG ligands (PEG-OCH_3, PEG-COOH), TA ligands and calcein were calculated by the charge

equalization method (QEq) in Material Studio 2017R2. The include toplogy (itp) files of all models were obtained by Sobtop (Tian Lu, Sobtop, Version 1.0(dev3.2), http://sobereva.com/soft/Sobtop, accessed on 17 Feb 2024). The water molecule amount and salt concentration of each system were kept constant, with SPCE as water model and Na^+ and Cl^- as counter ions. Periodic boundary conditions were used in all three Cartesian directions. L-BFGS algorithm, Steep algorithm, and CG algorithm were used sequentially with LINCS to minimize the energy of each system. The equilibrium phases simulations were then carried out in the NPT system for 1 ns with a time step of 1 fs, in which the temperature was maintained at 310 K (in vivo temperature) using V-rescale thermostat, and the pressure was set to 1 Bar (atm) using parrinello-rahman barostat. After the completion of the equilibrium phase, a 10 ns production phase simulation was performed in the NPT system, with the same temperature and pressure bath conditions, and with a time step of 2 fs. Also, The Verlet algorithm was used to construct the neighbor lists, where PME method was applied for the electrostatic interactions with a cut-off of 1.0 nm, Cut-off method was considered to calculate Van der Waals interactions with a cut-off of 1.0 nm. Molecular structures and kinetic trajectories were viewed in VMD [202].

For exploring the hydrophilicity of small molecules, the initial conformations of the PEG-OCH_3 and PEG-COOH short chain were derived from the end-chain conformations of the PEG ligands in production phase. A 5 × 5 × 5 nm cubic box was used for the modeling, and the rest of the computational details were consistent with those described above.

2.3 Result and discussion

2.3.1 Characterization of polyelectrolyte microparticles (caps) and molecular cargos

The stimuli-responsive microcapsules were fabricated utilizing calcium carbonate ($CaCO_3$) microparticles as templates and employing layer-by-layer (LbL) assembly of the polyelectrolytes poly(styrenesulfonate) (PSS, negatively charged) and poly(allylamine hydrochloride) (PAH, positively charged). Based on our previous work including the optimization of capsule properties, we synthesized capsules with the polyelectrolyte sequences $(PSS/PAH)_2$/GNSs/PAH/PSS ($caps^-$) or PAH/$(PSS/PAH)_2$/GNSs/PAH/PSS ($caps^+$), where GNS refers to the gold nanoparticles (here: nanostars) which are encapsulated into the capsule walls to facilitate the light-triggered rupture of these walls. This design ensures stable capsules with a high amount of encapsulated molecular cargo and minimal leakage, which can be opened intracellularly by a light pointer with micrometer resolution [204].

The synthesis of gold nanostars (GNSs) was carried out in accordance with the protocol previously established utilizing a seed-mediated growth method. In the reported synthesis, the size of gold nanostars (GNSs) was precisely modulated by systematically varying the concentration of Au seeds dispersed within the growth solution. Specifically, an increase in the seed concentration resulted in a reduction in the number of available Au atoms per seed, thereby leading to the formation of smaller nanostars. This inverse relationship arises because a higher density of seeds distributes the limited Au precursor among a greater number of nucleation sites, limiting the growth potential of each individual seed. By leveraging this relationship, the seed concentration serves as a critical parameter for controlling the size of GNSs. This size tunability directly influences the longitudinal surface plasmon resonance (LSPR) peak of the nanostars, particularly in the near-infrared (NIR) region. Larger nanostars exhibit a red-shifted LSPR peak, while smaller nanostars demonstrate a blue-shifted peak. This ability to fine-tune the plasmonic properties of GNSs is essential for optimizing their performance in applications such as photothermal therapy, biosensing, and in vivo imaging, where precise control over optical characteristics is required. The geometry and the shape of gold nanoparticles (GNPs, seeds) and GNSs are shown in Figure 2.1. The mean hydrodynamic diameters of GNPs and GNSs were determined to be d_h = 11.44 ± 0.49 nm and d_h = 122.50 ± 2.50 nm,

respectively, see Figure 2.2. In Figure 2.3, the seed GNPs had an absorption peak at λ = 520 nm. The surface plasmon resonance (SPR) peak of GNSs was at λ = 828 nm. GNSs have been shown to efficiently convert absorbed near-infrared (NIR) radiation into heat. This property, coupled with the fact that blood, skin, and tissues in the NIR are semitransparent, has led to the conceptualization of in vivo applications of gold nanostructures for photothermal therapy. The mean zeta-potential of GNS was found to be ξ = -22.87 ± 0.74 mV, which provides the basis for the formation of the capsule wall by electrostatic adsorption, see Figure 2.4.

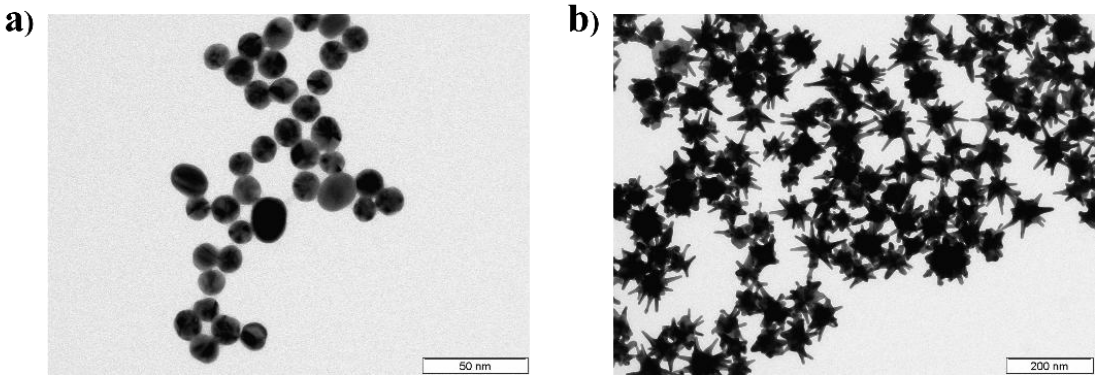

Figure 2.1. TEM images of GNPs and GNSs. The scale bar corresponds to 50 nm and 100 nm, respectively.

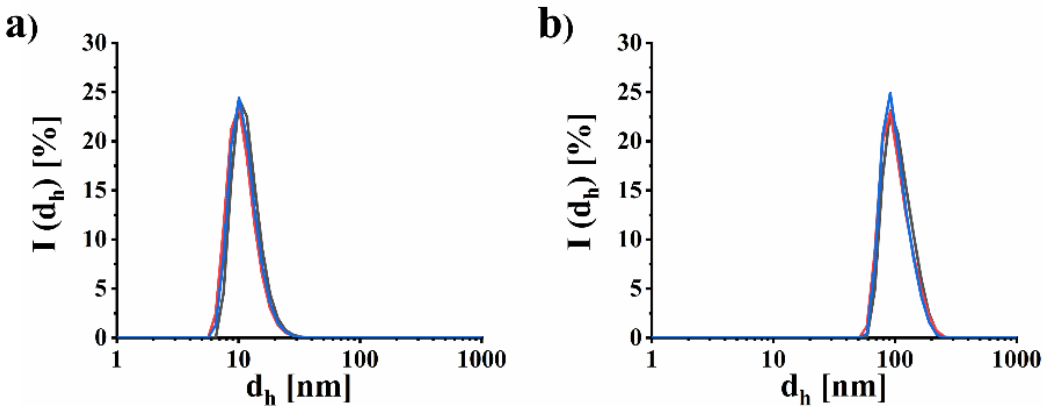

Figure 2.2. Intensity-weighted distribution of the hydrodynamic diameters for a) GNPs and b) GNSs. The data are based on three repeats of measuring the same samples.

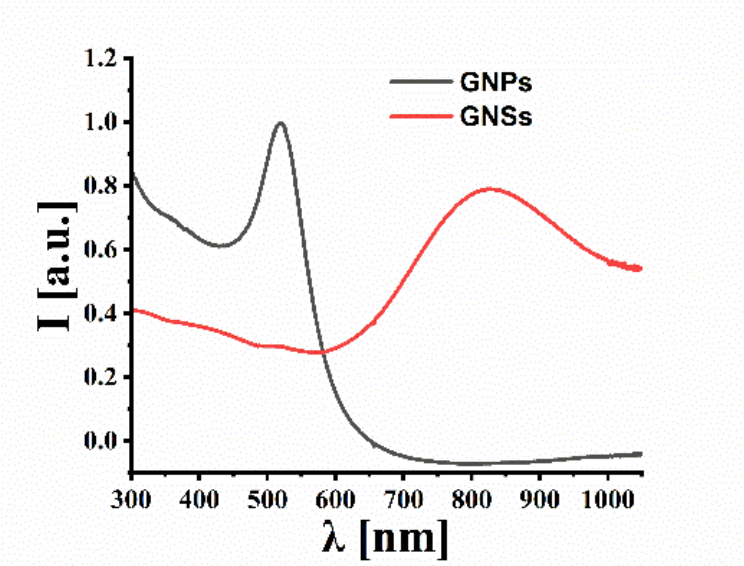

Figure 2.3. UV-Vis spectra of aqueous solutions of GNPs and GNSs.

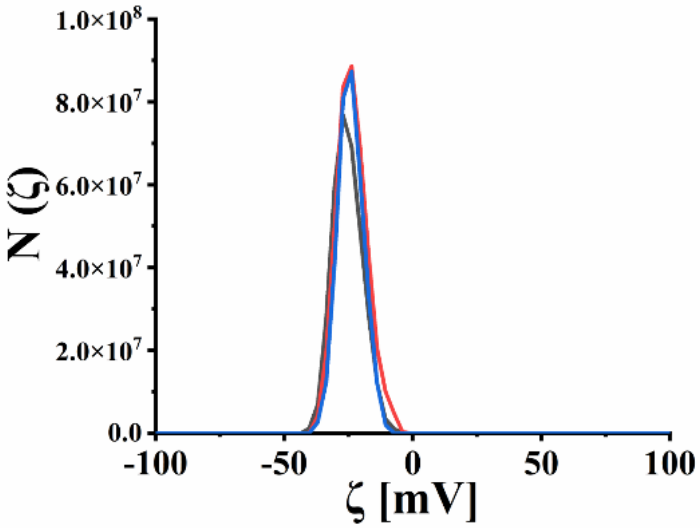

Figure 2.4. Zeta-potential distributions N(ξ) of GNSs in water. The data are based on three repeats of measuring the same samples.

Two different types of capsules were synthesized. Briefly, $CaCO_3$ microparticles (Figure 2.5a and b) were coated with the respective loads (Au nanoclusters, quantum dots and polystyrene fluospheres) by coprecipitation and were used as core templates. The category, size, and excitation/emission wavelength of cargos are listed in Table 1. The microparticles were functionalized with the positively charged polyallylamine hydrochloride (PAH, 56 kDa), the negatively charged polystyrene sodium sulfonate (PSS, 70 kDa) and the negatively charged star-shaped gold nanoparticles using the well-

described LbL method based on the alternating adsorption of different charged polyelectrolytes. Finally, the $CaCO_3$ cores were dissolved with ethylenediaminetetraacetic acid disodium salt (EDTA) in mild conditions to yield the cargos-loaded photothermal-triggered capsules. As shown by SEM and CLSM images (Figure 2.5c and d), the capsules were uniform, well dispersed, and presented spherical shape. The corresponding mean diameter as derived from the size distribution of the $CaCO_3$ cores and capsules were determined to be $d_c = 2.59 \pm 0.22$ μm and $d_c = 4.80 \pm 0.19$ μm, respectively. Calcein was encapsulated within the capsule core as a model cargo by post-loading and heat-shrinking based on the previous report [177].

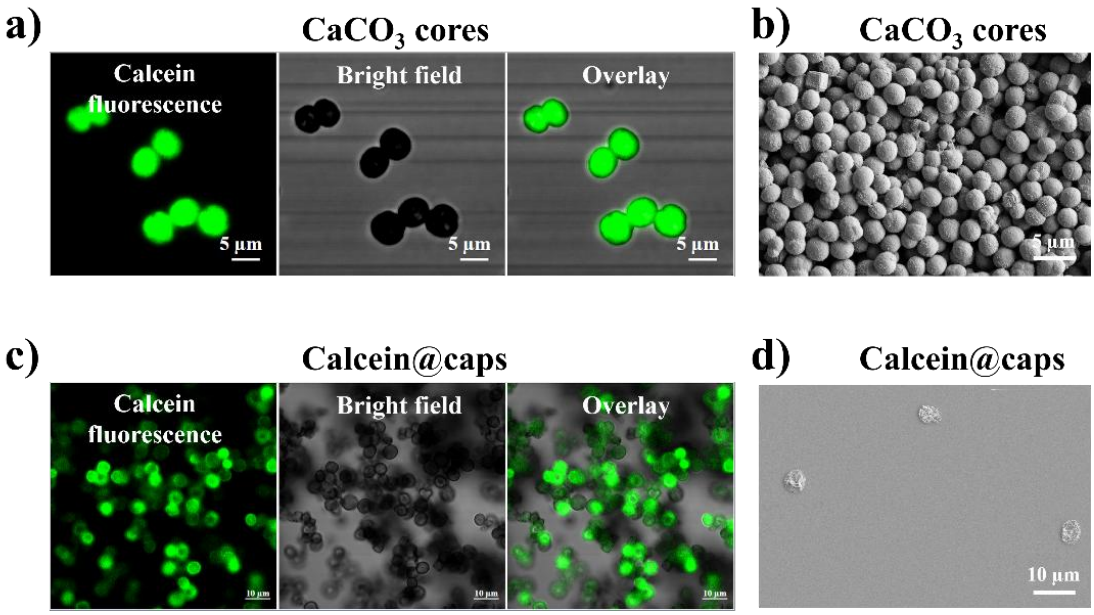

Figure 2.5. Morphology characterization of $CaCO_3$ cores and Calcein@caps. Optical microscopy images (bright-field and FITC fluorescence) of a) $CaCO_3$ cores and c) Calcein@caps. SEM images of b) $CaCO_3$ cores and d) Calcein@caps. The scale bar of $CaCO_3$ cores and Calcein@caps corresponds to 15 μm and 10 nm, respectively.

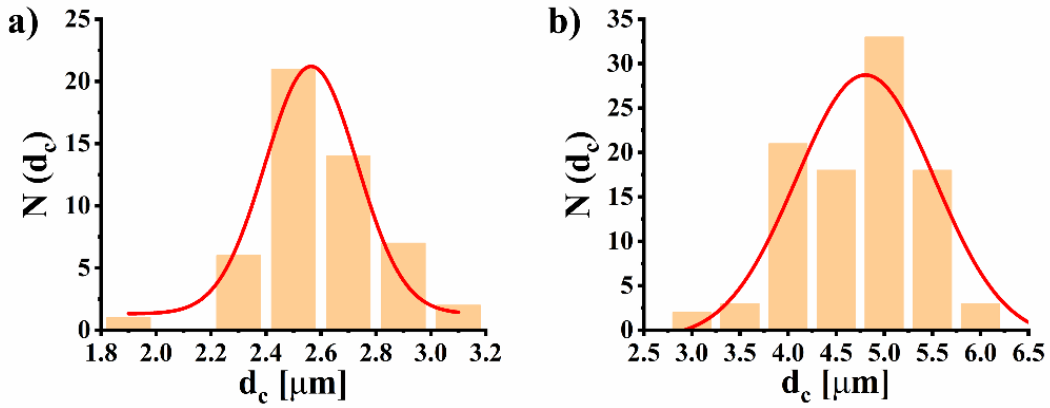

Figure 2.6. For Figures 2.5a and 2.5c, the corresponding distribution $N(d_c)$ in which the number of counts for $CaCO_3$ cores and capsules with a diameter d_c is given.

For characterization of solid nanoparticles, the geometry and the shape of the solid nanoparticles are shown in Figure 2.7. The photophysical characterization of solid nanoparticles is shown in Figure 2.8.

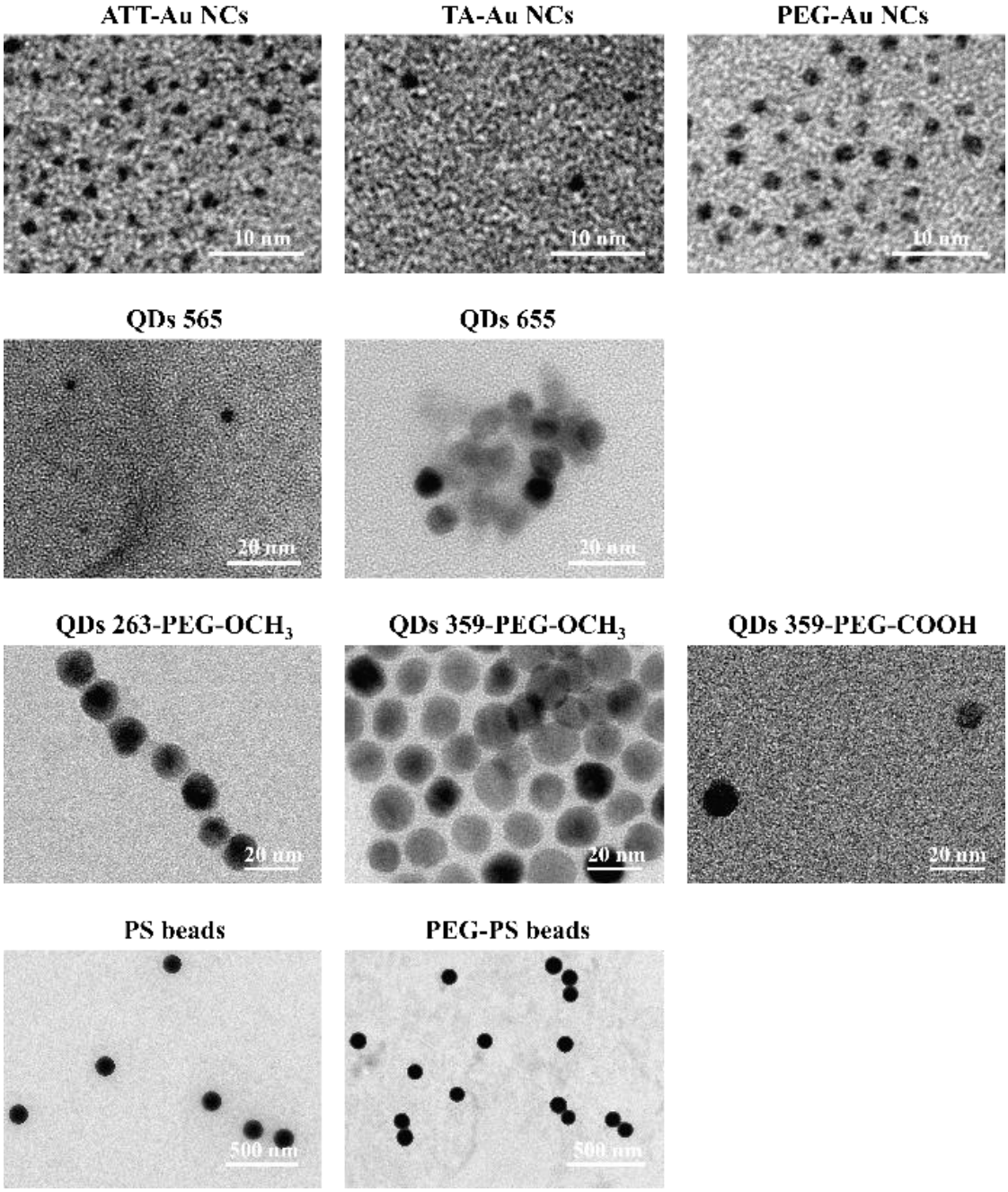

Figure 2.7. TEM images of ATT-Au NCs, TA-Au NCs, PEG-Au NCs, QDs 565, QDs 655, QDs 263-PEG-OCH_3, QDs 359-PEG-OCH_3, QDs 359-PEG-COOH, PS beads and PEG-PS beads. The scale bar of Au nanoclusters, QDs, and PS beads corresponds to 10 nm, 20 nm, and 500 nm, respectively

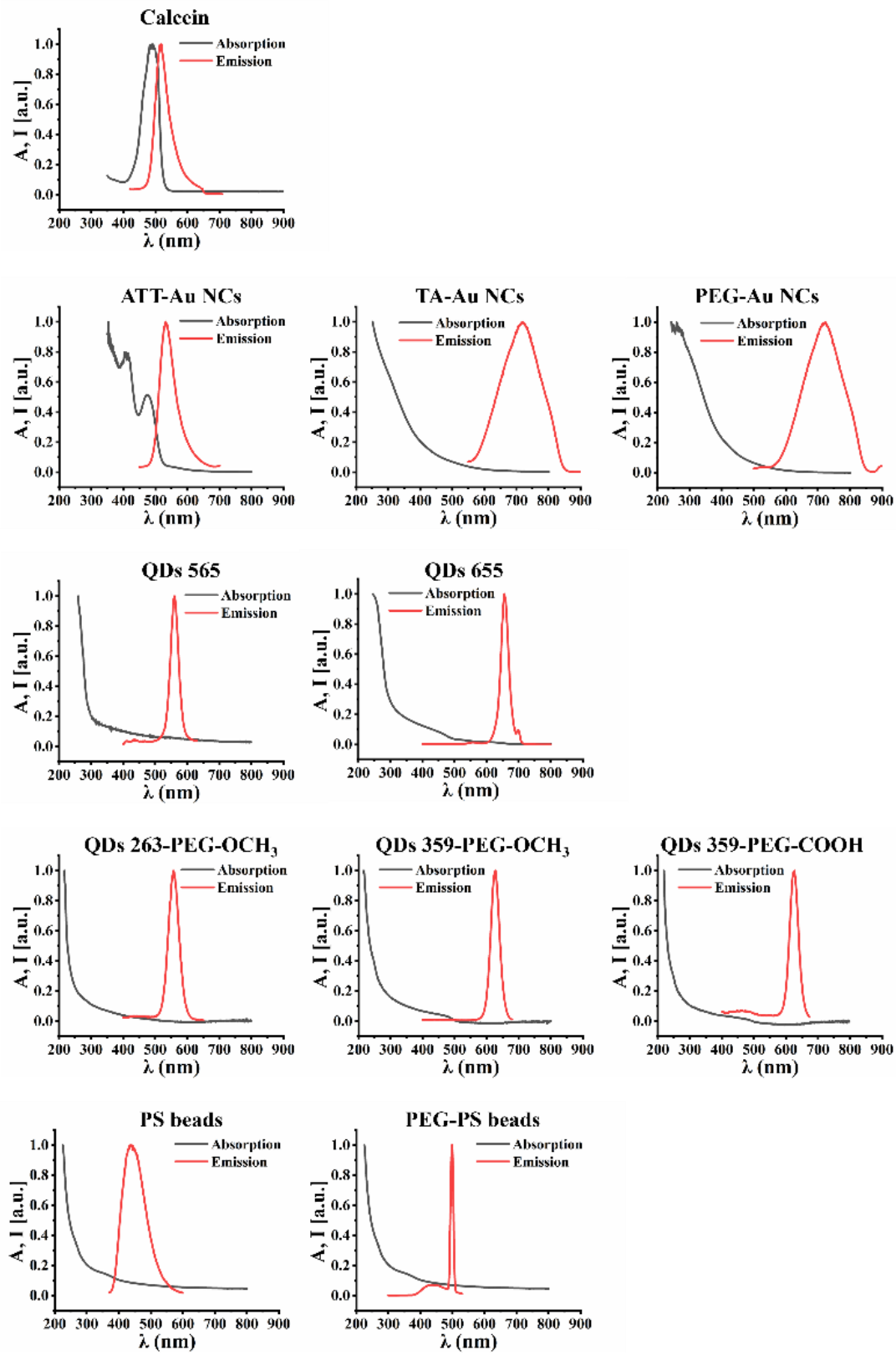

Figure 2.8. Normalized absorption and emission spectra of calcein, Au NCs, QDs and PS beads.

2.3.2 Monitoring the diffusion kinetics of encapsulated molecular cargo

Upon laser irradiation, the photothermal heating of the plasmonic gold nanoparticles can cause transient evaporation of water around the wall of capsules and locally disintegrate the capsules and lysosomal membranes around the respective capsules leading to a release of the cargos into the cytosol. CLSM allows real-time imaging and monitoring of the release behaviour of molecular cargo within cells to analyze the release kinetics. To efficiently open capsules by photothermal heating, calcein-loading capsules were determined in the LSM880. For simultaneously avoiding heat-induced cell death, the paraments of LSM880 set-up are consistent with published work [177]. The laser (P_{laser} = 13.48 mW, E_{laser} = 1.32 mJ) at 830 nm was used for all experiments. As shown in Figure 2.9, the calcein (shown in green false color) was efficiently intracellular released from capsules. The red rectangle indicates the area of irradiated capsules.

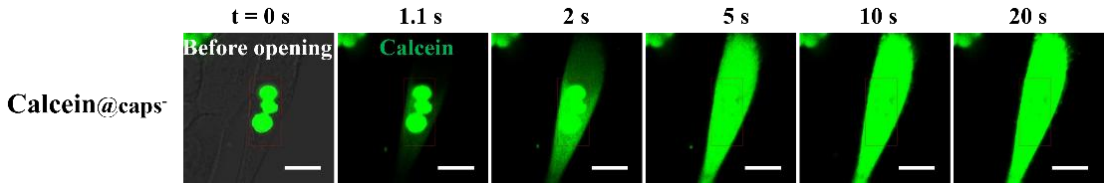

Figure 2.9. Intracellular spread of encapsulated endocytosed calcein into the cytosol. Overlay of bright field and fluorescence channels showing the time-dependent release dynamics of calcein (shown in green) upon capsule irradiation by an 830 nm laser at P_{laser} = 13.48 mW. The scale bars correspond to 10 µm.

2.3.3 Failed release of unmodified solid nanoparticles from caps$^{-/+}$

However, the strategy failed for solid nanoparticles. In our previous study, we established that the failed release of solid nanoparticles is not attributable to the potential interaction between the lysosomal membrane surrounding the endocytosed capsules and the encapsulated molecular cargos [177]. There are two possible reasons for the failure of the release of the solid nanoparticles. The release of nanoparticles might be hindered by their slow diffusion rate and strong attraction to the capsule's inner layer. In our present work, we investigated whether changing the charge of the capsule's inner layer could

reduce attractive interactions between nanoparticles and components of the capsules, thereby improving the diffusion of the particles into the cytosol.

To probe whether this is a possible issue that attractive electrostatic interactions between capsules and cargos impede the release of solid nanoparticles, two calcein-loading capsules with opposite charge polymer as the inner layer were employed for observation of intracellular solid nanoparticles diffusion. The encapsulated calcein was both released from capsules with a negatively charged inner layer ($(PSS/PAH)_2$/GNSs/PAH/PSS shell geometry, cap^-) and a positively charged inner layer ((PAH/PSS/PAH/GNSs/PAH/PSS shell geometry, cap^+) in Figure 2.10. Calcein release was robust and reproducible in both situations with similar release efficiency

For the typical solid nanoparticles, ATT-Au NCs and TA-Au NCs served as the exemplars in this measurement. After laser irradiation, there was no significant release of gold nanoclusters from cap^- or cap^+ both loading with calcein and gold nanoclusters in Figure 2.11.

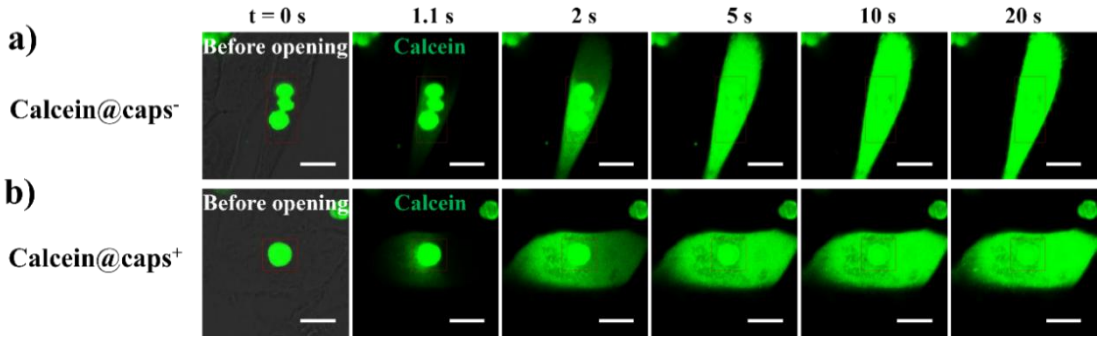

Figure 2.10. Intracellular spread of encapsulated endocytosed calcein in the cytosol after photothermal excitation of the respective capsules with different inner layers of a) PSS and b) PAH, respectively. Overlay of bright field and fluorescence channels showing the time-dependent release dynamics of calcein (shown in green) upon capsule irradiation by an 830 nm laser at P_{laser} = 13.48 mW. The red rectangle indicates the irradiated capsule. The scale bars correspond to 10 µm.

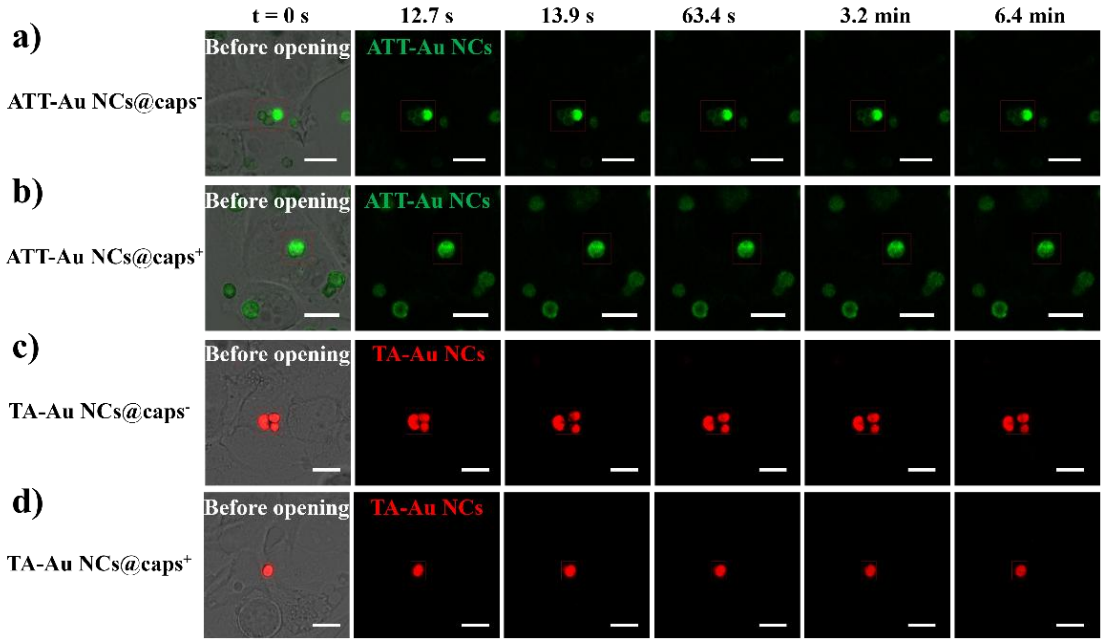

Figure 2.11. Intracellular spread of encapsulated endocytosed ATT-Au NCs in the cytosol after photothermal excitation of the respective capsules with different inner layers of a) PSS and b) PAH, respectively. Intracellular spread of encapsulated endocytosed TA-Au NCs in the cytosol after photothermal excitation of the respective capsules with different inner layers of (c) PSS and (d) PAH, respectively. Overlay of bright field and fluorescence channels showing the time-dependent release dynamics of calcein (shown in green), ATT-Au NCs (shown in green) and TA-Au NCs (shown in red) upon capsule irradiation by an 830 nm laser at P_{laser} = 13.48 mW. The red rectangle indicates the irradiated capsule. The scale bars correspond to 10 µm.

2.3.4 Failed release of unmodified solid nanoparticles (e.g. QDs and PS beads) from capsules

We endeavored to replicate the experiments on commercial quantum dots (QDs, Figure 2.12 and Figure 2.13), and polystyrene fluorophores (PS beads, Figure 2.14) to ascertain whether other larger particles with different coating ligands and sizes could be released from capsules.

To assess the release of commercial QDs, QDs 565 and QDs 655 served as the exemplars for the measurement. The capsules loading with QDs 655 (shown in yellow false colors) or QDs 655 (shown in red false colors) were determined in the LSM880. As

shown in Figure 2.12, the release of endocytosed encapsulated quantum dot was failed. To ensure the opening of the capsule, capsules were co-encapsulated with calcein as a positive reference dye and determined under LSM880 for observation of the intracellular spread of the cargo. As shown in Figure 2.13 (QDs) and Figure 2.14 (PS beads), the fluorescence of the released calcein was promptly detected within ca. 1 s due to its fast diffusion. In contrast, the intracellular QDs 655 and PS beads remained trapped within the opened capsules. Accordingly, attractive electrostatic interactions alone cannot explain the hindered release of nanomaterials in contrast to molecular cargos.

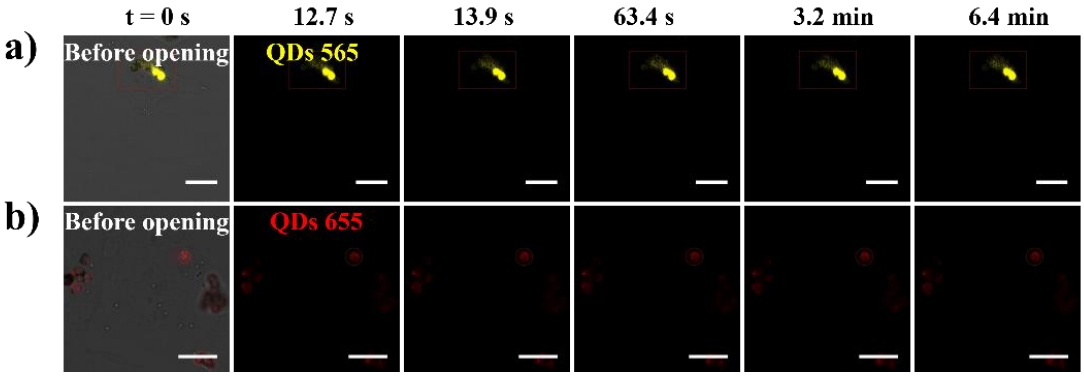

Figure 2.12. Intracellular spread of encapsulated endocytosed a) QDs 565 and b) QDs 655 in the cytosol. Overlay of bright field and fluorescence channels showing the time-dependent release dynamics of Qdots (shown in yellow or red false colors) upon capsule irradiation by an 830 nm laser at P_{laser} = 13.48 mW. The red rectangle indicates the irradiated capsule. The scale bars refer to 10 µm.

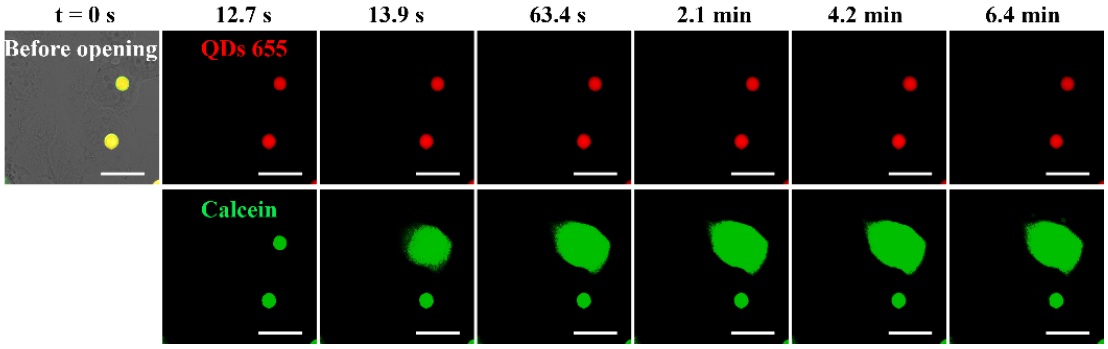

Figure 2.13. Failed photothermal release of endocytosed encapsulated quantum dots. Overlay of bright field and fluorescence channels showing the time-dependent release dynamics of calcein (shown in green) and Qdots 655 (shown in red false colors) upon

capsule irradiation by an 830 nm laser at P_{laser} = 13.48 mW. The red rectangle indicates the irradiated capsule. The scale bars correspond to 10 µm.

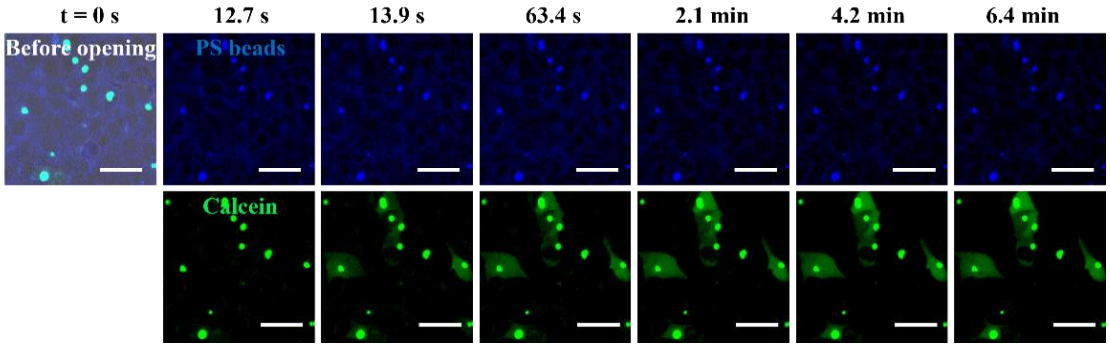

Figure 2.14. Intracellular spread of encapsulated endocytosed fluospheres (PS) beads and calcein in the cytosol. Overlay of bright field and fluorescence channels showing the time-dependent release dynamics of calcein (shown in green) and PS beads (shown in blue false colors) upon capsule irradiation by an 830 nm laser at P_{laser} = 13.48 mW. The red rectangle indicates the irradiated capsule. The scale bars refer to 10 µm.

2.3.5 Data analysis of the diffusion kinetics

The Intracellular spread of encapsulated cargos in the capsules was monitored with fluorescence microscopy at a single-cell level. In this study, the diffusion kinetics of the released molecular cargo within the cell were captured exclusively in two dimensions through fluorescence imaging, confined to the focal plane of the microscope. Time-series of the spread of the fluorescent released molecular cargo were recorded through fluorescence imaging (eg. Figure 2.10b). The use of the widely used open-source image analysis tool, ImageJ/Fiji [205], extracted information from microscopy data and provided a quantitative assessment of microscopy data. Two quantifiers were identified: the time-dependent fraction of the fluorescence present area and the time-dependent fraction of the mean fluorescence intensity in the cellular cross-section. During the initial 10 frames of NIR laser activation, the area occupied by the fluorescence (i.e., the area size of the capsule) and the mean fluorescence intensity were averaged and defined as the background value. Subsequent to the activation of the laser, the area occupied by the fluorescence and the mean fluorescence intensity are recorded at all time points. Followed

by subtracting by the background value, two values were extracted: the mean fluorescence intensity of the released molecular cargo (I(t)) and the area of the released molecular cargo (A(t)). I(t) and A(t) saturated eventually to the values I_{max} and A_{max}, respectively. $I(t)/I_{max}$ and $A(t)/A_{max}$ were collected by normalizing the data to their maximum values. As shown in Figure 2.15, the normalized data of released calcein was plotted over time. The extraction of two parameters, designated $t_{0.9\text{-}0.1}(I)$ and $t_{0.9\text{-}0.1}(A)$, was conducted from each curve to delineate the duration preceding the augmentation of intensity and fluorescent area from 10% to 90%.

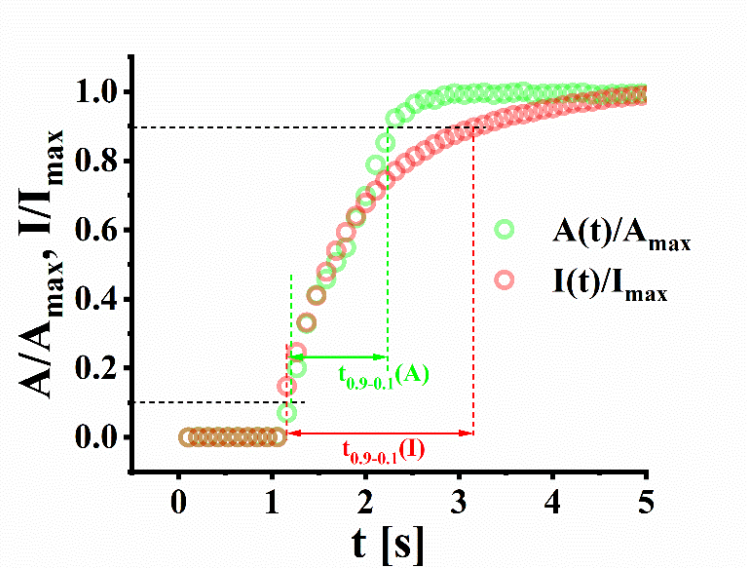

Figure 2.15. Normalized release intensity I/I_{max} and spreading area in the cytosol A/A_{max} as a function of time after photothermal opening. The data shown here were derived from Figure 2.10b.

2.3.6 Release of PEGylated solid nanoparticles from capsules

All release data of all the investigated PEGylated solid nanoparticles shown in Table 1 are provided here (Figure 2.16, Figure 2.17 and Figure 2.18). For each tested molecular cargo that was subjected to testing, a minimum of five capsule opening events were recorded. The recorded normalized release intensities I/I_{max} and spreading areas A/A_{max} were subsequently obtained. To further assess the time of the intracellular release and spreading of PEGylated solid nanoparticles, $t_{0.9\text{-}0.1}(I)$ and $t_{0.9\text{-}0.1}(A)$ were extracted in Figure 2.19. Calcein was used as a reference molecular cargo to confirm the intracellular

opening of the capsules in the experiments. There were incompatibilities between those molecular cargos and calcein (e.g., overlapping fluorescence spectra. Table 1).

Calcein was released in a rapid and complete filling of the entire cytosol, with the process being completed within approximately 0.9 s. Subsequent to this initial phase, the integrated intensity of the calcein remained constant. The fluorescence signal of calcein was saturated at the beginning, but a decline in fluorescence signal intensity in various degree is observed. The potential explanation for the decline in calcein fluorescence over time is that severe photobleaching during imaging or photothermal-induced cell membrane perforation results in the release of calcein into the extracellular environment. In contrast, different spatiotemporal spread of the investigated PEGylated solid nanoparticles (PEG-Au NCs in Figure 2.16, PEG-QDs in Figure 2.17 and PEG-PS beads in Figure 2.18) and calcein were observed. Ongoing spread of the released dyes throughout the cytosol occurred with varying rates of kinetics.

Normalized area A/A_{max} and integrated fluorescence intensity I/I_{max} of the average value for these three solid nanoparticles co-loading with calcein were shown in Figure 2.19a-c. The $t_{0.9\text{-}0.1}$(A) values of PEG-Au NCs, PEG-QDs and PEG-PS beads were calculated as 39.83 s, 385.00 s and 422.83 s, respectively. The $t_{0.9\text{-}0.1}(I)$ values of PEG-Au NCs, PEG-QDs and PEG-PS beads were 187.83 s, 463.60 s and 537.50 s, respectively, see Figure 2.19d-e. Those data indicated that PEGylation of solid nanoparticles facilitates an efficient photothermally triggered release from capsules and lysosomes into the cytosol of these materials.

In contrast, all solid nanoparticles with PEG-coating were successfully released into the cytosol. Even the comparably large PS beads were smoothly released from the capsules and diffused into the cytosol. Coating nanoparticles with PEG could enhance their diffusivity in water, despite an increase in their dimensions. The physics of this effect is currently not fully clear but may be related to the lubricating properties of this coating [206]. The observed differences in release kinetics can be rationalized with size effect. The smallest particles, Au NC, are released faster and spread faster than the bigger particles due to their larger diffusivity. Attractively, we also specifically explored the possible enhancing mechanism of diffusion from molecular dynamic (MD) perspective, which is demonstrated in §2.3.8 and §2.3.9.

As an example, we describe the experiments with co-encapsulated calcein and PEG-PS beads. Figure 2.18 presents the real-time imaging of the release of the co-encapsulated calcein and PEG-PS beads from the capsules and the lysosomes. We extracted the values of intracellular fluorescence integrated intensity/area to analyse the release kinetics. As shown in Figure 2.18b-e, the normalized integrated fluorescence intensity I/Imax and area A/Amax are used to represent the release kinetics. The spread of calcein was observed within 1 s. After the intracellular fluorescence area A and integrated intensity I reached their maximum, a slight decrease of these values was observed, which might be attributed to some photobleaching under continuous imaging by using the LSM880 set-up. At the end of the observation period of ~ 13 min, the fluorescence of calcein inside the capsules was still strong. This is consistent with previous reports that the cargo may bind to the polyelectrolyte matrix within the capsule, hindering cargo release [177]. In contrast, the ongoing spread of PEG-PS beads across the cytosol happened with different kinetics, and the PEG-PS beads rapidly filled the entire cytosol already within ≈ 1 min. After 10 min, the significant increase of intracellular fluorescence area A and the intensity I of the PEG-PS bead reached their maximum, and the integrated intensity and spread area of the PEG-PS bead remained basically constant afterwards due to the nanobeads' high photostability. The PEG-PS bead fluorescence inside and outside the capsule was roughly the same at the end of the experiment. Considering that these beads without PEG-coating were not released at all, these results indicate a crucial role of PEGylation in ensuring intracellular mobility after capsule opening. Reasons for this could be a reduced absorption to remaining capsule fragments (polyelectrolytes as well as Au NP aggregates) after opening, but also to cellular components. Additionally, PEGylation is well-known to provide enhanced colloidal stability which might also play a role in the observed effect. If particles are destabilized during the photothermal capsule opening process, they might form aggregates which are immobilized due to their size.

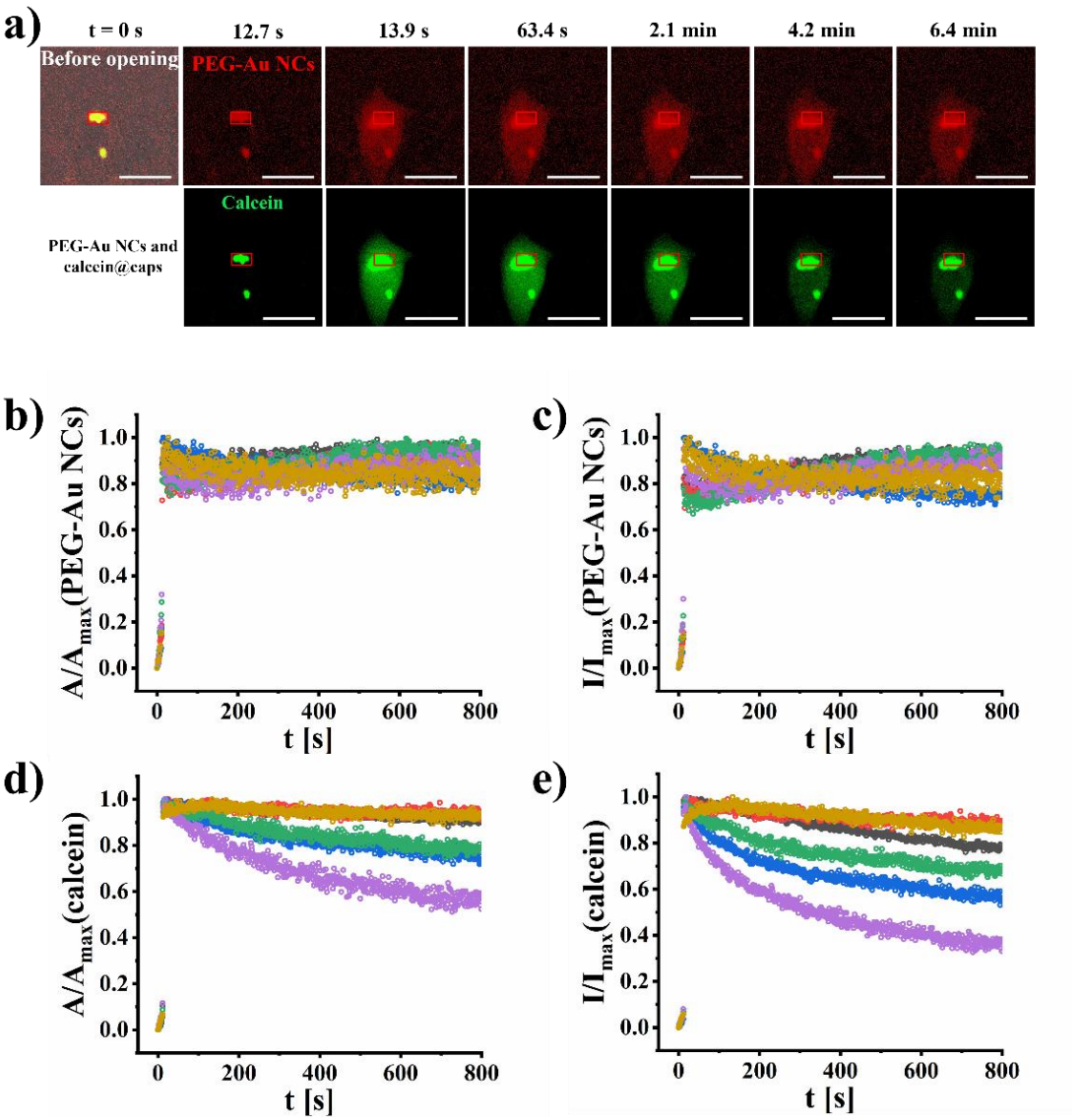

Figure 2.16. a) Intracellular spread of encapsulated endocytosed PEG-Au NCs and calcein in the cytosol. Overlay of bright field and fluorescence channels showing the time-dependent release dynamics of calcein (shown in green) and PEG-Au NCs (shown in red false colors) upon capsule irradiation by an 830 nm laser at P_{laser} = 13.48 mW. The red rectangle indicates the irradiated capsule. The scale bars refer to 20 µm. b,c,d,e) Release kinetics as obtained for the release of PEG-Au NCs and calcein upon different events of photothermal heating. Normalized integrated fluorescence intensity I/I_{max} of one cell, as calculated as the normalized integral of the local fluorescence intensities across the cell, as a function of time. Normalized area A/A_{max} of one cell, which is reached by the released fluorophores, as a function of time. Each curve corresponds to one experiment, from which the parameters $t_{0.9\text{-}0.1}(I)$ and $t_{0.9\text{-}0.1}(A)$ were extracted.

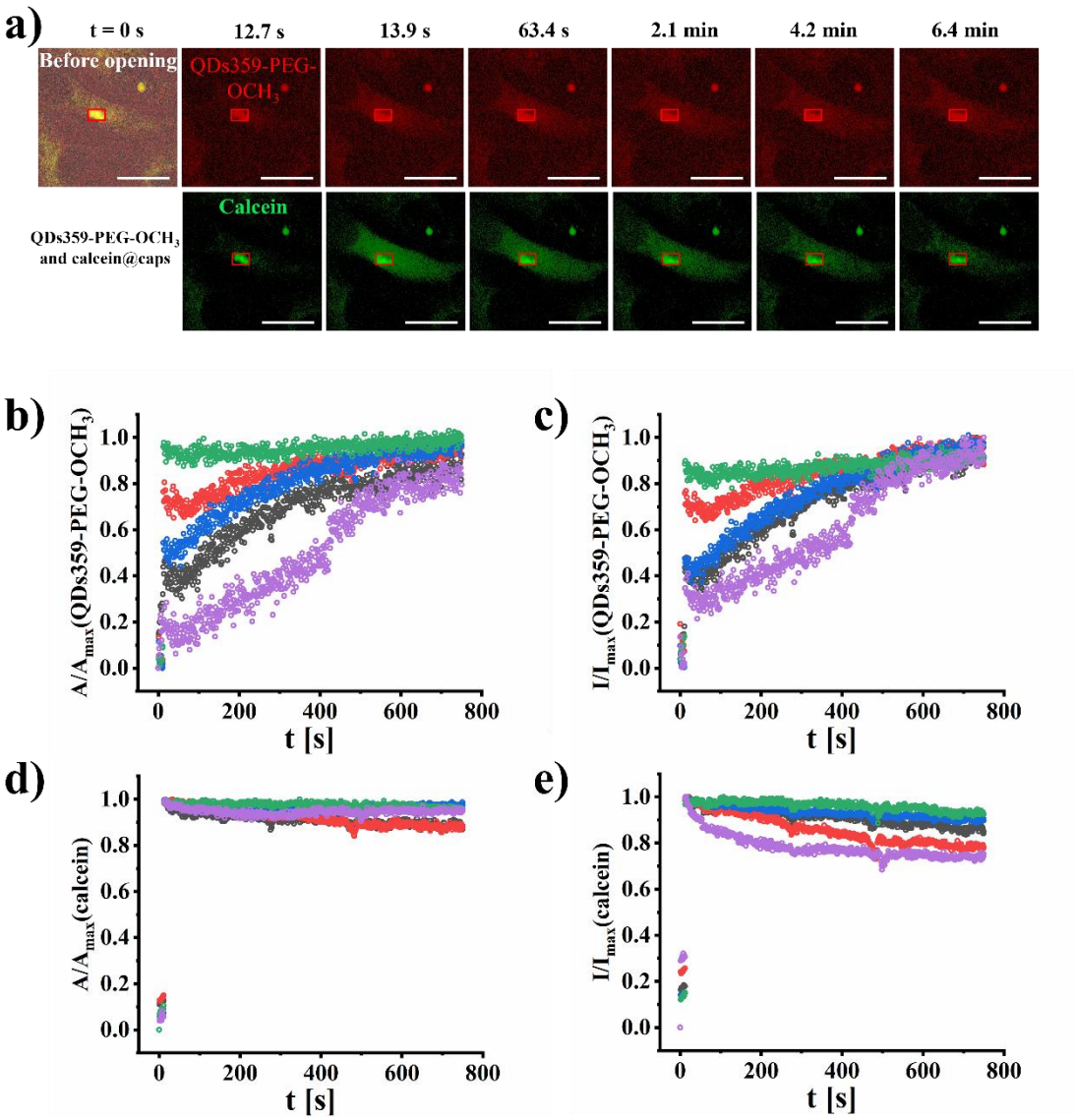

Figure 2.17. a) Intracellular spread of encapsulated endocytosed QDs359-PEG-OCH_3 and calcein in the cytosol. Overlay of bright field and fluorescence channels showing the time-dependent release dynamics of calcein (shown in green) and QDs359-PEG-OCH_3 (shown in red false colors) upon capsule irradiation by an 830 nm laser at P_{laser} = 13.48 mW. The red rectangle indicates the irradiated capsule. The scale bars refer to 20 µm. b,c,d,e) Release kinetics as obtained for the release of QDs359-PEG-OCH_3 and calcein upon different events of photothermal heating. Normalized integrated fluorescence intensity I/I_{max} of one cell, as calculated as the normalized integral of the local fluorescence intensities across the cell, as a function of time. Normalized area A/A_{max} of one cell, which is reached by the released fluorophores, as a function of time. Each curve corresponds to one experiment, from which the parameters $t_{0.9\text{-}0.1}(I)$ and $t_{0.9\text{-}0.1}(A)$ were extracted.

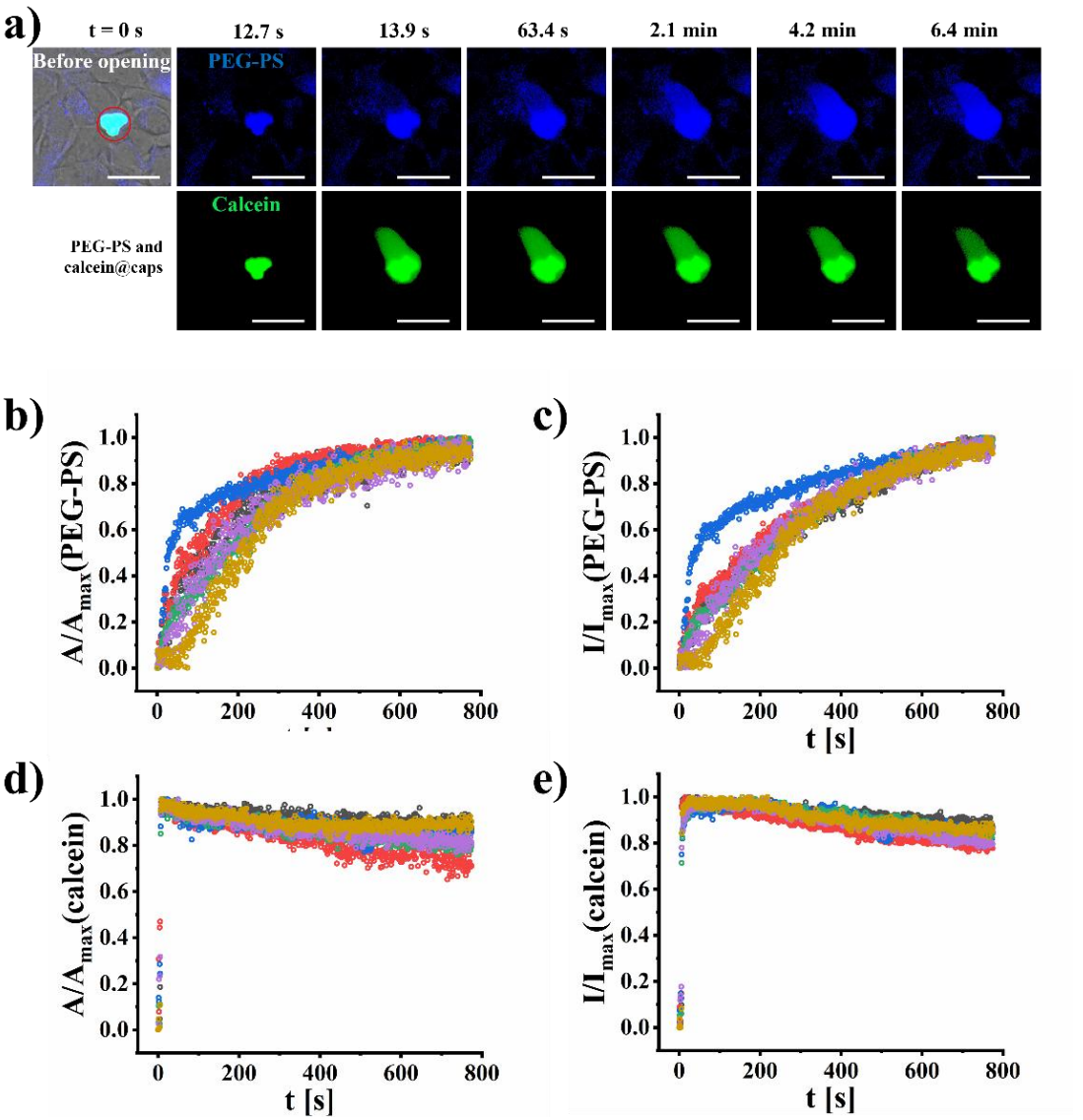

Figure 2.18. a) Intracellular spread of encapsulated endocytosed PEG-PS beads and calcein in the cytosol. Overlay of bright field and fluorescence channels showing the time-dependent release dynamics of calcein (shown in green) and PEG-PS beads (shown in blue false colors) upon capsule irradiation by an 830 nm laser at P_{laser} = 13.48 mW. The red circle indicates the irradiated capsule. All scale bars: 20 µm. b,c,d,e) Release kinetics as obtained for the release of PEG-PS beads and calcein upon different events of photothermal heating. Normalized integrated fluorescence intensity I/I_{max} of one cell, as calculated as the normalized integral of the local fluorescence intensities across the cell, as a function of time. Normalized area A/A_{max} of one cell, which is reached by the released fluorophores, as a function of time. Each curve corresponds to one experiment, from which the parameters $t_{0.9\text{-}0.1}(I)$ and $t_{0.9\text{-}0.1}(A)$ were extracted.

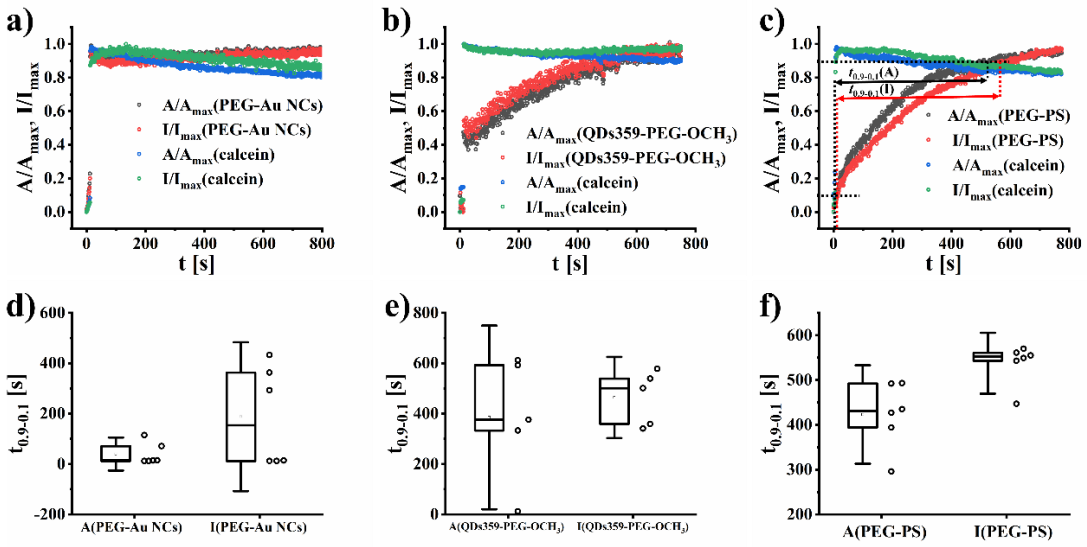

Figure 2.19. Normalized area A/A_{max} and integrated fluorescence intensity I/I_{max} of the average value, which is obtained from the released a) PEG-Au NCs and calcein, b) QDs359-PEG-OCH_3 and calcein, c) PEG-PS beads and calcein, as a function of time. Summary of the results for the $t_{0.9\text{-}0.1}(I)$ and $t_{0.9\text{-}0.1}(A)$ values of d) PEG-Au NCs, e) Qds359-PEG-OCH_3 and f) Qds359-PEG-COOH. The data were obtained from Figure 2.16, Figure 2.17 and Figure 2.18.

2.3.7 Release and analysis of solid nanoparticles with different terminal groups in ligands

In order to verify whether the intracellular release of solid nanoparticles to cytosol is affected by different terminal groups in ligands, QDs, a prototypical class of solid nanoparticles, were selected as the object of study in this investigation. QDs263-PEG-OCH_3, QDs359-PEG-OCH_3 and QDs359-PEG-COOH were employed to encapsulate into capsules. For each tested molecular cargo that was subjected to testing, a minimum of ten capsule opening events were recorded. Images (bright field and fluorescence) were recorded at different time points and corresponding $t_{0.9\text{-}0.1}(I)$ and $t_{0.9\text{-}0.1}(A)$ values of QDs were obtained in Figure 2.20. The release kinetics of the encapsulated QDs, Normalized area A/A_{max} and integrated fluorescence intensity I/I_{max} of the average value for these three solid nanoparticles are shown in Figure 2.20. The $t_{0.9\text{-}0.1}$(A) values of QDs263-PEG-

OCH_3, QDs359-PEG-OCH_3 and QDs359-PEG-COOH were calculated as 761.10s, 825.67 s and 1208.42 s, respectively. The $t_{0.9\text{-}0.1}(I)$ values of QDs263-PEG-OCH_3, QDs359-PEG-OCH_3 and QDs359-PEG-COOH were 825.70 s, 903.25 s and 1325.58 s, respectively. The diffusion speed of PEGylated QDs is significantly faster than that of hydroxyl groups, which may be caused by the difference in the hydrophilicity of nanoparticles. More exploration will be presented in §2.3.8 and §2.3.9.

Co-encapsulation of a reference dye (calcein) with the cargo being tested is a good way to measure the release of the encapsulated cargo. Compared with Figure 2.17 and Figure 2.21, it is noteworthy that the release rate of cargos in the presence of calcein is significantly higher than that in the absence of calcein. This topic will be discussed in more detail in §2.3.8 and §2.3.9.

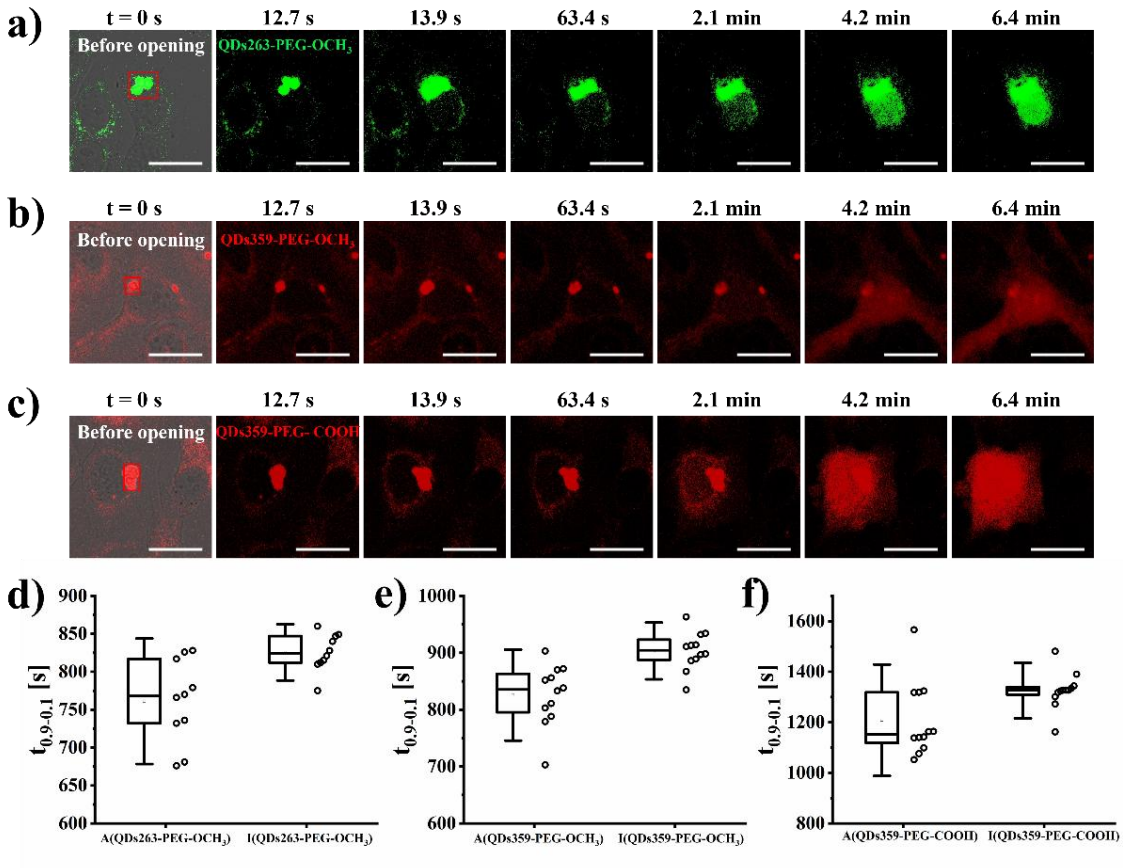

Figure 2.20. Intracellular spread of encapsulated endocytosed a) QDs263-PEG-OCH_3, b) QDs359-PEG-OCH_3 and c) QDs359-PEG-COOH in the cytosol. Overlay of bright field and fluorescence channels showing the time-dependent release dynamics of QDs263-PEG-OCH_3 (shown in green), QDs359-PEG-OCH_3 (shown in red) and QDs359-PEG-

COOH (shown in red false colors) upon capsule irradiation by an 830 nm laser at P_{laser} = 13.48 mW. The red rectangle indicates the irradiated capsule. The scale bars refer to 20 µm. Summary of the results for the $t_{0.9\text{-}0.1}(I)$ and $t_{0.9\text{-}0.1}(A)$ values of endocytosed d) QDs263-PEG-OCH_3, e) QDs359-PEG-OCH_3 and f) QDs359-PEG-COOH as obtained from the data shown in Figure 2.20.

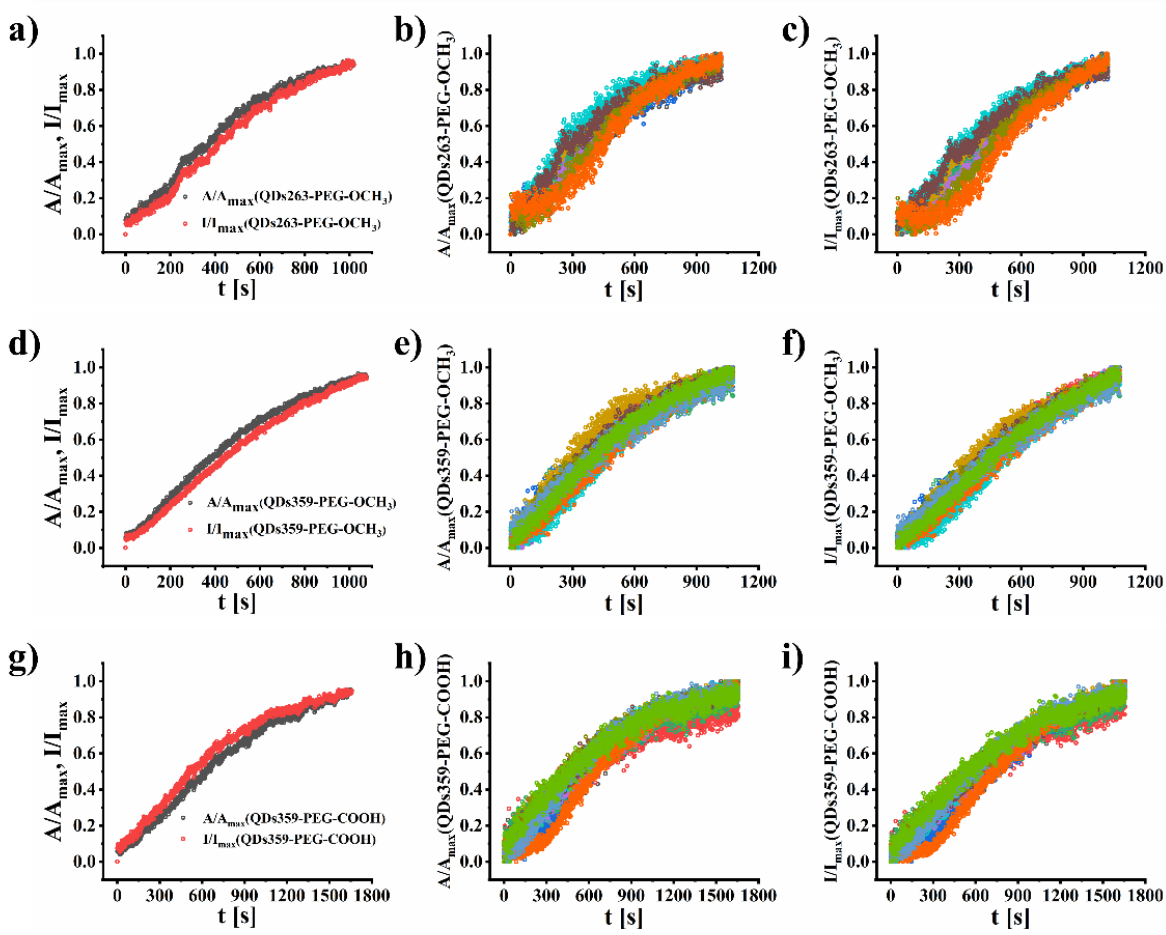

Figure 2.21. Release kinetics as obtained for normalized release intensities I/Imax and intracellular spreading areas A/Amax of b) and c) QDs263-PEG-OCH_3, e) and f) QDs359-PEG-OCH_3, and, h) and i) QDs359-PEG-COOH upon different events of photothermal heating. Each curve corresponds to one experiment, from which the parameters $t_{0.9\text{-}0.1}(I)$ and $t_{0.9\text{-}0.1}(A)$ were extracted. a), d) and g) The curves show the average value from all traces in (c, d), (e, f) and (h, i), respectively.

2.3.8 Investigation on possible enhancing mechanism of diffusion

In order to elucidate the effect of PEGylation in the release experiments, Molecular Dynamics (MD) simulations were carried out. Gold nanocluster (Au NC) was designated to be the candidate attributing to the more well-defined and stable structures than QDs. Figure 2.22a-c show the equilibrium geometries of the Au NC with different ligands, namely TA, TA-PEG-OCH_3 and TA-PEG-COOH, respectively. The optimized conformations of the different ligands is shown in Figure 2.22d. By calculating the solvent interaction energies of gold nanoclusters with different terminal-group of PEG ligands, the total interaction energy was increased from -4095.724 kJ/mol (Au-TA NCs) to -22906.627 kJ/mol (Au NCs-TA-PEG-OCH_3) and -23828.778 kJ/mol (Au NCs-TA-PEG-COOH) (Figure 2.22f). Meanwhile, the Van der Waals interactions between the ligand coatings of the Au NC and water changed from repulsion in case of TA (399.572 kJ/mol) to attraction (-2540.540 kJ/mol and -2416.507 kJ/mol, respectively) in case of the PEG-coatings (Figure 2.22e). This finding is consistent with the observed difficulty in diffusion on the release experiment of TA-Au NCs. The simulation results and experimental results consistently demonstrate that PEGylation significantly improves the release and intracellular diffusion of nanoparticles. Furthermore, the interaction energies of the different terminal-groups modified PEG short chains with water were investigated, which the short chains were extracted from the stable conformation of Au NCs with approximated relative molecular weight of Calcein. Intriguing, the -COOH terminated PEG short chain exhibited the strongest interaction with water (-546.677 kJ/mol), which was 70-80 kJ/mol stronger than that of -OCH_3 terminal-group modified PEG short chain and calcein (a quite fast releasing small molecules as mentioned above) (Figure 2.22g). Thus, PEG modification can be considered to effectively enhance the interaction of the cargos with water, and -COOH terminated PEG can be considered as the best candidate for hydrophilic surface modification of cargoes, endowing nanoclusters with better application potential. We note that the better solubility in water is also directly related to colloidal stability, because decreased solubility increased the probability of agglomeration, aggregation, and precipitation.

Comparing the intracellular release of endocytosed encapsulated quantum dots with differently terminated PEG coatings led to contrary conclusions (Figure 2.20 and Figure 2.21). The intracellular spread of QDs-PEG modified with -OCH_3 terminal-groups was faster than for those with -COOH groups. As shown in Figure 2.21, -OCH_3

terminated QDs-PEG was therefore considered to exhibit stronger interaction with water and better release properties than the -COOH terminated ones. Considering the possible excess ligand coating of the nanocluster surface in the experiments, zeta potentials of different PEG grafting QDs were further conducted to explain the paradoxical phenomenon. QDs-PEG-OCH_3 exhibited stronger surface negativity (-13.14 ± 0.30 mV) than QDs-PEG-COOH (-9.47 ± 0.80 mV) (Figure 2.23), which successfully supported the excessive coating hypothesis. Hence, the unexpectable coating of un-grafted ligands on the material surface was also one of the important influencing factors to achieve controlled release modulation of cargoes.

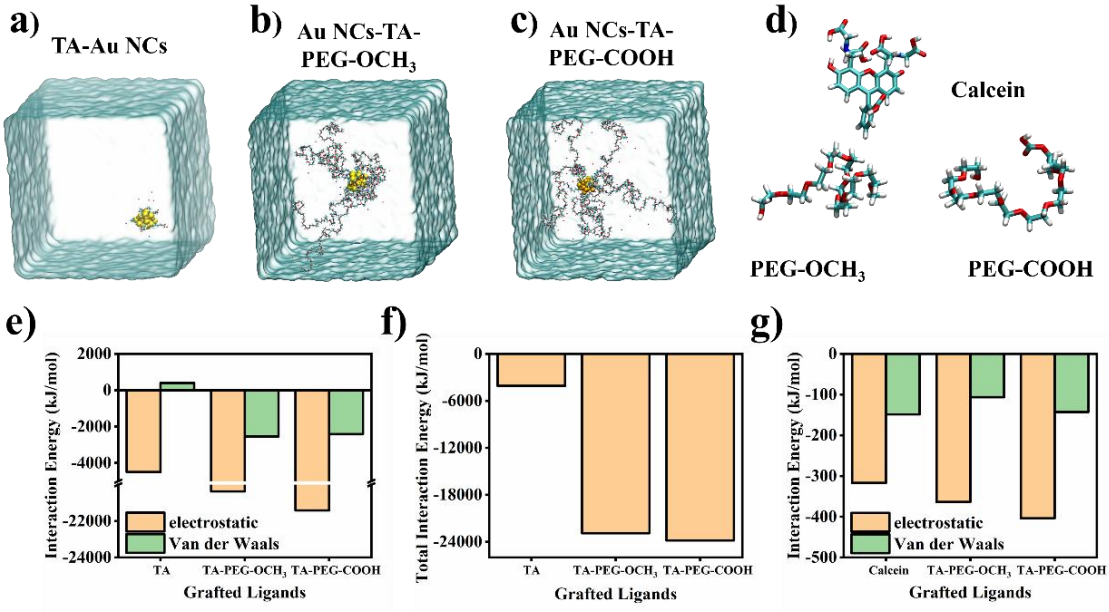

Figure 2.22. The equilibrium geometry of gold nanoclusters with different ligands: a) TA; b) TA-PEG-OCH_3; c) TA-PEG-COOH. d) The equilibrium conformation of PEG-OCH_3, PEG-COOH and calcein. The interaction energy between gold nanoclusters with different ligands and water: e) electrostatic interactions and Van der Waals interactions; f) total interactions. g) The interaction energy between different terminal end chains and water, in which calcein was designated as control and the same molecular weight was employed.

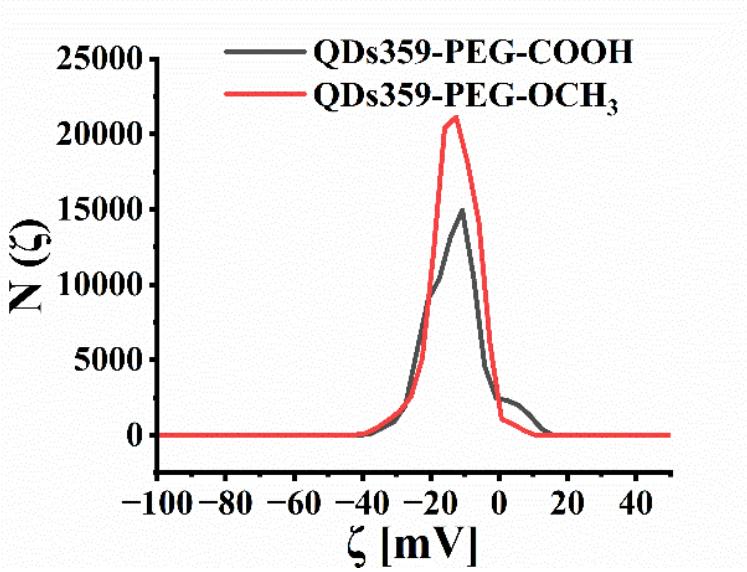

Figure 2.23. The mean zeta-potentials of the Au NCs-PEG-COOH and Au NCs-PEG-OCH_3 were -9.17 ± 0.80 and -13.14 ± 0.30 mV, respectively.

2.3.9 Effect of calcein co-loading on intracellular diffusivities

The above results consistently demonstrate that PEGylation significantly improves the release and intracellular diffusion of nanoparticles. Surprisingly, the release and diffusion kinetics were strongly affected by calcein co-loading. When capsules were loaded with a combination of calcein and PEGylated nanoparticles, the release took place within seconds as shown in Figure 19a-c (PEG-Au NCs, PEG-QDs and PEG-PS beads). In contrast, it took a few minutes to observe significant release of PEGylated nanoparticles when no calcein was co-encapsulated.

To explore possible reasons for this behavior the calcein adsorption was simulated with the Au NC model described in Figure 2.22. The stable adsorption model was first simulated for 10 ns, then removed all unattached calcein and simulated for 10 ns to remove the unstable adsorption calcein by twice, which better represented the reality drug loading processes of capsule construction (Figure 2.24a). Compared to the pure Au NC, the interaction energy of calcein/Au NC mixtures with water was significantly increased (from -23828.778 kJ/mol to -40740.616 kJ/mol) (Figure 2.24b). The promoting effect of hydrophilic small molecule adsorption on the release properties of cargoes was primarily

enunciated. In this case, the increase in the interaction energy of the gold cluster system with water was mainly due to strong interactions of the small molecules-small molecules and small molecules- cargoes. Although calcein had a lower interaction capacity with water than PEG, more calcein tended to aggregate and gained stronger interaction with water than single PEG with the strong interactions of the small molecules-small molecules (Figure 2.24c), which ultimately realized the enhancement of hydrophilicity (Figure 2.24d).

Moreover, since the complexity component of cytoplasm, the stable adsorption of the calcein to the PEG coating might also diminish the unspecific adsorption to other stuff (such as the protein, the shatter fragments of the capsules and aggregated Au NP) caused by the light lasering. In summary, we initially proposed a regulatory strategy to achieve the on-demand release.

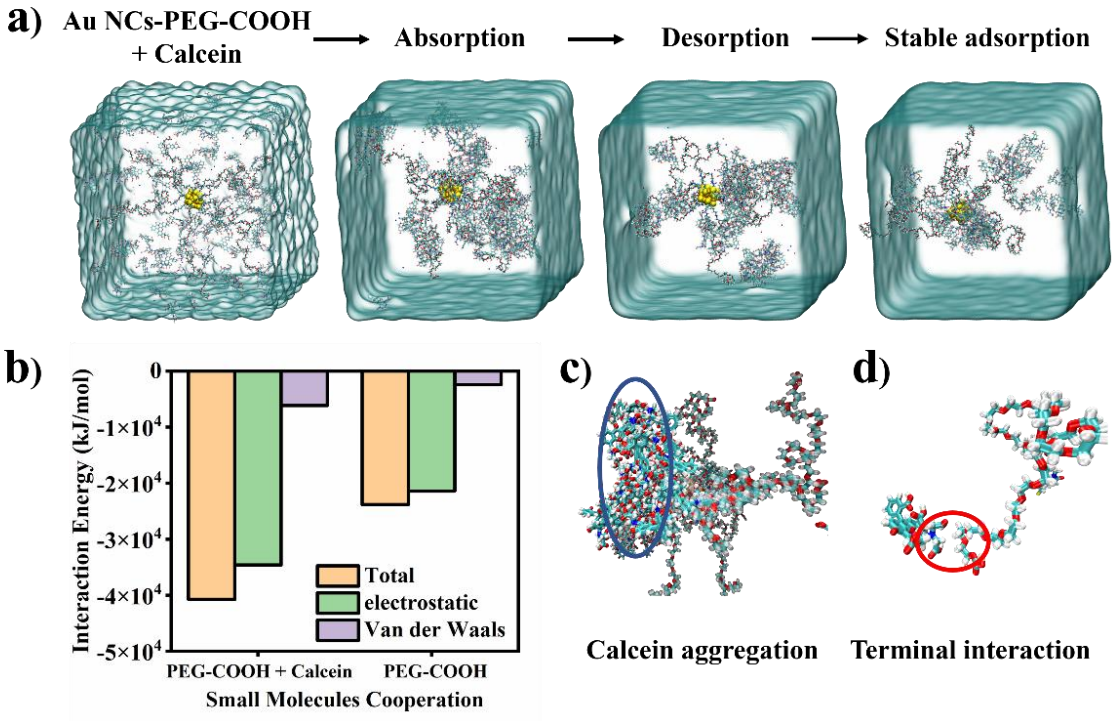

Figure 2.24. a) The stable absorption process of Au NCs-PEG-COOH with calcein. b) The total, electrostatic interaction, Van der Waals interaction energy between water and Au NCs-PEG-COOH with/without calcein. The interaction snapshot of c) calcein aggregation and d) electrostatic interaction between the terminal group of PEG-COOH and calcein.

2.4 Conclusion

In this work, we present data on the intracellular light-triggered release of different nanomaterials, ranging from small nanoclusters with hydrodynamic diameters well below several nm to poly(styrene) spheres with diameters of 100 nm. For all solid nanoparticles tested, the efficient release was enabled by poly(ethylene glycol) coatings in contrast to all other tested coatings. Molecular dynamics (MD) simulations further clarified that PEG modification was considered to effectively enhance the interaction of the cargos with water. Quantitative analysis reveals that intracellular diffusion performance of nanoparticles is dependent on the size of nanoparticles. PEGylation nanoparticles with OCH_3 terminal-groups showed better release performance than the COOH terminal-group modification, as the simulation clarified that the terminal group is a significant impact factor for the intracellular diffusion of nanoparticles with approximated relative nanoparticles. PEGylation nanoparticles with unstable interaction based on calcein stick gained stronger interaction with water, which means that calcein doping PEGylation nanoparticles could reverse the low diffusion performance. Hence, calcein-mediated PEGylation nanoparticle delivery could represent a potential solution for the bottleneck of cytosolic delivery, enhance the intracellular release of the nanoparticles from the endosome to the target position, and further enhance nanoparticle delivery efficiency.

3 Microcapsule-mediated engineered cells for intracellular nanoplastic biodegradation

3.1 Introduction

The widespread use of plastics has led to an inevitable increase in human exposure to plastic particles worldwide [207, 208]. Microplastics and nanoplastics have emerged as novel particulate anthropogenic pollutants, rapidly gaining attention from both the scientific community and the general public [209-211]. When exposed to biological, chemical, and environmental factors, a single microplastic particle can fragment into billions of nanoplastic particles, suggesting that nanoplastic pollution will become ubiquitous on a global scale [212, 213]. Due to their minute size, nanoplastics may pose greater risks than microplastics, as they can penetrate biological membranes [214-217]. These particles have been detected not only in diverse environmental matrices but also in drinking water and food chains, raising significant concerns about their potential impacts on human health. Concurrently, the massive production of plastics presents formidable challenges for waste management [218].

Traditional approaches for nanoplastic remediation predominantly employ physical and chemical methodologies [219, 220]. Photocatalytic degradation utilizing titanium dioxide nanoparticles under ultraviolet irradiation demonstrates efficacy in mineralizing polyethylene into benign byproducts [221]. Mechanical techniques such as ultrasonication facilitate polymer chain scission, while advanced oxidation processes including Fenton reactions mediate oxidative breakdown through hydroxyl radical generation [222, 223]. Hydrolytic methods employing strong acids or bases target ester linkages in polyesters [224]. However, these strategies are constrained by several factors: the persistence of catalytic residues, formation of toxic intermediates, requirements for corrosive reagents, and incompatibility with biological systems [225, 226]. In contrast, biological degradation platforms, particularly enzyme-based systems, offer environmentally benign alternatives [227, 228]. Notable examples include PETase derived from Ideonella sakaiensis and genetically engineered Escherichia coli exhibiting surface-displayed PETase with 328-fold enhanced degradation efficiency [229]. Despite these advancements, a significant knowledge gap persists regarding intracellular nanoplastic degradation within mammalian systems.

To address this critical unmet need, we have developed a biomimetic degradation platform employing layer-by-layer assembled polyelectrolyte capsules. These nanostructured vehicles, designated as $(DEXS/pARG)_2/(DEXS/PEI)_2$@PETase, are rationally designed for lysosomal trafficking following cellular internalization (Figure 3.1). The system capitalizes on two synergistic mechanisms: first, the acidic lysosomal microenvironment induces capsule disassembly, and second, the intrinsic proton buffering capacity of polyethyleneimine maintains optimal pH for PETase activity. This dual-function architecture ensures both spatial and temporal control of enzymatic payload release, enabling efficient intracellular plastic degradation. The platform's biological compatibility and targeted delivery represent significant advancements over conventional degradation methods, establishing a novel paradigm for addressing nanoplastic accumulation in living systems.

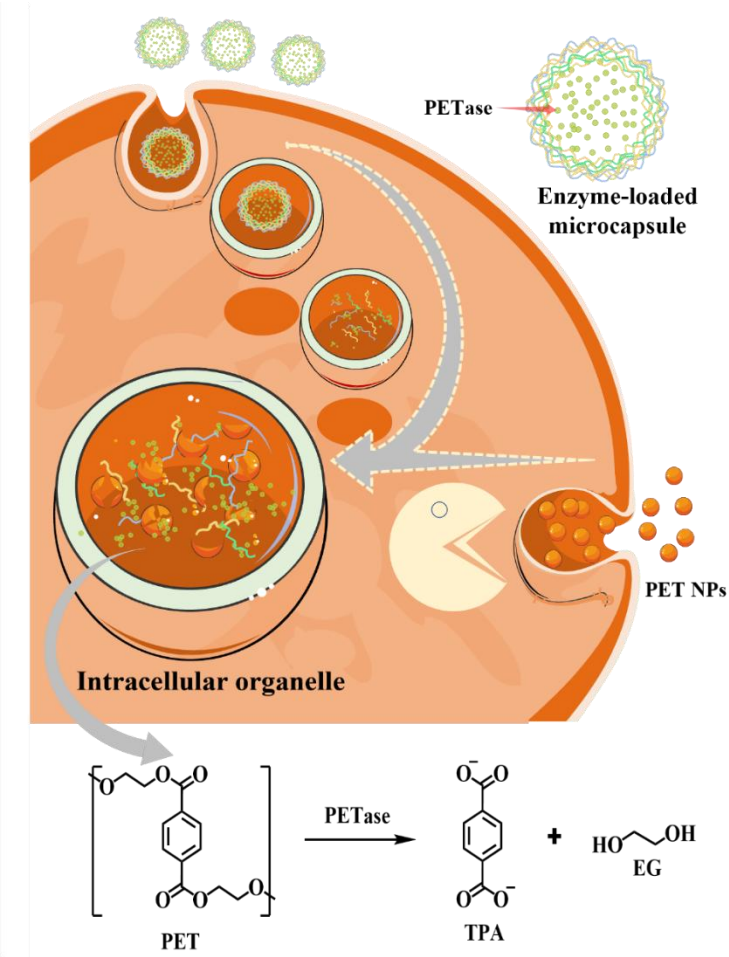

Figure 3.1. Engineered cells for the biodegradation of nanoplastics.

3.2 Experimental section

3.2.1 Regant and materials

Polyethylene terephthalate filament (PET, #ES30-FB-000110) was purchased from Goodfellow (Germany). Rhodamine B (RB, #83689), hexafluoroisopropanol (HFIP, #105228), bovine serum albumin (BSA, #A2153), branched poly(ethyleneimine) (PEI, $M_w \approx 25$ kDa, #408727), poly-L-arginine hydrochloride (pARG, $M_w \approx 15$-70 kDa, #P7762), dextran sulfate sodium salt (DEXS, $M_w \approx 10$ kDa, #51227), calcium chloride dihydrate ($CaCl_2 \cdot 2H_2O$, #223506), sodium carbonate (Na_2CO_3, #S7795), sodium phosphate dibasic (Na_2HPO_4, #S3264), potassium phosphate monobasic (KH_2PO_4, #P5655), ethylenediamine-tetra-acetic acid disodium salt dihydrate (EDTA disodium salt, #E5134) and iron(II) sulfate heptahydrate ($FeSO_4 \cdot 7H_2O$, #F7002) were purchased from Sigma-Aldrich (Germany). Trisodium citrate dihydrate (#3580.4), hydrochloric acid (HCl, #4625.1) and sodium hydroxide (NaOH, #6771.1) were purchased from Carl Roth (Germany). Hydrogen peroxide (H_2O_2, #23622) was purchased from Avantor (Germany). Ultrapure double distilled water (ddH_2O, MilliQ) with a resistivity greater than 18.2 MΩ cm^{-1} was used for all experiments.

3.2.2 Synthesis of polyethylene terephthalate nanoparticles (PET NPs)

Polyethylene terephthalate (PET) nanoparticles (PET NPs) were synthesized following a previously reported protocol [230], with modifications as described below. To prepare the PET precursor solution, 0.58 g of PET filament was accurately weighed and added to 35 mL of hexafluoroisopropanol (HFIP) in a glass container. The mixture was subjected to continuous stirring at room temperature (RT, ~25°C) for 1 hr to ensure complete dissolution of the PET polymer. For nanoprecipitation, 10 mL of the PET solution was introduced dropwise at a controlled rate of 1 mL/min into 75 mL of MilliQ water under continuous stirring at RT. A LEGATO® 111 syringe pump (KD Scientific, USA) equipped with a 10 mL glass syringe (FORTUNA Optima®, Poulten & Graf GmbH, Germany) was used to maintain a consistent flow rate, allowing for controlled nucleation and precipitation of PET NPs. Following precipitation, the resulting PET NP suspension was transferred into a round-bottom flask and subjected to mild heating at

55°C under vacuum using a rotary evaporator to facilitate the removal of residual HFIP. Once the total volume of the suspension was reduced to approximately 30 mL, an additional 75 mL of MilliQ water was introduced, and a second round of rotary evaporation was performed under identical conditions to further concentrate the nanoparticle dispersion and remove any remaining HFIP. To ensure complete removal of HFIP, the PET NP suspension was subjected to centrifugation at 3000 rpm for 5 min at RT. The supernatant was carefully discarded, and the nanoparticle pellet was resuspended in 5 mL of bovine serum albumin (BSA) solution (0.5 mg/mL, pH 8.2). This washing step was repeated three times, with the supernatant being discarded and replaced with fresh MilliQ water in each cycle. After the final wash, the PET NPs were resuspended in 5 mL of BSA solution (0.5 mg/mL, pH 8.2) and stored at 4°C in the dark until further use.

For the preparation of rhodamine B-labeled PET nanoparticles (PET-RB NPs), the same nanoprecipitation protocol was followed, with the exception that 1 mL of a rhodamine B (RB) solution (0.05 mg/mL) was added to the PET solution prior to the precipitation step. This modification allowed for the incorporation of fluorescent RB molecules into the PET NPs, facilitating subsequent imaging and tracking studies.

3.2.3 Synthesis of polyelectrolyte microparticles (caps)

Polyelectrolyte capsules were synthesized using a layer-by-layer (LbL) assembly method following previously established protocols [177, 231]. The process involved the fabrication of micrometer-sized calcium carbonate ($CaCO_3$) cores as sacrificial templates, followed by polymer coating and core removal to obtain hollow polyelectrolyte capsules.

Step 1: Fabrication of $CaCO_3$ Template Cores. To synthesize $CaCO_3$ cores, 615 µL of 0.33 M sodium carbonate (Na_2CO_3) solution was mixed with 400 µL of a 5 mg/mL molecular cargo solution (either PETase or BSA-FITC) in a 20 mL glass vial. The mixture was subjected to vigorous stirring at 900 rpm to ensure uniform dispersion. Subsequently, 615 µL of 0.33 M calcium chloride dihydrate ($CaCl_2 \cdot 2H_2O$) solution was introduced into the system under continuous stirring. The reaction mixture was maintained at room temperature (RT, ~25°C) under magnetic stirring for 30 s, followed by a 3 min static incubation period to allow for $CaCO_3$ precipitation and crystal growth cessation. The resulting $CaCO_3$ microparticles were collected via centrifugation at 3000 rpm for 30 s,

after which the supernatant was discarded. The precipitate was subjected to a three-step washing process with fresh MilliQ water to remove unreacted reagents. Each washing step consisted of centrifugation at 3000 rpm for 30 s, removal of the supernatant, and resuspension in fresh water.

Step 2: Layer-by-Layer Assembly of Polyelectrolyte Shells. The polyelectrolyte shell coating was achieved using sequential adsorption of oppositely charged polymers onto the $CaCO_3$ cores [232]. Initially, the $CaCO_3$ cores were resuspended in 1 mL of a negatively charged dextran sulfate (DEXS) solution (2 mg/mL in 0.1 M NaCl, pH 6.5) and subjected to 2 min of sonication to enhance polymer adsorption. The suspension was then incubated under continuous shaking for 10 min to ensure uniform polymer coating. Excess unbound polymer was removed through three cycles of centrifugation at 3000 rpm for 30 s, with each cycle followed by supernatant removal and resuspension in fresh MilliQ water. Subsequently, 1 mL of positively charged poly-L-arginine (pARG) solution (2 mg/mL in 0.1 M NaCl, pH 6.5) was added to the particle suspension. The mixture was processed following the same adsorption, washing, and resuspension steps as described for DEXS. This alternating deposition of DEXS and pARG was repeated to construct a four-bilayer shell [$(DEXS/pARG)_4$] [159].

Step 3: Removal of $CaCO_3$ Core and Capsule Purification. To obtain hollow polyelectrolyte capsules, the polymer-coated $CaCO_3$ particles were incubated overnight in 2 mL of 0.1 M ethylenediaminetetraacetic acid (EDTA), pH 6.5, at 4°C, allowing for complete dissolution of the $CaCO_3$ core. The resulting hollow polyelectrolyte capsules were then purified by centrifugation at 1800 rpm for 10 min, followed by removal of the supernatant and resuspension in fresh MilliQ water. This washing process was repeated three times to ensure the complete removal of residual EDTA. Finally, the purified capsules with a $(DEXS/pARG)_4$ shell architecture were resuspended in 1 mL of MilliQ water and stored at 4°C until further use.

Step 4: Alternative Capsule Architecture with Proton-Buffering Capability. To introduce proton-buffering functionality, an alternative capsule configuration was synthesized by modifying the final two bilayers. Specifically, instead of forming the last two bilayers with pARG, positively charged polyethyleneimine (PEI, 2 mg/mL in 0.1 M NaCl, pH 6.5) was employed. This resulted in a final shell composition of $(DEXS/pARG)_2/(DEXS/PEI)_2$, which provided enhanced buffering capacity within the capsule microenvironment.

Regardless of the final shell composition, the molecular cargo (PETase or BSA-FITC) remained encapsulated within the hollow capsule cavity after $CaCO_3$ dissolution, ensuring its retention for subsequent applications.

3.2.4 Estimation of the amount of PETase per capsule

According to the methodology outlined in §3.2.3, the encapsulation of PETase was initiated by utilizing 400 μL of a PETase solution at a concentration of 5 mg/mL as the template for core synthesis. This corresponds to a total PETase mass of 0.4 mL × 5 mg/mL = 2 mg of PETase. Following the core dissolution process and subsequent encapsulation, the resulting capsules were dispersed in 1 mL of ultrapure water, yielding a theoretical PETase concentration of 2 mg/mL in the final suspension. It is important to note that this value represents the theoretical upper limit of PETase concentration, as it does not account for potential losses incurred during inefficient integration of PETase into the core structures or during the washing steps, which may result in partial enzyme degradation or removal. The concentration of capsules in the stock solution was quantified to be approximately 10^8 capsules per milliliter (mL^{-1}). Based on this measurement, the upper limit for the amount of PETase per individual capsule can be estimated as follows: 2 mg/mL (total PETase concentration) divided by 10^8 capsules/mL (capsule concentration) equals 2×10^{-8} mg of PETase per capsule, which is equivalent to 20 pg of PETase per capsule. This calculation assumes ideal conditions with no loss of PETase during the encapsulation and washing processes, thereby providing a conservative estimate of the maximum possible enzyme loading per capsule.

3.2.5 Characterization of nano- and microparticles

Morphology characterization: The morphology of the PET NPs was determined with a transmission electron microscope (TEM, JEM 1011, JEOL) on dried samples. The capsules were imaged with optical bright-field microscopy and fluorescence microscopy

(LSM880 system, Zeiss; the continuous wave laser was generated by a two-photon generator (Ti:Sa Laser Mai Tai, Spectra Physics)).

Dynamic light scattering: Dynamic light scattering (DLS) analysis for obtaining the hydrodynamic diameter d_h of the particles in MilliQ water was conducted using a Malvern Zetasizer Particle Analyzer (ZEN3600, Malvern).

Fourier transformed infrared (FTIR) characterization: Fourier-transform infrared spectra (FTIR) were collected using an FTIR spectrometer (Cary 630, Agilent).

Characterization of optical properties: Fluorescence excitation and fluorescence emission spectra were collected in MilliQ water using a Fluorescence Spectrometer (Cary Eclipse, Agilent)

Stability of properties in different media: The stability of the hydrodynamic diameter and the stability of RB fluorescence of the PET-RB NPs was probed by incubating the NPs in phosphate buffered saline (PBS), pH 7.4 or RPMI-1640 culture medium supplemented with 10% FBS and 1% P/S (see the cell culture part for details) for 120 h at 25 ℃, whilre monitoring the hydrodynamic diamter and fluroescence intensity over time.

3.2.6 Degradation of PET by PETase

The enzymatic degradation of polyethylene terephthalate nanoparticles (PET NPs) was analyzed by monitoring the formation of 2-hydroxyterephthalate (HOTP), a fluorescent byproduct generated in situ via the Fenton reaction following the radical hydroxylation of terephthalic acid (TPA), as described in previous studies [233, 234]. The fluorescence of HOTP was measured at an excitation wavelength of 328 nm and an emission wavelength of 421 nm.

Enzymatic Hydrolysis Procedure. A reaction mixture was prepared by adding 50 µL of PET NP dispersion (C_NP = 7 mg/mL) as the enzymatic substrate into a 1.5 mL microcentrifuge tube containing 1 mL of phosphate buffer (PB, Na_2HPO_4-KH_2PO_4, 1/15 M, pH 8). Subsequently, 25 µL of PETase solution (2 mg/mL) was introduced into the mixture. The reaction was incubated at room temperature (RT) for 48 h under continuous agitation (200 rpm) using an orbital shaker (KS 250B, IKA, Germany) to ensure homogeneous enzymatic activity. During enzymatic hydrolysis, PET NPs were degraded

into terephthalic acid (TPA) and ethylene glycol (EG), as illustrated in Figure 3.2. After incubation, the reaction mixture was centrifuged at 3000 rpm for 5 min to precipitate any undigested PET NPs, and the supernatant containing the released TPA was carefully collected for subsequent analysis.

Fluorescence-Based HOTP Detection. For fluorescence quantification of enzymatic degradation, 30 µL of the collected supernatant was transferred into each well of a 96-well black microtiter plate. To initiate the Fenton reaction, the following reagents were sequentially added per well, reaching a total reaction volume of 200 µL: 100 µL of phosphate buffer (PB, 1/15 M, pH 8), 30 µL of H_2O_2 (2% v/v) solution, 20 µL of EDTA (3 mM) solution and 20 µL of $FeSO_4 \cdot 7H_2O$ (3 mM) solution. The plate was incubated at room temperature for 25 min to allow the hydroxylation of TPA and the subsequent formation of HOTP, as depicted in Figure 3.2. To quench the reaction, 50 µL of 2 M H_2SO_4 solution was added to each well, stabilizing the fluorescence signal for analysis.

Fluorescence Measurement. The fluorescence intensity of HOTP was measured using a FLUOstar Omega microplate reader (BMG LABTECH, Germany), equipped with a 460 nm emission filter. Data acquisition and analysis were performed using the Omega 4.01 R2 software. The fluorescence intensity of HOTP directly correlated with the concentration of enzymatically released TPA, thereby providing a quantitative measure of PET NP degradation.

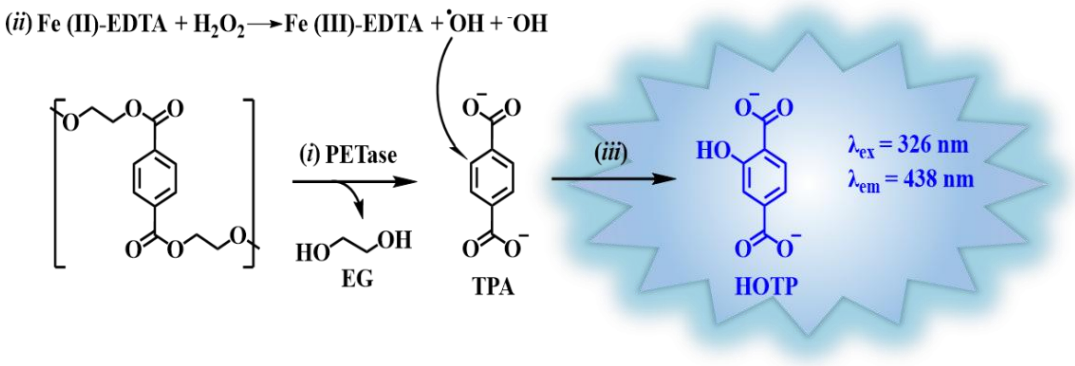

Figure 3.2. Fluorimetric detection of PET NPs via TPA. (i) Enzymatic PET hydrolysis yields TPA and EG. (ii) Fe(II)-EDTA generates hydroxyl radicals (·OH). (iii) ·OH hydroxylates TPA to fluorescent 2-HOTP (λ_{ex} = 326 nm, λ_{em} = 438 nm).

To evaluate the influence of pH on the enzymatic degradation of PET nanoparticles (PET NPs) by PETase, the previously described enzymatic hydrolysis assay was systematically repeated across a range of pH conditions. Specifically, 50 µL of PET NP dispersion (7 mg/mL) and 25 µL of PETase solution (2 mg/mL) were mixed with 1 mL of phosphate buffer (PB) solution at varying pH values. The enzymatic reaction and subsequent fluorescence-based analysis were conducted as detailed in the prior experimental procedure.

Preparation of Phosphate Buffer (PB) Solutions at Different pH Values. The PB solutions were prepared by mixing two stock solutions, Na_2HPO_4 (1/15 M) and KH_2PO_4 (1/15 M), in defined volume ratios to achieve the desired pH conditions. The buffer compositions were adjusted as follows:

pH ≈ 4.0: 0:10 ratio (only KH_2PO_4) – Since the intrinsic pH of KH_2PO_4 (1/15 M) was 4.5, hydrochloric acid (HCl) was added to adjust the final pH to 4.0.

pH ≈ 5.0 (measured pH = 4.92): 0.1:9.9 ratio of Na_2HPO_4:KH_2PO_4.

pH ≈ 6.0 (measured pH = 5.91): 1.0:9.0 ratio of Na_2HPO_4:KH_2PO_4.

pH ≈ 7.0 (measured pH = 6.98): 6.0:4.0 ratio of Na_2HPO_4:KH_2PO_4.

pH ≈ 8.0 (measured pH = 8.00): 9.5:0.5 ratio of Na_2HPO_4:KH_2PO_4.

Each buffer solution was carefully prepared and pH measurements were performed using a calibrated pH meter to ensure precision. The adjusted pH conditions were maintained throughout the enzymatic degradation assay to assess the influence of pH variation on PETase activity.

3.2.7 Degradation of PET by encapsulated PETase

To evaluate the enzymatic activity of encapsulated PETase, the hydrolysis assay described in §3.2.5 was also conducted for PETase encapsulated within polyelectrolyte capsules of two distinct shell geometries: $(DEXS/pARG)_4$ and $(DEXS/pARG)_2/(DEXS/PEI)_2$.

Since the encapsulation confines the enzyme within the capsule matrix, it was necessary to disrupt the capsules to allow access of the PET NPs to the encapsulated

PETase prior to initiating the enzymatic reaction. To achieve this, the capsules were subjected to ultrasonic treatment using a SONOREX DIGITEC DT 102H ultrasonic bath (Bandelin, Germany), operating at a fixed frequency of 35 kHz with an adjustable power range of 120–480 W. The sonication was performed in a cold water bath for 10 min, facilitating capsule rupture and the subsequent release of PETase into the reaction medium.

This approach ensured the efficient liberation of PETase while minimizing potential enzyme denaturation, thereby enabling a direct comparison of free versus encapsulated PETase in PET degradation assays.

3.2.8 Cell culture techniques

Human cervical carcinoma cells (HeLa cells) were cultured in Dulbecco's Modified Eagles Medium (DMEM, #11965092, ThermoFisher Scientific) with 4.5 g/L glucose supplemented with 10% fetal bovine serum (FBS, Biochrom, Germany, #S0615), 1% penicillin/streptomycin (P/S, #15070063, Thermo Fisher Scientific) at 5% CO_2 and 37 °C. For cell viability assays (§3.2.9) and enzymatic degradation experiments (§3.2.6, §3.2.7), HeLa cells were cultured in the aforementioned serum-supplemented medium. However, for colocalization studies (§3.2.10), a serum-free DMEM formulation was used during the incubation with LysoTracker, to prevent potential interference from serum components.

3.2.9 Cell viability assays

The cytotoxicity of rhodamine B-labeled PET nanoparticles (PET-RB NPs) and PETase-loaded polyelectrolyte capsules (PETase@caps) with $(DEXS/pARG)_2/(DEXS/PEI)_2$ shell geometry was evaluated based on cellular metabolic activity, quantified using a resazurin reduction assay [234].

HeLa cells were seeded into black 96-well plates (Corning® 3603, USA) with a seeding area of 0.32 cm^2 per well at an initial density of 5,000 cells per well in 100 µL of

complete culture medium. Cells were incubated at 37°C in a humidified environment with 5% CO_2 for 24 h. Following overnight incubation, the culture medium was carefully aspirated and replaced with fresh medium containing either: PET-RB NPs at a designated nanoparticle concentration (C_{NP}), or PETase@caps, added at a defined capsule-to-cell ratio ($N_{caps/cell}$). Control wells consisted of cells maintained under identical conditions but without exposure to PET-RB NPs or PETase@caps. After 24 h or 48 h of exposure, the treated cells were carefully washed three times with PBS to remove residual nanoparticles or capsules. Subsequently, 200 µL of sterile-filtered resazurin solution (25 µg/mL in DMEM) was added to each well, and the plate was incubated for 3 h at 37°C and 5% CO_2 to allow enzymatic reduction of resazurin to resorufin by metabolically active cells. Following incubation, the fluorescence intensity of resorufin was measured using a FLUOstar Omega microplate reader (BMG LABTECH, Germany), with excitation at λ_{ex} = 544 nm, emission at λ_{em} = 590 nm, and a cut-off filter set at 570 nm. Data acquisition and analysis were conducted using Omega 4.01 R2 software. Cell viability (V) was determined by normalizing the fluorescence intensity of PET-RB NP- or PETase@caps-exposed cells to that of the untreated control cells, according to the following equation:

$$V = \frac{F_{treated}}{F_{control}} \times 100\%$$

where $F_{treated}$ represents the fluorescence intensity of cells exposed to PET-RB NPs or PETase@caps, and $F_{control}$ corresponds to the fluorescence intensity of control cells not exposed to either material.

3.2.10 Colocalization experiments

For colocalization imaging, a total of 100,000 HeLa cells were seeded in a µ-Dish (#81156, ibidi; bottom area: 3.5 cm^2) containing 2 mL of Dulbecco's Modified Eagle Medium (DMEM) supplemented with 10% fetal bovine serum (FBS). The cells were maintained overnight in a humidified incubator at 37 °C with 5% CO_2 to allow for adherence and stabilization. Following this, the cells were incubated with polyethylene terephthalate-rhodamine B nanoparticles (PET-RB NPs) at a concentration of CNP = 5 µg/mL for an additional 24-h period under the same incubation conditions. On the third day, the cells were further incubated with bovine serum albumin-fluorescein

isothiocyanate-labeled capsules (BSA-FITC@caps) at a concentration of Ncaps/cell = 1.5 capsules per initially seeded cell, again for 24 h. On the fourth day, after the 24-h incubation period with BSA-FITC@caps, the lysosomes within the cells were optionally stained. For lysosomal staining, the cells were washed three times with phosphate-buffered saline (PBS) to remove any residual medium and then incubated with 1 mL of serum-free medium containing 50 nM LysoTracker™ Deep Red staining solution for 30 min at 37 °C and 5% CO_2. This serum-free incubation step was the only instance where serum-free conditions were applied. Following the staining procedure, the cells were washed three times with PBS to remove excess dye, and 2 mL of fresh culture medium supplemented with 10% FBS was added to the dish. In cases where lysosomal staining was not performed, the medium was directly replaced with 2 mL of fresh culture medium supplemented with 10% FBS.

Subsequently, the cells were imaged using an upright confocal laser scanning microscope (LSM880 system, Zeiss). Image acquisition was performed using the ZEN 2.3 software (blue edition, operation software for LSM880). The following fluorescence settings were employed: for BSA-FITC@caps, excitation wavelength (λex) = 488 nm and emission wavelength (λem) = 517 nm; for PET-RB NPs, λex = 561 nm and λem = 577 nm; and for LysoTracker™ Deep Red, λex = 633 nm and λem = 688 nm. These settings were optimized to ensure minimal spectral overlap and maximum signal specificity for each fluorescent marker.

3.2.11 Intracellular degradation (multiple cells)

HeLa cells were seeded in black 96-well plates (Corning® 3603, USA; 0.32 cm^2 seeding area per well) at an initial density of 5,000 cells per well. The cells were cultured in 100 µL of Dulbecco's Modified Eagle Medium (DMEM) supplemented with 10% fetal bovine serum (FBS) and maintained in a humidified incubator at 37 °C under 5% CO_2 for 48 h to ensure proper cell adherence and proliferation. Following this incubation period, polyethylene terephthalate-rhodamine B nanoparticles (PET-RB NPs) were introduced into each well at a final concentration of C_{NP} = 5 µg/mL, and the cells were further incubated overnight under the same conditions to allow for nanoparticle internalization.

On the third day, non-internalized PET-RB NPs were removed by carefully aspirating the medium from each well. The cells were then replenished with fresh serum-supplemented medium containing PETase-loaded capsules (PETase@caps) at a density of 1.5 capsules per initially seeded cell. Based on the upper estimated limit of PETase loading per capsule, as described in §3.2.6, each capsule contained a maximum of 12.5 pg of PETase. After an incubation period of time t, the cells were washed three times with phosphate-buffered saline (PBS) to remove any residual extracellular components.

The rhodamine B (RB) fluorescence intensity (I_{RB}) in each well was quantified using a microplate reader (BMG LABTECH, Germany) with excitation and emission wavelengths set to λ_{ex} = 544 nm and λ_{em} = 590 nm, respectively, and a 10 nm bandpass filter to ensure precise fluorescence detection. As a control, an identical experimental procedure was conducted in parallel, omitting the addition of PETase@caps to account for any background fluorescence or nonspecific effects. This control experiment was essential to validate the specificity of the observed fluorescence changes attributable to PETase activity.

3.2.12 Intracellular degradation (single cells)

The degradation of polyethylene terephthalate-rhodamine B nanoparticles (PET-RB NPs) in the presence of PETase-loaded capsules (PETase@caps) was monitored at the single-cell level using fluorescence microscopy. Control experiments were conducted by incubating cells with PET-RB NPs alone and PETase@caps alone to rule out nonspecific effects.

For an experiment, 100,000 HeLa cells were seeded in 2 mL of Dulbecco's Modified Eagle Medium (DMEM) supplemented with 10% fetal bovine serum (FBS) in a grid-500 µ-Dish (#80156, ibidi; seeding area: 3.5 cm²). The cells were cultured overnight in an incubator at 37 °C under 5% CO_2. On the following day, the cells were incubated with PET-RB NPs at a concentration of CNP = 5 µg/mL under the same incubation conditions (37 °C, 5% CO_2) for 24 h. On the third day, non-internalized PET-RB NPs were removed by careful aspiration, and the cells were incubated with 2 mL of fresh medium containing PETase@caps, which featured a shell geometry of $(DEXS/pARG)_2/(DEXS/PEI)_2$, at a density of 1.5 capsules per initially seeded cell. The

cells were maintained in culture for a specified incubation time t (ranging from 2 to 48 h) at 37 °C and 5% CO_2. After incubation, the cells were washed three times with phosphate-buffered saline (PBS) to remove extracellular residues, and 2 mL of fresh culture medium supplemented with 10% FBS was added. The cells were then imaged using an upright confocal laser scanning microscope (LSM880 system, Zeiss). Imaging was performed at five distinct time points (t = 2 h, 6 h, 12 h, 24 h, and 48 h) to assess the temporal dynamics of PET-RB NP degradation. During imaging, the temperature was maintained at 37 °C using a stage-top incubator, although CO_2 control was not implemented. The following imaging parameters were employed: bright-field microscopy and PET-RB NP fluorescence detection with excitation and emission wavelengths set to λ_{ex} = 561 nm and λ_{em} = 577 nm, respectively. Image acquisition and analysis were conducted using ZEN 2.3 software (blue edition, operation software for LSM880).

3.3 Result and discussion

3.3.1 Characterization of PET NPs

In this study, we employed poly(ethylene terephthalate) hydrolase (PETase) [217, 235], an enzyme recognized for its capability to catalyze the degradation of polyethylene terephthalate (PET) nanoparticles (NPs). Notably, enzymes capable of hydrolyzing other types of nanoplastic materials have also been identified and characterized in the literature [236]. The PETase enzyme and PET NPs utilized in this work were synthesized following established protocols [230, 237]. To facilitate visualization and tracking, PET NPs incorporating rhodamine B (referred to as PET-RB NPs) were also synthesized. These fluorescently labeled NPs exhibited an average diameter of dc = 138 ± 19 nm, as confirmed by dynamic light scattering (DLS) in Figure 3.3c. A representative TEM image of PET NPs is shown in Figure 3.3a. From a series of such images of the respective distribution of the core diameter, the mean PET NP diameter was determined to be dc ≈ 92 nm in Figure 3.3b. Fluorescence excitation and fluorescence emission spectra of RB and PET-RB NPs were collected in MilliQ water using a Fluorescence Spectrometer in Figure 3.3d. The prominent pink of fluorescence excitation and fluorescence emission spectra were similar between RB and PET-RB NPs. Thus, the labeling of fluorescent dye RB on PET NPs was achieved. The FTIR profiles of PET and PET-RB NPs were compared in Figure 3.3e and Figure 3.3f. The F-IR profiles of both types of NPs showed the characteristic absorption bands of PET bulk polymer at 1715 cm^{-1} (C=O stretching), 1578 cm^{-1} (stretching of C=C in ring), 1505 cm^{-1} (in-plane bending of C–H in ring; stretching of C=C in ring), and 1240 cm^{-1} (C=O in-plane bending, C–C stretching, C(=O)–O stretching) [230]. Thus, the integration rhodamine kept the PET chemistry intact.

The stability of both PET NPs and PET-RB NPs was rigorously characterized. Specifically, their fluorescence properties and colloidal stability were evaluated in solutions containing salts and proteins to mimic physiological and environmental conditions [238, 239]. Data indicate stability of both properties (d_h, I) in the 2 different media. The results demonstrated that both the fluorescence intensity and colloidal stability of the NPs remained consistent over time, with no significant aggregation or degradation observed (Figure 3.4). These findings underscore the suitability of PET-RB

NPs as a model system for studying nanoplastic degradation in biologically relevant environments.

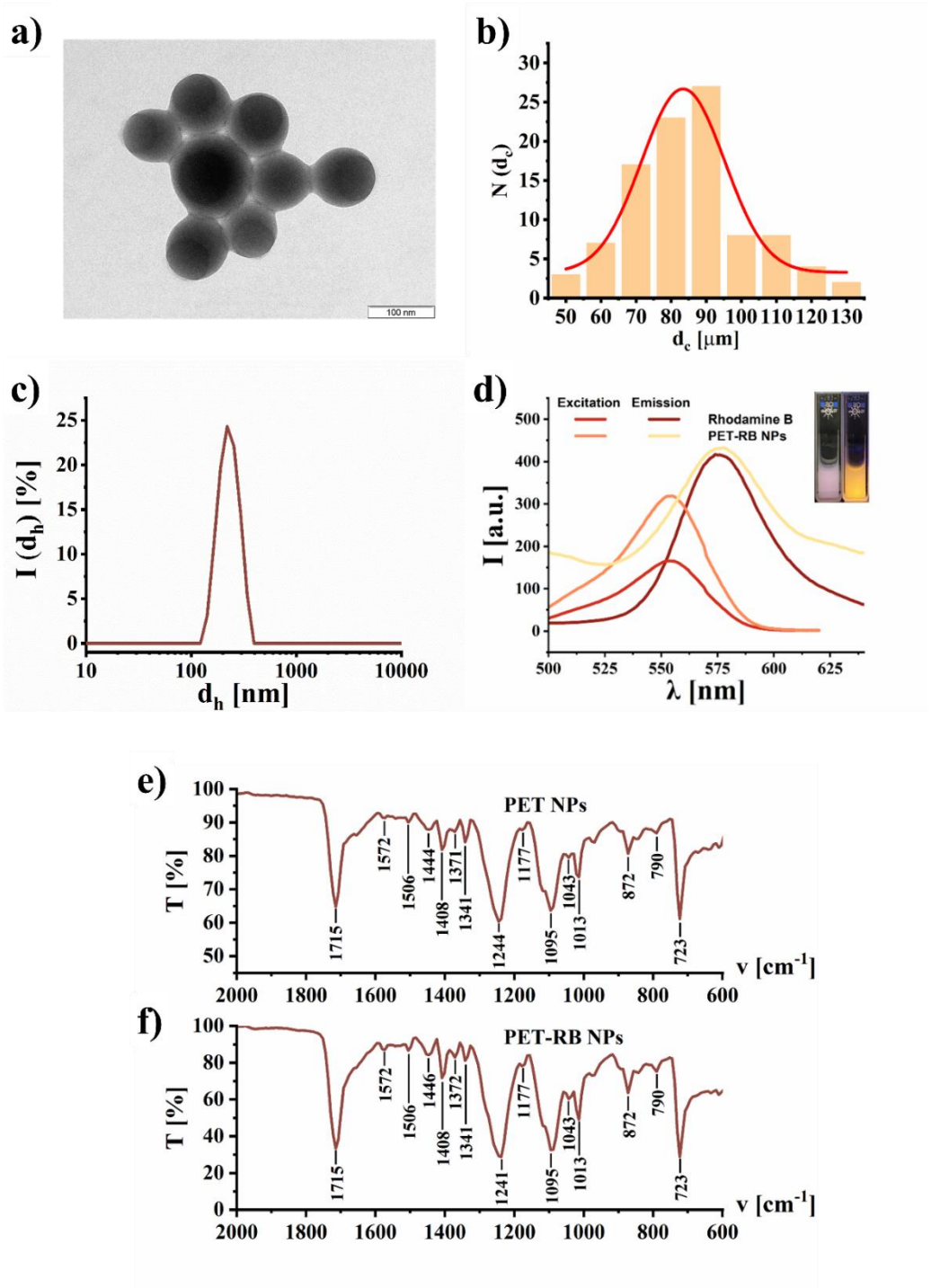

Figure 3.3. Characterization of PET NPs and PET-RB NPs: a) TEM image of PET NPs (scale bar: 100 nm). b) Size distribution N(d_c) of PET NPs, showing a mean diameter $d_c \approx$ 92.33 nm. c) Intensity-weighted hydrodynamic diameter distribution of PET-RB NPs

(average of five DLS measurements). d) Excitation and emission spectra of PET-RB and PET NPs in aqueous solution; inset displays photographs under visible (left) and UV light (right). FTIR spectra of (e) PET NPs and (f) PET-RB NPs, depicting transmission (T) vs. wavenumber (ν).

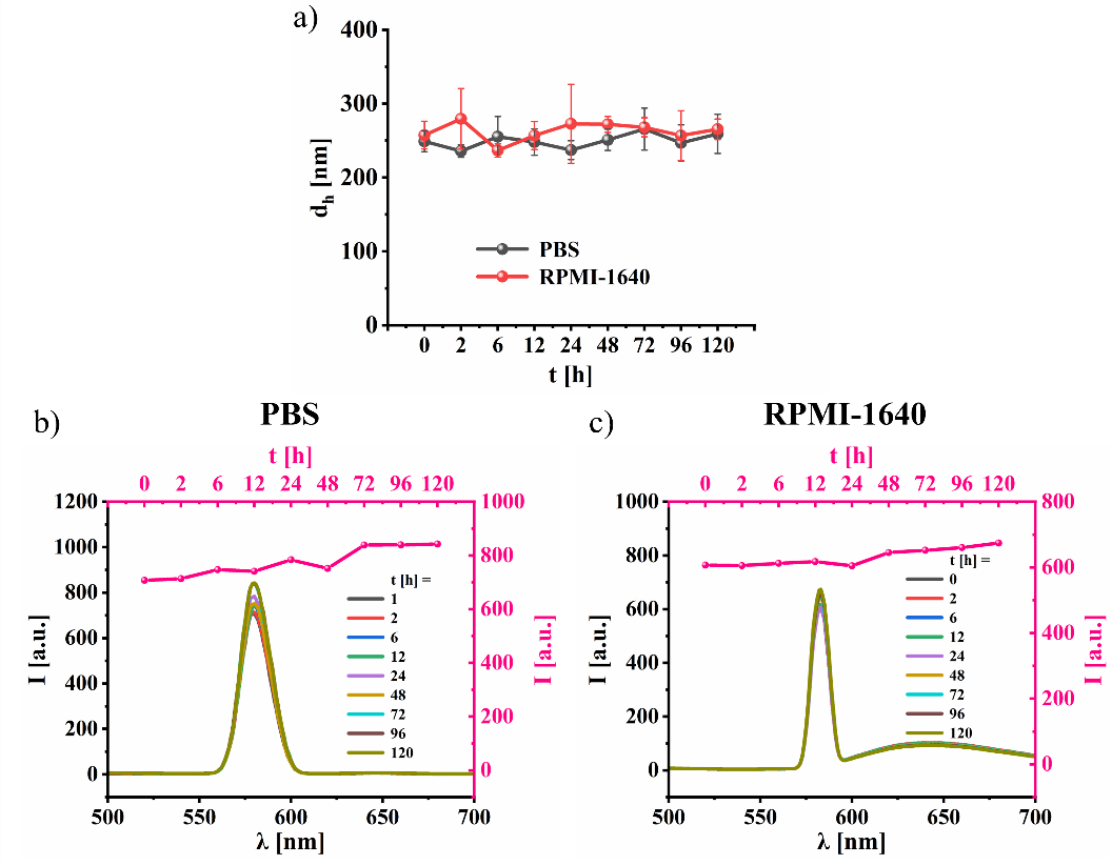

Figure 3.4. Time-dependent stability of PET-RB NPs incubated in PBS (pH 7.4) or RPMI-1640 (+10% FBS, 1% P/S): a) Hydrodynamic diameter (d_h, DLS intensity-weighted) vs. incubation time (t). b, c) Fluorescence spectra (I(λ), black axes) at different t and corresponding intensity (I(t)) over time.

3.3.2 Characterization of capsules

Polyelectrolyte capsules were then synthesized by layer-by-layer (lbl) assembly of oppositely charged polymers around the template cores with a schematic representation provided in Figure 3.5. As shown in Figure 3.6a, the built-up of layers was monitored by

zeta potential measurements, indicating the formation of each new layer by a reversal in the sign of the potential. BSA-FITC@caps ($(DEXS/pARG)_2/(DEXS/PEI)_2$ shell geometry) exhibited an average diameter of dc 2925 ± 210.70 nm, as confirmed by dynamic light scattering (DLS) in Figure 3.6b. The capsules were imaged with optical bright-field microscopy in Figure 3.6c and fluorescence microscopy (LSM880 system, Zeiss; the continuous wave laser was generated by a two-photon generator (Ti:Sa Laser Mai Tai, Spectra Physics)). In Figure 3.6c images of BSA-FITC encapsulated with (DEXS/pARG)2/(DEXS/PEI)2 (i.e. BSA-FITC@caps) is shown. From the images of the bright-field channel the mean capusule diameter was determined to be dc ≈ 3.3 µm in Figure 3.6d.

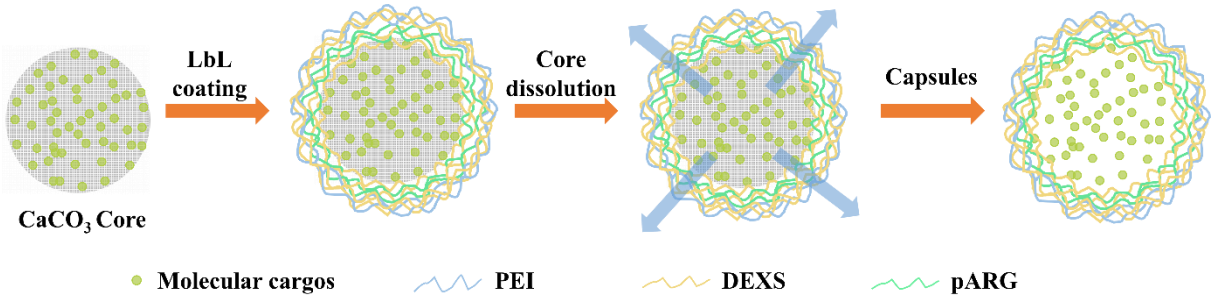

Figure 3.5. Schematic illustration of the synthesis of a multilayer polyelectrolyte capsule. The molecular cargo is either BSA-FITC or PETase. The final shell geometry of the here depicted capsule is $(DEXS/pARG)_2/(DEXS/PEI)_2$.

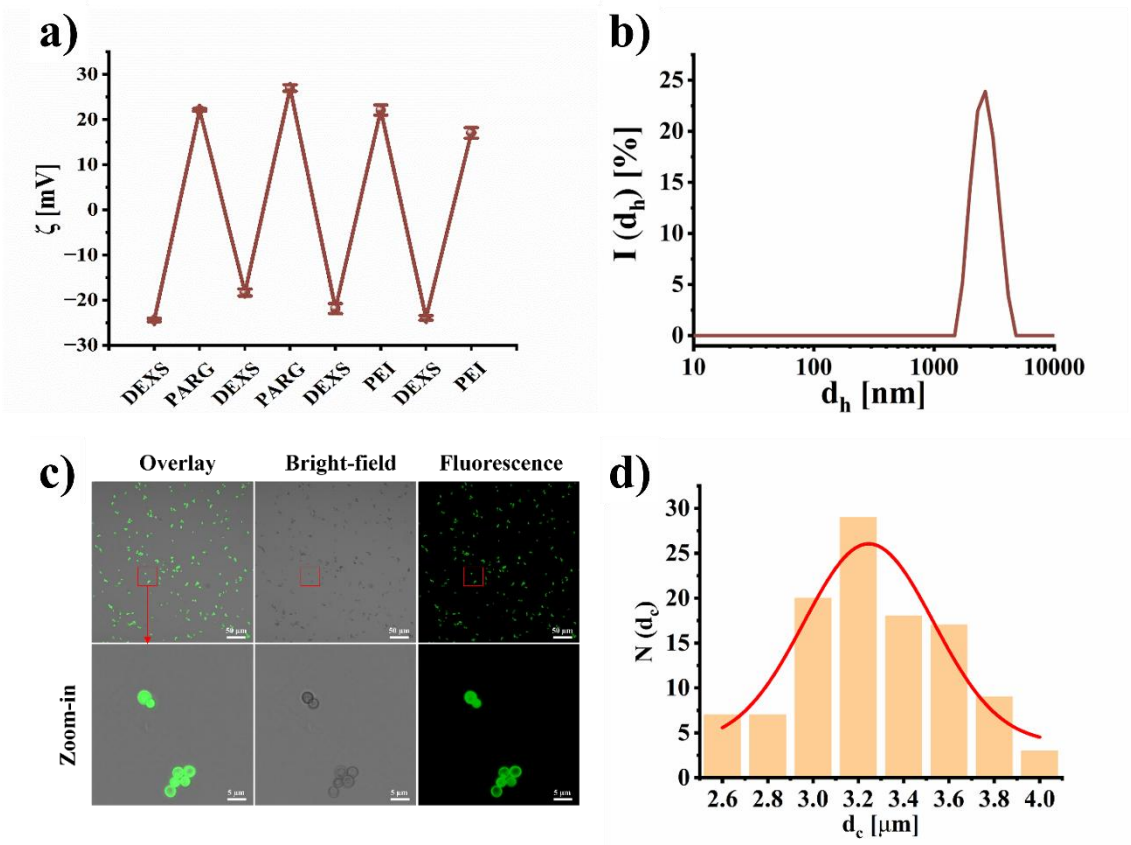

Figure 3.6. Characterization of polyelectrolyte-coated $CaCO_3$ capsules: a) Zeta potential (ζ) evolution during layer-by-layer assembly of $(DEXS/pARG)_2/(DEXS/PEI)_2$ in MilliQ water. b) Bright-field and FITC-fluorescence microscopy of BSA-FITC@caps (scale bars: 50 µm upper row, 5 µm zoom-in). c) Size distribution $N(d_e)$ showing mean capsule diameter $d_e \approx 3.3$ µm. d) Intensity-weighted hydrodynamic diameter distribution (average of 5 DLS measurements).

3.3.3 Degradation of PET by PETase

Degradation of PET by PETase was monitored by the presence of fluorescent 2-hydroxyterephthalate (HOTP), which is formed by the Fenton reaction between the hydrolysis product of PET (terephthalic acid (TPA) and $FeSO_4$ + H_2O_2. As shown in Figure 3.7, the fluorescence of HOTP was analyzed on a FLUOstar Omega microplate reader. The excitation and emission maxima of HOTP are 326 nm and 438 nm, respectively. The assay was performed for PET NPs and PET-RB NPs in the presence of PETase and as control without PETase. The results of the fluorescence read-out are

presented in Figure 3.8. The show, that after 12 h there is a saturation in the HOTP fluorescence, i.e. no further degradation of PET. Without PETase there is on production of HOTP. PETase however operates best under neutral or slightly alkaline conditions, whereas there is only insufficient hydrolysis of PET at low pH (pH = 4). Results are shown in Figure 3.9 and indicate that at pH = 4 there is basically no enzymatic activity.

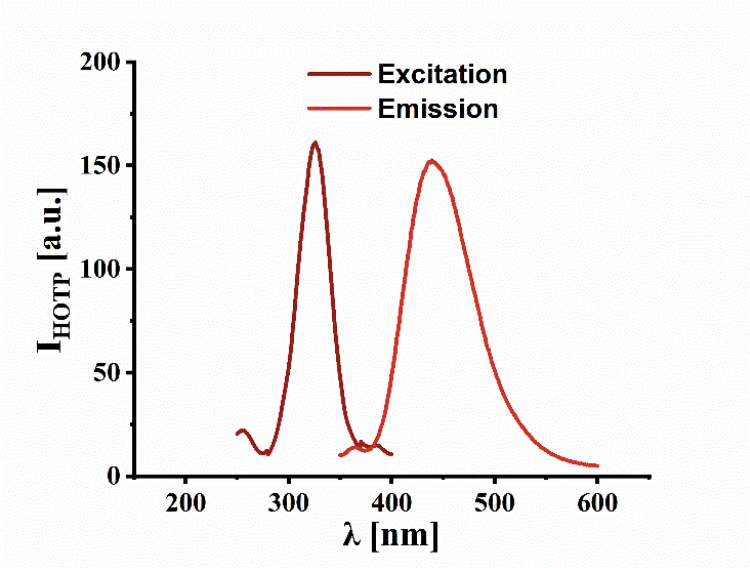

Figure 3.7. Excitation and emission spectra of HOTP.

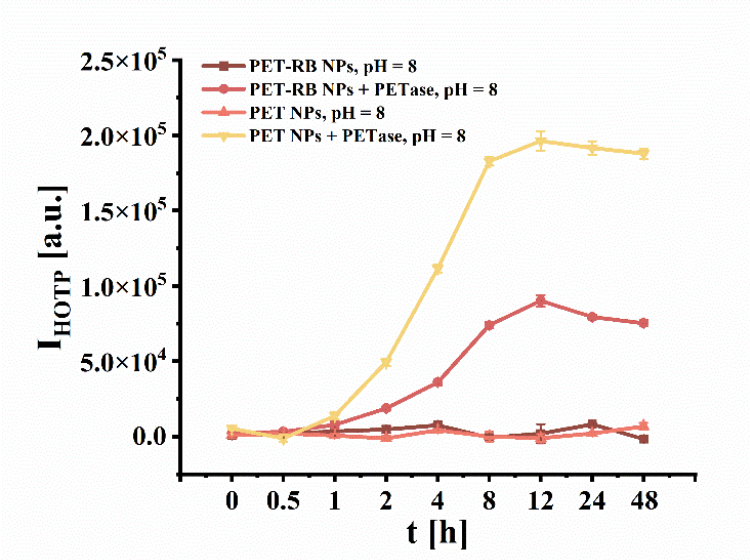

Figure 3.8. HOTP fluorescence intensity I_{HOTP} of PET-RB NPs and PET NPs with/without PETase at pH 8.

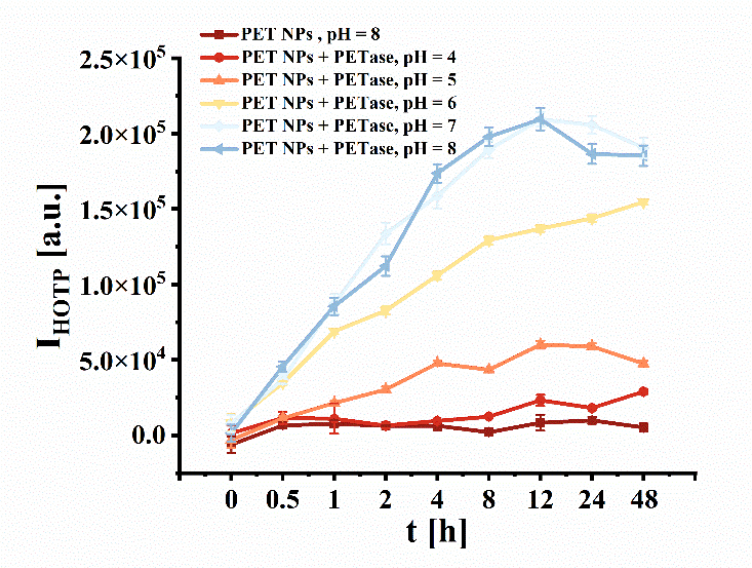

Figure 3.9. pH-dependent fluorescence intensity I_{HOTP} of PET NPs with/without PETase treatment.

3.3.4 Degradation of PET by encapsulated PETase

Previous studies have demonstrated negligible PETase activity at pH 4, precluding its functionality within acidic endosomal/lysosomal compartments. To construct engineered cells capable of intracellular nanoplastic degradation, two critical requirements must be met: (1) sufficient PETase delivery into lysosomes, and (2) preservation of enzymatic activity under acidic conditions. Polyelectrolyte capsules address these challenges through their high loading capacity and the proton-buffering effect of incorporated polyethylenimine (PEI), enabling both efficient cellular uptake and maintenance of PETase activity in lysosomal environments [52, 240, 241].

PETase was initially encapsulated within pH-responsive microcapsules featuring a degradable $(DEXS/pARG)_4$ shell geometry. To verify post-encapsulation activity, capsules were disrupted via sonication and incubated with PET nanoparticles (NPs), with degradation monitored over 48 h (Figure 3.10a). While encapsulated PETase retained significant activity at pH 8, no degradation was observed at pH 4, consistent with the enzyme's pH-dependent activity profile. To overcome lysosomal pH inhibition, a proton-buffering system was engineered into the capsule shell by replacing two pARG layers with branched polyethylenimine (PEI, $M_w \approx 25$ kDa), yielding a

$(DEXS/pARG)_2/(DEXS/PEI)_2$ shell geometry (Figure 3.10b). Remarkably, the released PETase achieved measurable nanoplastic degradation even at pH 4, attributable to PEI-mediated local pH modulation that maintains enzymatic activity. This breakthrough demonstrates the feasibility of creating engineered cells for intracellular plastic degradation, where "@caps" denotes PEI-incorporated shell systems.

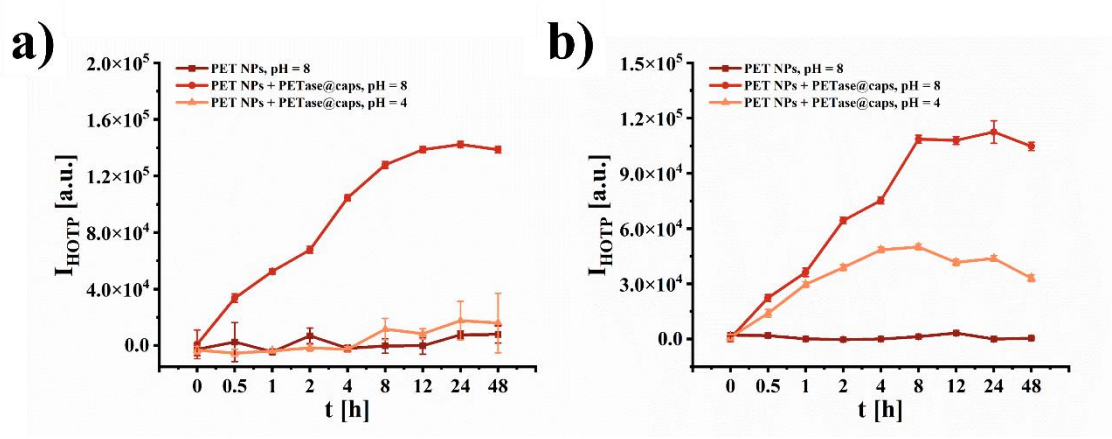

Figure 3.10. Enzymatic degradation assay of PET NPs: a) With ultrasonically disrupted $(DEXS/pARG)_4$ PETase@caps in PB (pH 8 or 4). b) With ultrasonically disrupted $(DEXS/pARG)_2/(DEXS/PEI)_2$ PETase@caps in PB (pH 8 or 4).

3.3.5 Cell viability assays

Prior to the examination of plastic degradation within cellular contexts, it is imperative to ascertain the non-toxic nature of the material under investigation. Results are shown in Figure 3.11. In the investigated concentration range, there was no reduction in cell viability upon the presence of PET-RB NPs. However, at high capsule exposure concentrations (which are higher than used for the following experiments) a reduction in cell viability was found [242].

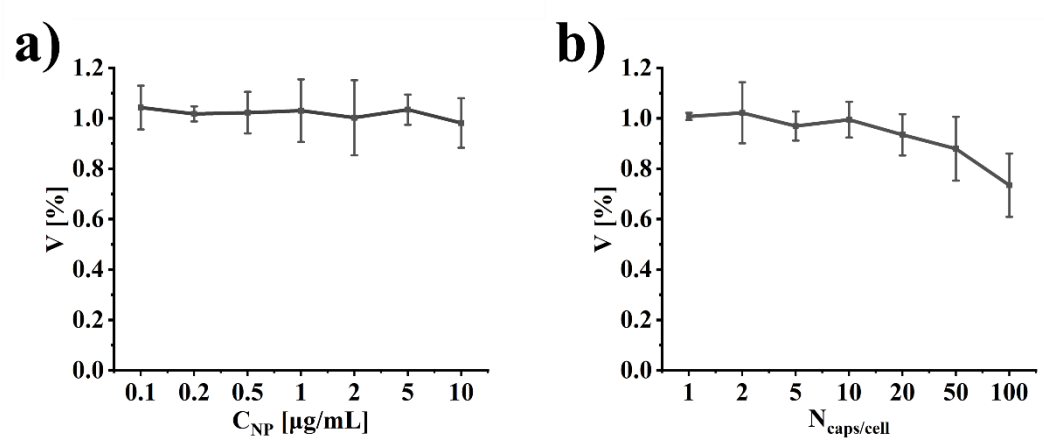

Figure 3.11. Concentration-dependent cytotoxicity assessment: a) Cell viability (V) versus PET-RB NP concentration (C_{NP}) after 24 h exposure (mean ± SD, n=5). b) Cell viability (V) versus capsule number per cell (N_{caps}) after 48 h exposure (mean ± SD, n=5).

3.3.6 Colocalization experiments

The successful construction of engineered cells capable of intracellular PET degradation requires two critical conditions: (1) efficient endocytic uptake of PETase@caps, and (2) subsequent colocalization of the released enzymes with PET NPs within lysosomal compartments. the essential colocalization of PETase with PET NPs for enzymatic degradation, we employed BSA-FITC@caps as a fluorescent protein tracer due to PETase's non-fluorescence. Our experimental design involved sequential 24 h co-incubation of cells with PET-RB NPs and BSA-FITC@caps. Fluorescence imaging revealed spatial colocalization between BSA-FITC@caps (shown in green false colors) and PET-RB NPs (shown in blue false colors) in cells (Figure 3.12).

For precise lysosomal localization analysis, we performed 30-minute LysoTracker staining following particle internalization. As demonstrated in Figure 3.13, the absence of spectral crosstalk between the green (protein), blue (nanoplastics), and red (lysosome) channels validated signal specificity. Notably, while acid-triggered release of BSA-FITC from capsules occurred within lysosomes, cytoplasmic dispersion was also observed. Partial triple-fluorescence overlap (Figure 3.14) indicated that: 1） BSA-FITC@caps colocalized with lysosomal markers; 2) PET-RB NPs accumulated in lysosomes; 3) Released BSA-FITC showed association with internalized PET-RB NPs.

Interestingly, cytoplasmic BSA-FITC distribution (observed in all six examined cells) suggests potential PET degradation capability beyond lysosomes, given the neutral pH of cytosol.

To rigorously confirm three-dimensional colocalization, we conducted z-axis scanning of Cell 6 using confocal laser scanning microscopy (Figure 3.15). Optical sectioning revealed co-planar fluorescence signals for NPs and released proteins and elimination of potential signal overlap artifacts from different focal planes. These findings provide conclusive evidence for genuine spatial association between the delivered enzymatic components and PET NPs within cellular architectures, supporting the feasibility of engineered intracellular nanoplastic degradation systems.

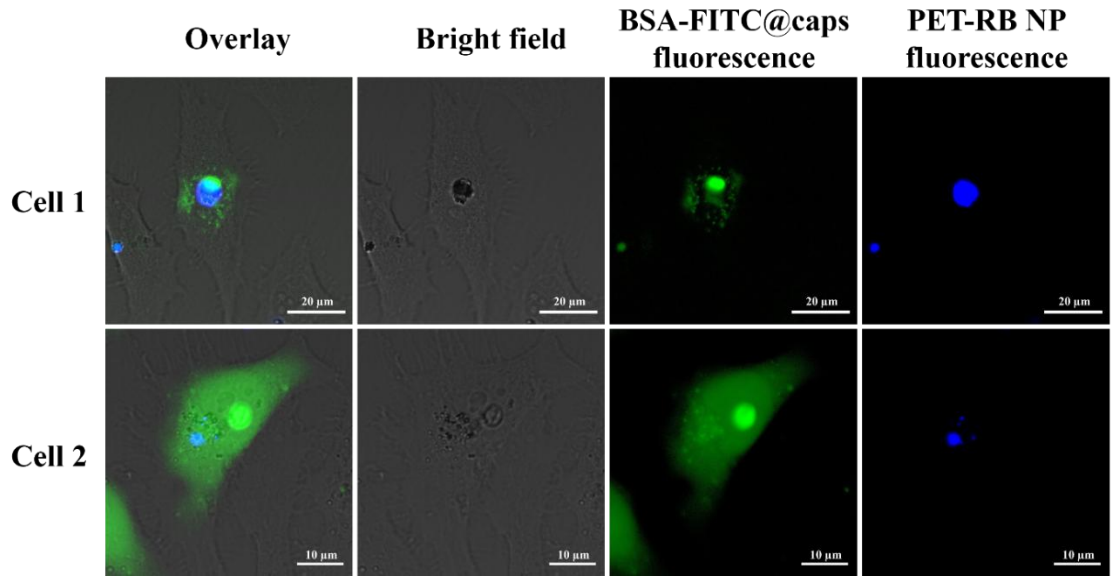

Figure 3.12. Intracellular distribution of BSA-FITC released from BSA-FITC@caps in cells co-incubated with PET-RB NPs. Fluorescence images (slightly overexposed to visualize cytosolic BSA-FITC) demonstrate partial release from endosomal/lysosomal compartments into the cytosol. Scale bars: 10 µm.

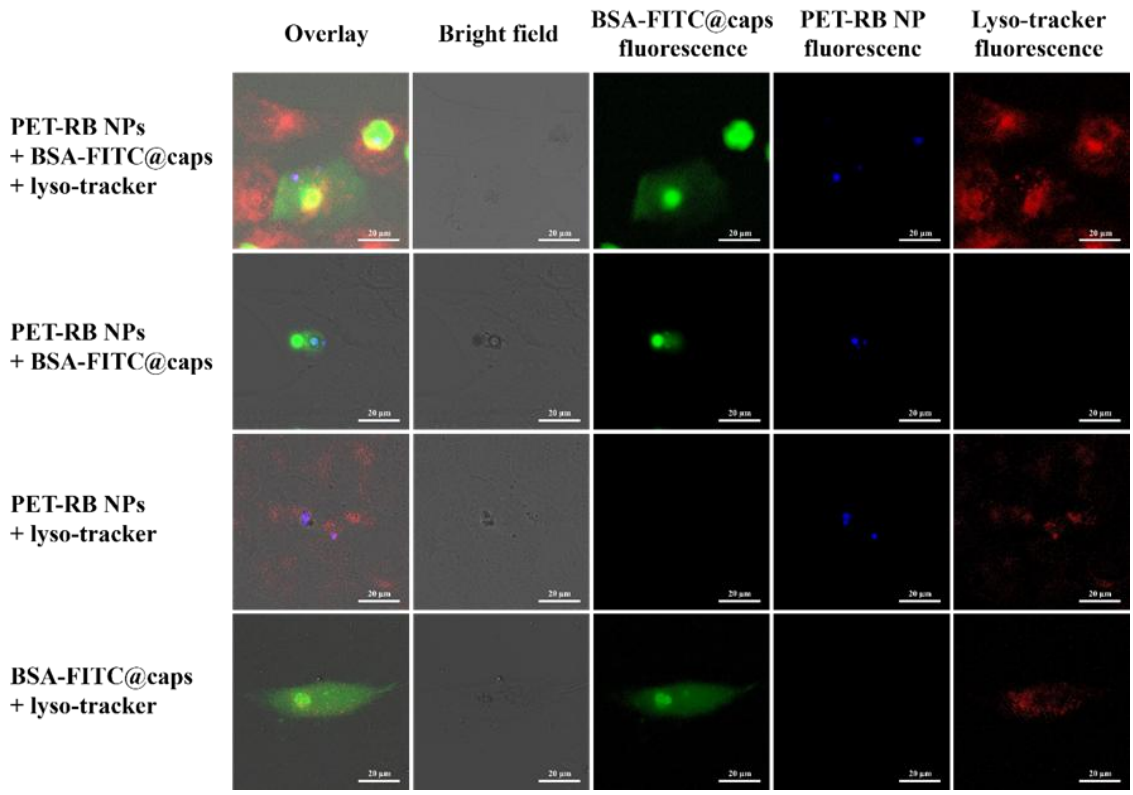

Figure 3.13. Confocal microscopy analysis of cellular uptake and compartmentalization. Cells were exposed to PET-RB NPs and BSA-FITC@caps, with lysosomal staining by LysoTracker. FITC channel overexposure highlights cytosolic protein release. Scale bars: 20 μm.

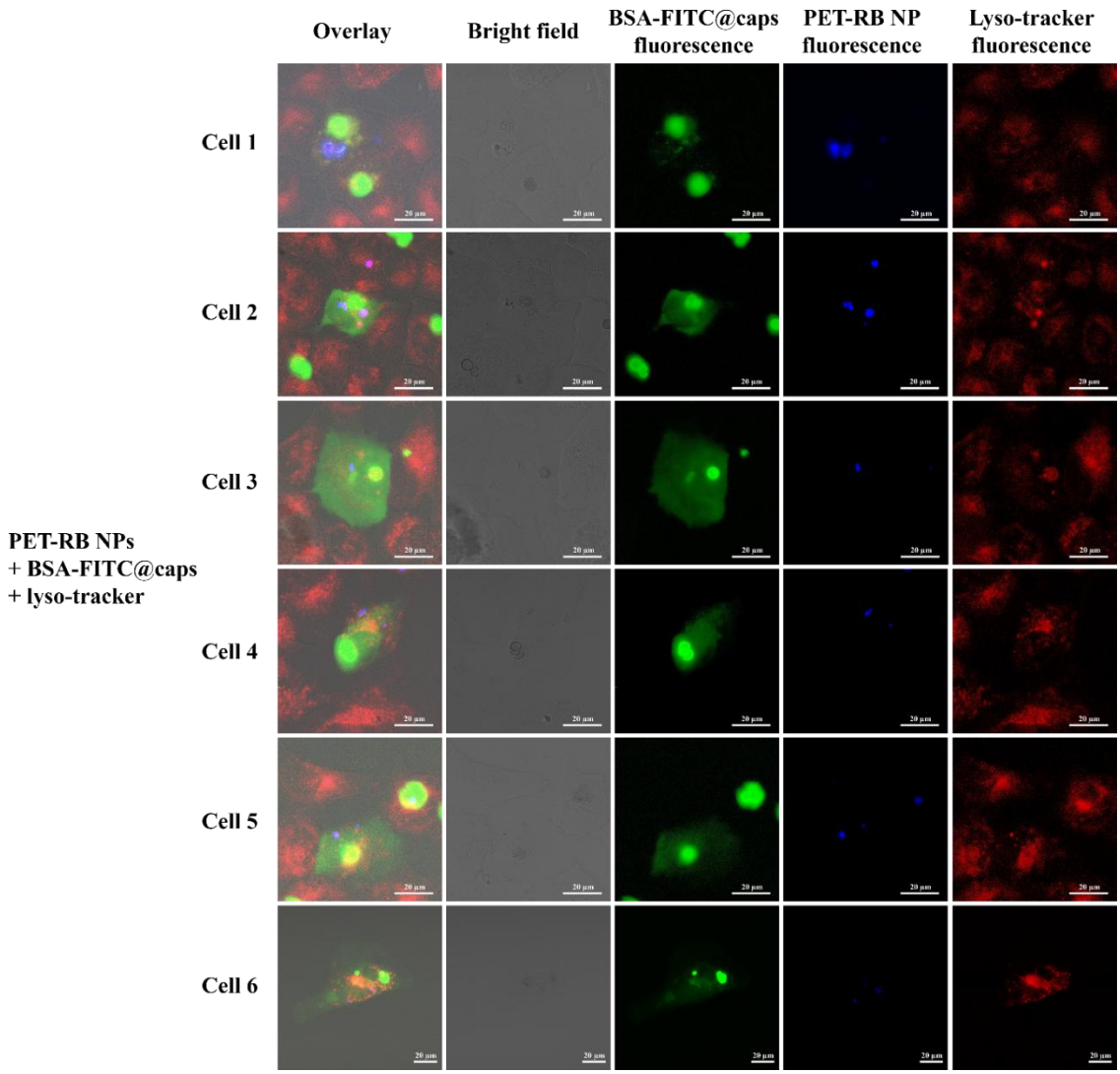

Figure 3.14. Lysosomal colocalization analysis in six cell samples treated with PET-RB NPs and BSA-FITC@caps. Overexposed FITC channel reveals both lysosome-associated and cytosolic BSA-FITC distributions. Partial colocalization between capsules and lysosomes is evident. Scale bars: 20 μm.

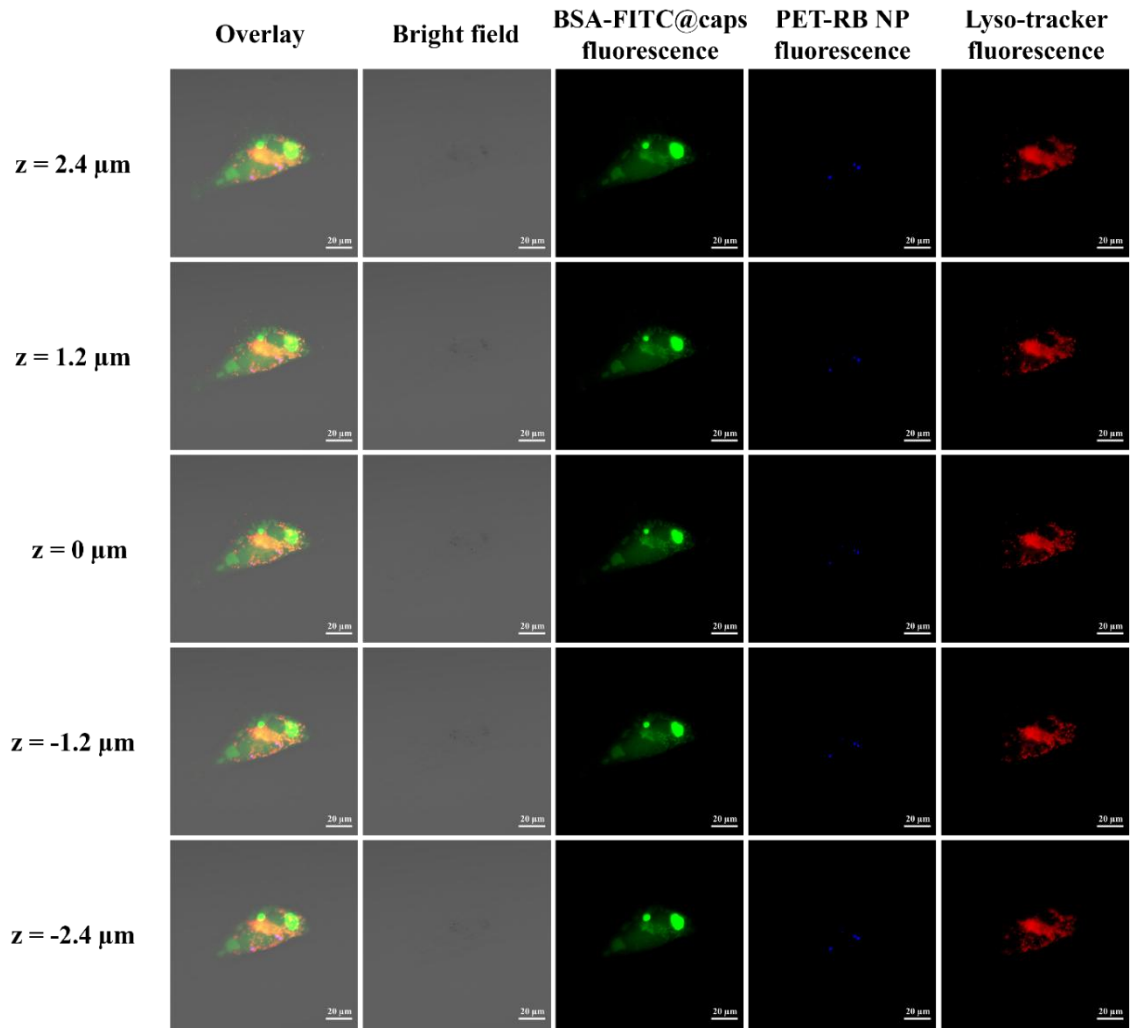

Figure 3.15. Z-stack confocal analysis (Δz = 1.2 µm) of a representative cell showing: (i) clear lysosomal accumulation of PET-RB NPs (z = 0 µm focal plane), and (ii) widespread BSA-FITC distribution (FITC channel overexposure complicates precise colocalization assessment). Scale bars: 20 µm.

3.3.7 Intracellular PET NPs degradation in multiple cells

In the subsequent phase of the investigation, we sought to determine whether polyethylene terephthalate nanoparticles (PET NPs) internalized by cells could be degraded by endocytosed PETase-loaded capsules (PETase@caps). To address this question, HeLa cells were initially incubated with rhodamine B-labeled PET NPs (PET-RB NPs) for a period of 24 h. Following this incubation, extracellular PET-RB NPs that had not been internalized were removed with PBS. To evaluate the potential degradation

of internalized PET-RB NPs, the cells were subsequently exposed to PETase@caps for an additional 24 h. After this treatment period, the cells were washed again to remove any extracellular remnants, and the rhodamine B (RB) fluorescence intensity, indicative of the remaining PET-RB NPs, was quantified using a microplate reader (see Figure 3.16). As a control, an identical experimental procedure was conducted in parallel, omitting the addition of PETase@caps to account for any nonspecific changes in fluorescence.

In the control experiment, the RB fluorescence intensity remained constant over time, reflecting the presence of internalized PET-RB NPs that were not subjected to enzymatic degradation. Although the NPs could be redistributed among daughter cells during cell proliferation, this redistribution did not alter the total quantity of NPs within the cell population, resulting in a stable fluorescence signal. The size of the PET-RB NPs precluded efficient exocytosis, as supported by prior studies [243-246], further confirming that the observed fluorescence was attributable to intracellular NPs.

In contrast, the experimental group treated with PETase@caps exhibited a temporal decline in RB fluorescence intensity. This reduction suggests that the co-localization of PETase@caps and PET-RB NPs within the cells led to the enzymatic degradation of the NPs. The resulting fragments, being smaller in size, may have been sufficiently reduced to permit exocytosis. These fragments, along with their associated fluorescence, were likely removed during the washing steps prior to fluorescence measurement. The observed decrease in intracellular RB fluorescence thus indicates partial degradation of the PET-RB NPs and subsequent removal of the degradation products via exocytosis. Importantly, since non-internalized PET-RB NPs had been eliminated from the extracellular medium prior to the addition of PETase@caps, the degradation of PET-RB NPs is inferred to have occurred intracellularly rather than extracellularly.

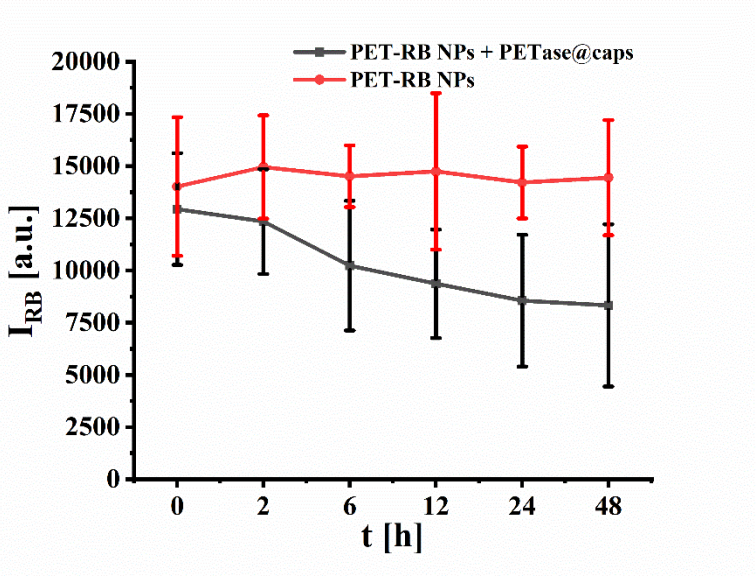

Figure 3.16. Time-dependent fluorescence intensity I_{RB} of intracellular PET-RB NPs in cells co-incubated with PETase@caps ((DEXS/pARG)$_2$/(DEXS/PEI)$_2$ shell geometry). Control: PET-RB NPs alone. Data represent mean ± SD (n = 20 wells).

3.3.8 Intracellular PET NPs degradation in single cells

To further substantiate these findings, we conducted single-cell resolution analysis of intracellular polyethylene terephthalate nanoparticle (PET-RB NP) degradation kinetics. The experimental protocol comprised sequential phases: (1) cellular internalization of PET-RB NPs during 24 h incubation, followed by rigorous washing to eliminate extracellular NPs; (2) enzymatic activation via introduction of PETase-encapsulated capsules [(DEXS/pARG)$_2$/(DEXS/PEI)$_2$]; and (3) lysosomal compartment visualization using LysoTracker™ Deep Red staining prior to confocal microscopy imaging (Figure 3.17, lower panels). Control groups, either lacking PETase@caps or PET-RB NPs, were processed in parallel (Figure 3.17, upper panels). Results revealed a marked reduction in fluorescence intensity of intracellular PET-RB NPs (demarcated by white circles) compared to extracellular NPs in treated samples, while control groups maintained stable fluorescence signals. This observation suggests that the co-localization of PET-RB NPs and PETase@caps within cells leads to the partial degradation of PET-RB NPs, with the resulting fragments being exocytosed, thereby reducing the intracellular fluorescence signal over time.

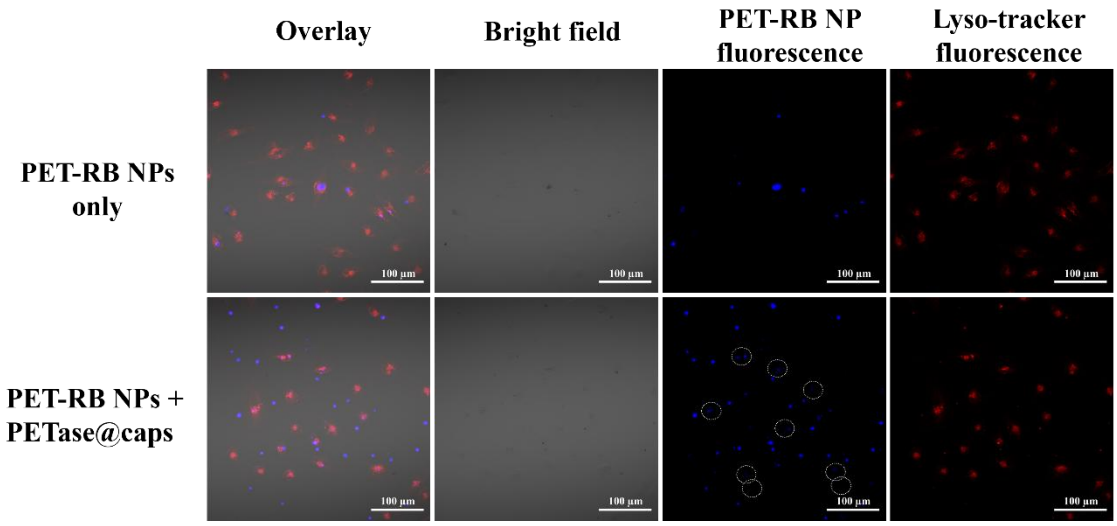

Figure 3.17. a) Fluorescence images of cells after 24 h incubation with PET-RB NPs with/without PETase@caps. Circles highlight intracellular PET-RB NPs in treated samples. Scale bars: 100 µm.

The workflow for the data evaluation with the example of Figure 3.19 is presented in Figure 3.18. For the quantitative assessment of intracellular polyethylene terephthalate-rhodamine B nanoparticle (PET-RB NP) degradation, the region of interest (ROI) was meticulously defined by manually delineating the area encompassing intracellular PET-RB NPs using the "Draw rectangle" tool within the imaging software, as depicted in Figure 3.18a. The software subsequently computed the average mean signal intensity within the designated rectangular ROI, demarcated by an orange box in Figure 3.18b, for the image corresponding to the time point t = 2 h. In this particular instance, the area of the orange box (ROI) was precisely calculated to be A_{ROI} = 424,061,776.048 nm². The mean fluorescence intensity in the rhodamine B (RB) channel was quantified as I_{RB} = 870.22, whereas the mean intensity in the bright-field channel, which was excluded from further analysis, was recorded as I_{bright_field} = 26,430.542.

This analytical protocol was methodically replicated for images captured at subsequent time points. For example, Figure 3.18c illustrates the image corresponding to the time point t = 6 h. To ensure consistency and comparability across all time points, the area of the orange box (ROI) was rigorously maintained at A_{ROI} = 424,061,776.048 nm²

for all images. However, to accommodate potential cellular motility during the experimental duration, the spatial coordinates of the ROI were dynamically adjusted in alignment with the new cellular position. For the t = 6 h time point, the mean fluorescence intensity in the RB channel was measured as I_{RB} = 604.430, and the mean intensity in the bright-field channel was recorded as I_{bright_field} = 21,380.027.

This methodological framework was uniformly applied to all time points within a single experimental series, facilitating the acquisition of IRB values for each respective time point. The resultant dataset yielded a temporal profile of PET-RB NP fluorescence intensity, which was subsequently employed to evaluate the kinetics of intracellular nanoparticle degradation. This rigorous and standardized analytical approach ensured the reliability, reproducibility, and precision of the quantitative fluorescence measurements throughout the experimental timeline, thereby providing a robust foundation for the interpretation of intracellular degradation dynamics.

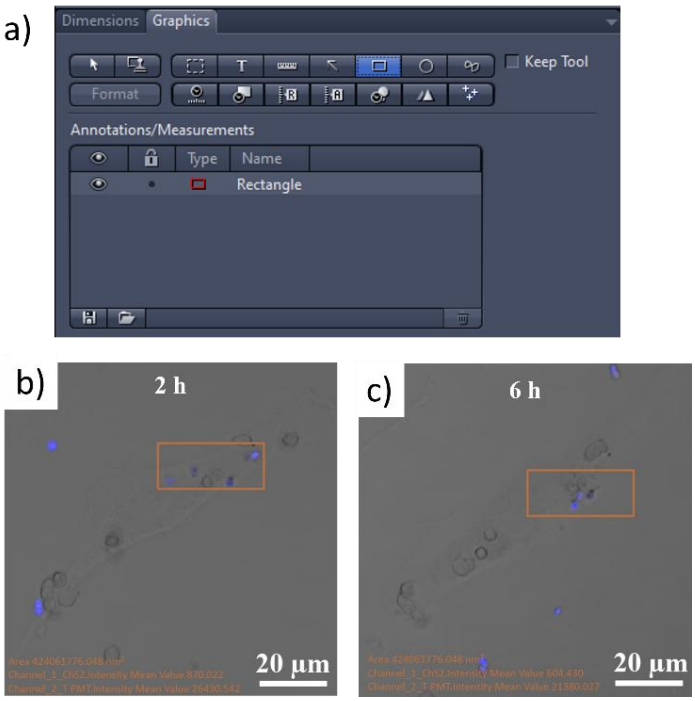

Figure 3.18. a) Manual region-of-interest (ROI) selection protocol using ZEN software. b, c) Representative ROIs (orange boxes) analyzed at t = 2 h and 6 h. Quantified parameters per ROI: Area (A_{ROI}); Mean RB fluorescence intensity (I_{RB}); Mean bright-field intensity ($I_{bright\text{-}field}$).

To quantitatively assess this phenomenon, a time-lapse imaging approach was employed, capturing a series of images at distinct time points during the incubation period t (48 h) after adding capsules. The fluorescence intensity of individual PET-RB NPs was tracked over time.

Data for cells exposed to first PET-RB NPs and then to PETase@caps are presented in Figure 3.19 and Figure 3.20. Data for cells exposed to PET-RB NPs only (here instead of the addition of PETase@caps only medium was added) are given in Figure 3.21, Figure 3.22 and Figure 3.23. Data for cells exposed to PETase@caps only are given in Figure 3.24 and Figure 3.25. For experiments involving PETase-loaded capsules (PETase@caps), specifically in the presence of both PET-RB NPs and PETase@caps or PETase@caps alone, the incubation time (t = 0) was defined as the point at which PETase@caps were introduced to the cells. In contrast, for experiments involving PET-RB NPs alone (i.e., absence of PETase@caps), t = 0 was defined as the time of PET-RB NP addition.

The experimental results demonstrate a significant acceleration in fluorescence decay when cells were co-exposed to both PET-RB NPs and PETase@caps, with over 60% reduction in fluorescence intensity observed within 48 h. This pronounced decrease provides compelling evidence that the encapsulated PETase maintains substantial enzymatic activity within intracellular environments, enabling efficient degradation of plastic nanoparticles during this timeframe. The degradation kinetics suggest that PET nanoparticles are likely broken down into smaller molecular fragments, which may facilitate subsequent cellular exocytosis processes. Control experiments revealed critical comparative data: 1) Cells exposed solely to PET-RB NPs maintained stable fluorescence intensity throughout the 48-hour observation period, confirming the inherent stability of these nanoparticles against non-enzymatic degradation by cellular or environmental factors; 2) PETase@caps-only treatments showed no detectable fluorescence signal, eliminating potential interference from autofluorescence in experimental measurements.

These collective findings establish that our engineered cellular system achieves effective intracellular degradation of plastic nanoparticles through the synergistic action of: 1) Efficient cellular internalization enzyme-loaded capsules; 2) Preservation of PETase activity in intracellular compartments; 3) Progressive biodegradation of PET polymers into excretable byproducts.

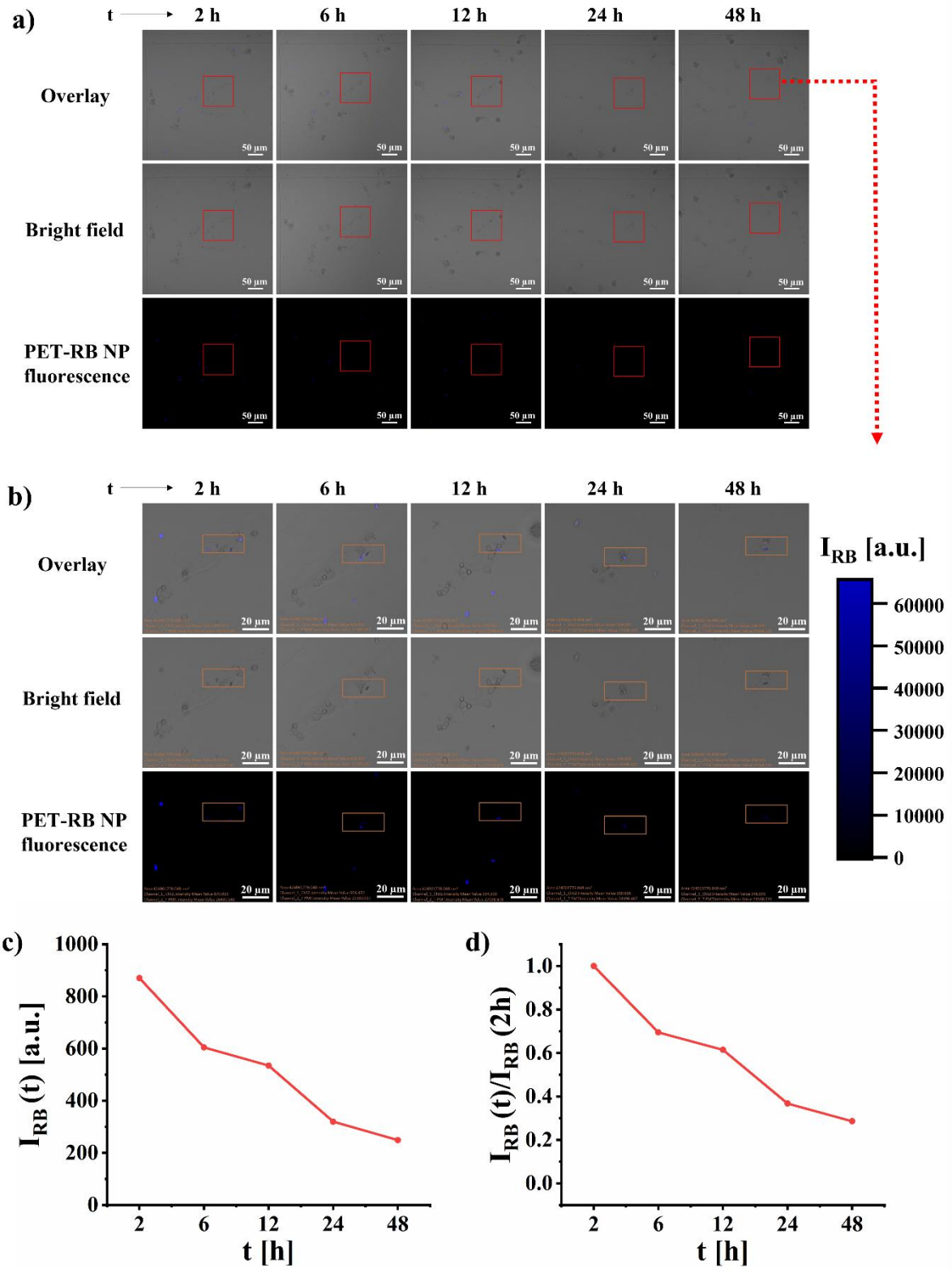

Figure 3.19. Time-resolved PET-RB NP degradation by PETase@caps. a) Sequential treatment: Cells incubated with PET-RB NPs (Day 0) followed by PETase@caps (Day 1). Bright-field and RB fluorescence images acquired at post-treatment intervals (t). Scale

bars: 50 µm. b) Magnified view (red box in (a)) tracking NP-containing regions. Scale bars: 20 µm. The orange box indicates the analysis area moved with cell migration. c) Time course of I_{RB} in selected areas. d) Normalized I_{RB} (to t = 2 h baseline).

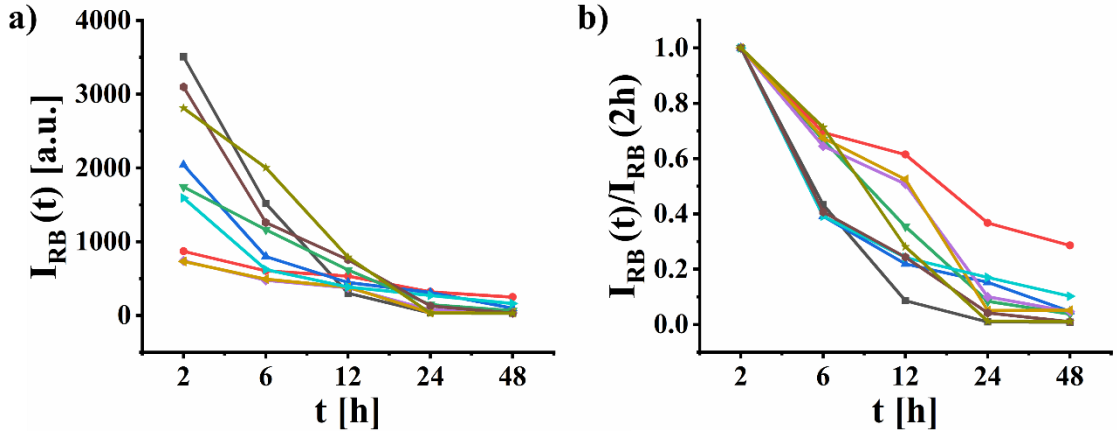

Figure 3.20. Results of cellular exposure to PET-RB NPs and PETase@caps. Time-dependent fluorescence intensity I_{RB} of intracellular PET-RB NPs in cells co-incubated with PETase@caps $((DEXS/pARG)_2/(DEXS/PEI)_2$ shell geometry).

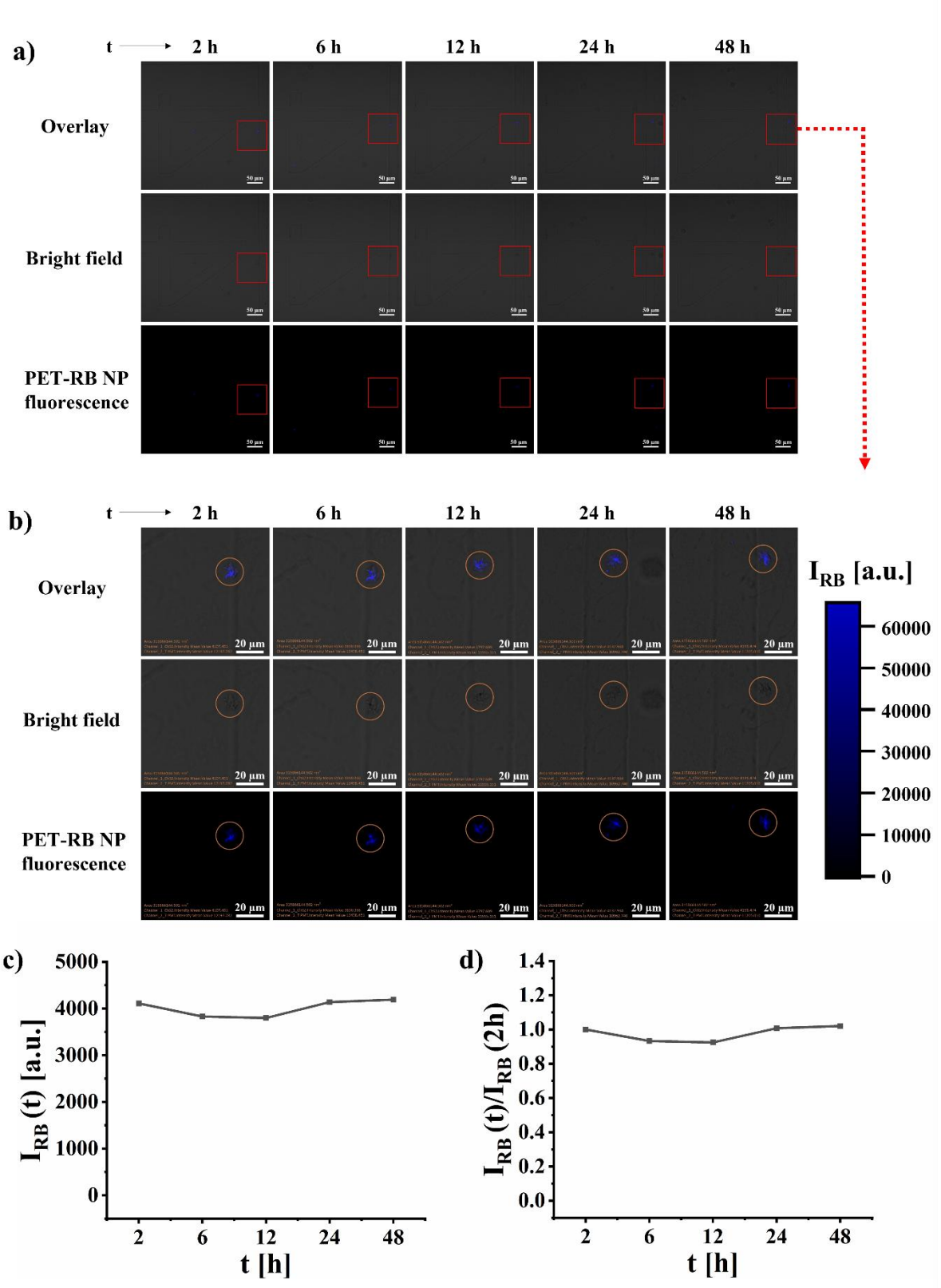

Figure 3.21. An example of PET-RB NPs only. Time-dependent fluorescence intensity I_{RB} of PET-RB NPs in cells. For further explanation see the legend of Figure 3.19.

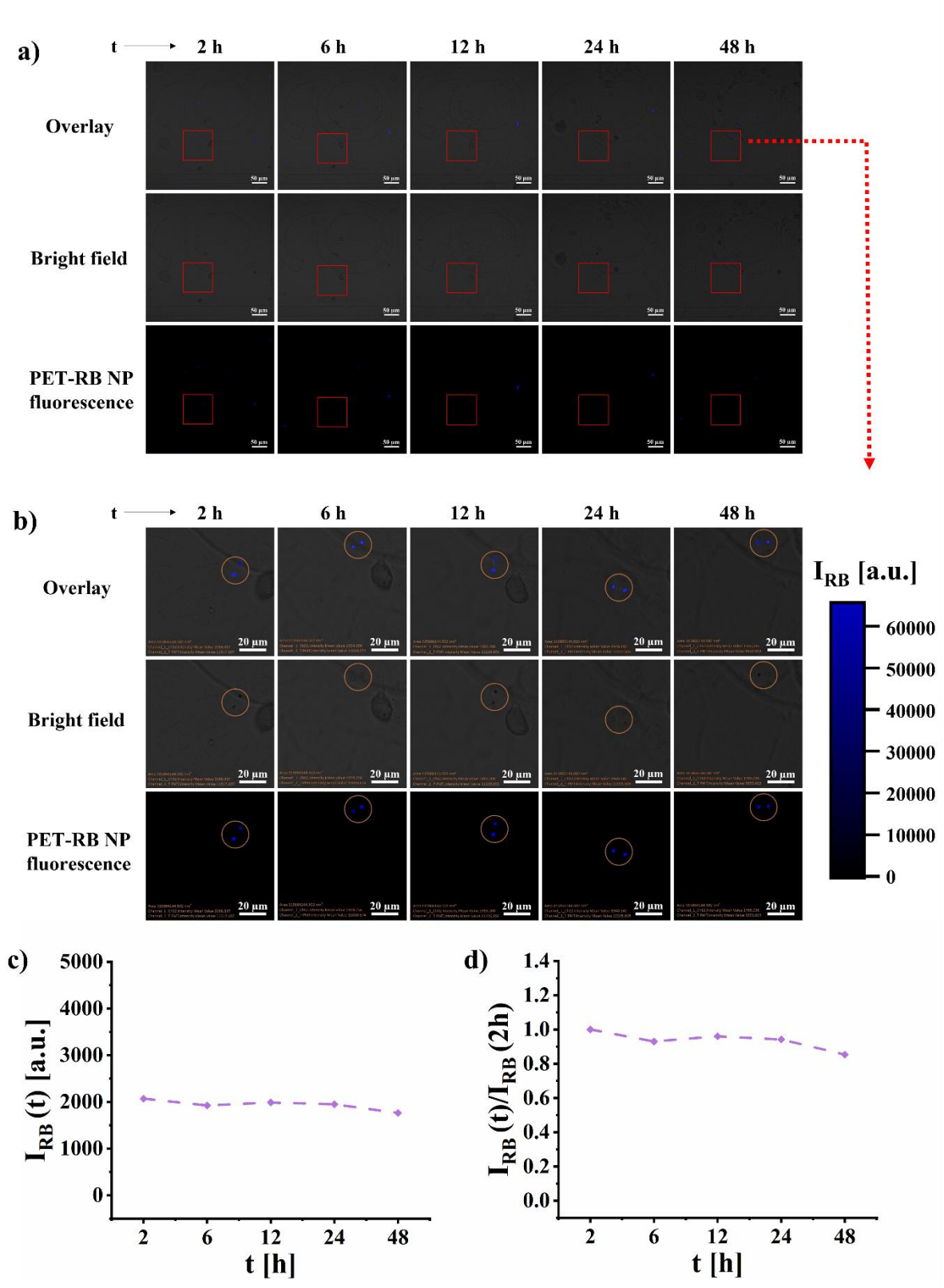

Figure 3.22. An example of PET-RB NPs only. Time-dependent fluorescence intensity I_{RB} of PET-RB NPs outside cells. For further explanation see the legend of Figure 3.19.

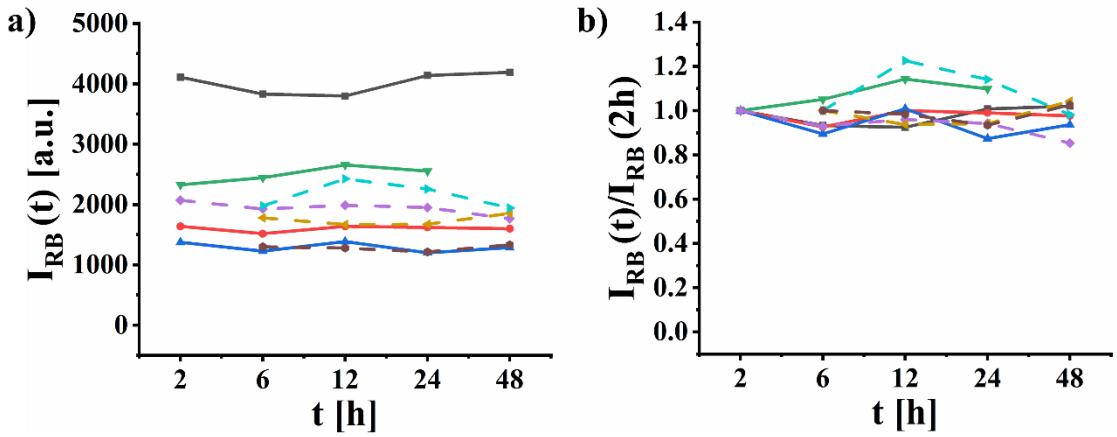

Figure 3.23. Results of cellular exposure to PET-RB NPs only. Time-dependent fluorescence intensity I_{RB} of intracellular PET-RB NPs inside/outside cells. The solid and dashed lines represent PET-RB NPs inside and outside of cells, respectively.

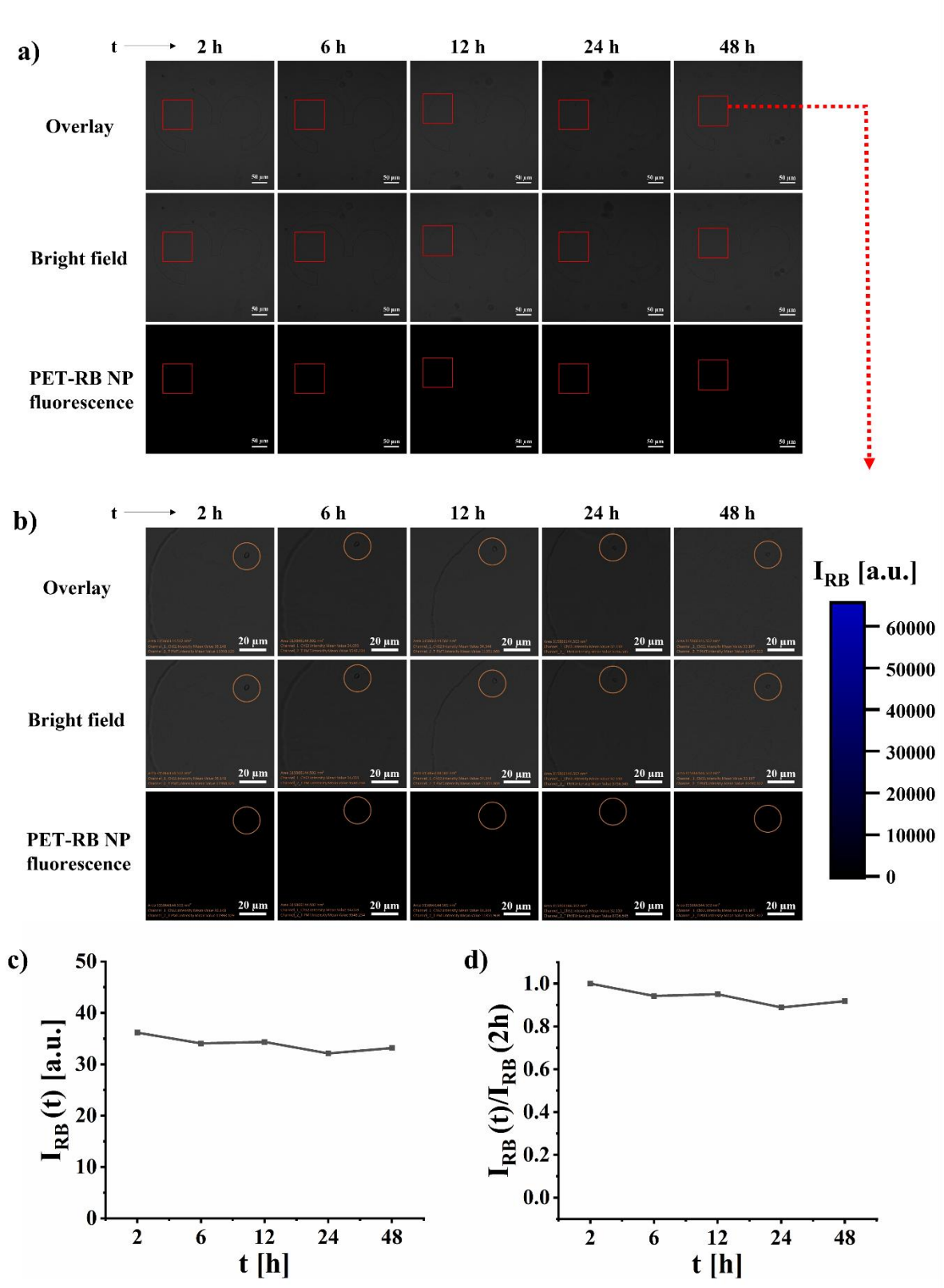

Figure 3.24. An example of PETase@caps only. For further explanation see the legend of Figure 3.19.

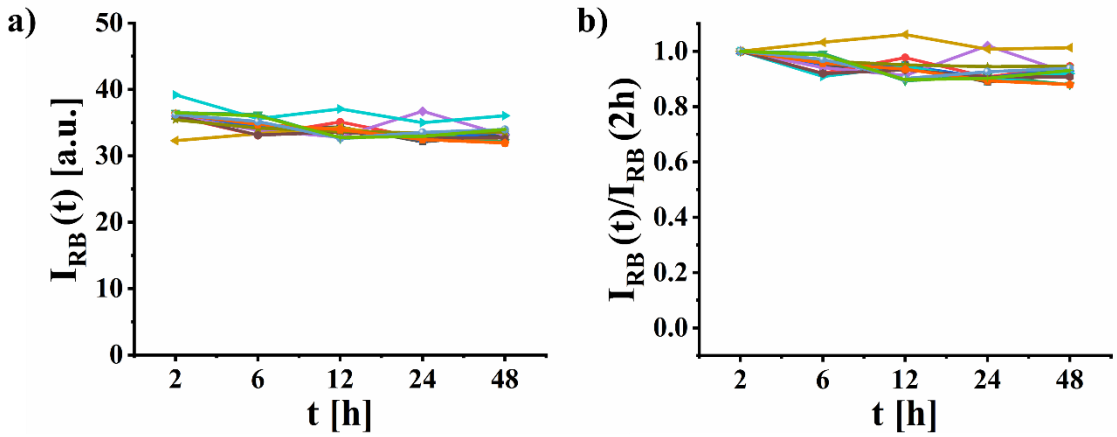

Figure 3.25. Results of cellular exposure to PETase@case only. Time-dependent fluorescence intensity I_{RB} of PETase@caps ((DEXS/pARG)$_2$/(DEXS/PEI)$_2$ shell geometry) in cells.

3.4 Conclusion

In summary, the data collectively demonstrate that the presence of PETase-loaded capsules (PETase@caps) within the same cell as polyethylene terephthalate-rhodamine B nanoparticles (PET-RB NPs) facilitates the degradation of the PET-RB NPs. This finding provides a proof-of-concept validation for the idea that internalized plastic nanoparticles (NPs) can be effectively cleared by endocytosed PETase@caps. However, several critical challenges remain to be addressed beyond this initial demonstration. Firstly, the degradation products of PET-RB NPs, including PET-dimer ($M(HET)_2$), methyl bis(2-hydroxyethyl terephthalate), and PET-trimer ($M(HET)_3$), methyl tris(2-hydroxyethyl terephthalate), are known to exhibit [247]. To mitigate the toxicity associated with plastic NPs, future enzymatic degradation strategies should aim to produce non-toxic byproducts. Additionally, the degradation fragments must be sufficiently small to enable efficient exocytosis, raising questions about the specificity of enzymatic degradation—specifically, whether different types of plastic NPs can be selectively degraded by distinct enzymes within cellular environments. Furthermore, the mechanisms underlying the intracellular co-localization of PET-RB NPs and PETase@caps remain incompletely understood, including the functional longevity of the encapsulated enzymes within cells.

Despite these challenges, the potential applications of PETase@caps as "intracellular organelles" warrant further exploration. The encapsulation of enzymes within cells offers significant advantages over free enzymes, as the intracellular environment provides protection against degradation and enables targeted enzymatic activity at specific cellular locations. The demonstrated degradation efficiency (60% within 48 h) represents a significant advancement in developing cellular platforms for nanoplastic remediation, with potential applications in environmental biotechnology and therapeutic interventions against plastic particle accumulation. Further studies are warranted to characterize the exact degradation products and their cellular export mechanisms.

4 Summary and outlook

In summary, this study introduces an innovative microcapsule-based platform that simultaneously tackles two fundamental challenges in nanomaterial engineering: optimizing intracellular nanoparticle transport and enabling cellular nanoplastic degradation. Through the development of stimuli-responsive polyelectrolyte capsules, we have achieved precise spatiotemporal control over nanoparticle delivery while establishing a novel approach for enzymatic breakdown of internalized plastics. Key findings demonstrate that PEGylation parameters (including terminal group chemistry) and calcein co-encapsulation significantly enhance nanoparticle diffusion kinetics in the cytosol, addressing critical barriers in intracellular drug delivery. Furthermore, the successful implementation of enzyme-loaded capsules for PET nanoparticle degradation within endolysosomal compartments validates the feasibility of engineered cellular systems for environmental nanoplastic remediation. These dual advancements not only provide mechanistic insights into intracellular nanoparticle behavior but also establish a versatile platform with broad applications in both therapeutic delivery and environmental biotechnology.

The microcapsule platform developed in this work represents a significant advancement in intracellular delivery systems, with unique capabilities for both biomedical and environmental applications. For therapeutic nanoparticle delivery, our quantitative analysis of post-endosomal diffusion kinetics reveals previously underappreciated design parameters that critically influence cytosolic transport. The finding that terminal PEG chemistry and small molecule co-loading can dramatically enhance nanoparticle mobility suggests new strategies to overcome one of the most persistent bottlenecks in drug delivery - inefficient trafficking to subcellular targets. Future studies should explore whether these principles extend to other nanoparticle classes (e.g., lipid-based, metallic oxides) and more complex intracellular environments (e.g., polarized cells, 3D organoids).

From an environmental health perspective, the successful demonstration of intracellular nanoplastic degradation opens several promising research avenues. The PETase@caps system provides a blueprint for engineering "cellular cleanup" mechanisms against accumulating environmental pollutants in the human body. However, three key challenges must be addressed: (i) Expanding the range of degradable

plastics beyond PET; (ii) Improving byproduct management through coupled metabolic pathways that convert degradation fragments to non-toxic metabolites; and (iii) Developing targeted delivery strategies to relevant cell types (e.g., liver macrophages for systemic nanoplastic clearance).

List of hazardous substances

List of hazardous substances used in the work

Substance	Signal word	GHS pictograms	Hazard Sentences (H-)	Precaution Sentences (P-)
0.05% trypsin/EDTA	Warning	GHS07	H290-H319	P305+P351+P338
2,2′-Azobis(2-methylpropionitrile)	Danger	GHS02, GHS07	H242-H302-H312-H315-H319-H335	P210-P280-P302+P352-P305+P351+P338
6-Aza-2-thiothymine	Warning	GHS07	H302-H315-H319-H335	P261-P305+P351+P338
Branched poly(ethyleneimine)	Danger	GHS05	H314-H335	P280-P305+P351+P338-P310
Calcein	Warning	GHS07	H315-H319-H335	P261-P305+P351+P338
Calcium chloride dihydrate	Warning	GHS07	H319	P305+P351+P338
EDC hydrochloride	Danger	GHS05, GHS07	H302-H314-H317-H318	P280-P305+P351+P338-P310
EDTA disodium salt dihydrate	Warning	GHS07	H319	P305+P351+P338
Ethanol (96%)	Danger	GHS02, GHS07	H225-H319	P210-P305+P351+P338
Gold(III) chloride trihydrate	Danger	GHS05, GHS07	H314-H317	P280-P305+P351+P338-P310
Hexafluoroisopropanol	Danger	GHS02, GHS05	H225-H302-H312-H315-H318-	P210-P280-P305+P351+P338-P310

			H335-H336	
Hydrochloric acid (37%)	Danger	GHS05	H290-H314-H335	P280-P305+P351+P338-P310
Hydrogen peroxide (30%)	Danger	GHS03, GHS05	H271-H314-H318	P210-P280-P305+P351+P338-P310
Iron(II) sulfate heptahydrate	Warning	GHS07	H302-H315-H319	P305+P351+P338
n-Hexane	Danger	GHS02, GHS07, GHS08	H225-H304-H315-H336-H373-H411	P210-P301+P310-P331-P403+P233
N-hydroxysuccinimide	Warning	GHS07	H315-H319-H335	P305+P351+P338
Nitric acid (65%)	Danger	GHS03, GHS05	H272-H314-H318	P210-P280-P305+P351+P338-P310
Penicillin/streptomycin	Warning	GHS07	H317	P261-P280
Poly(allylamine hydrochloride)	Warning	GHS07	H315-H319-H335	P305+P351+P338
Poly-L-arginine hydrochloride	Warning	GHS07	H315-H319-H335	P261-P305+P351+P338
Resazurin	Warning	GHS07	H302-H319	P305+P351+P338
Rhodamine B	Warning	GHS07	H302-H312-H315-H319	P280-P305+P351+P338
Silver nitrate	Danger	GHS05, GHS07, GHS09	H290-H314-H317-H410	P273-P280-P305+P351+P338-P310

Sodium borohydride	Danger	GHS02, GHS05	H260-H302-H314	P223-P231+P232-P280-P305+P351+P338-P370+P378
Sodium carbonate	Warning	GHS07	H319	P305+P351+P338
Sodium hydroxide	Danger	GHS05	H290-H314	P280-P305+P351+P338-P310
Tetrahydrofuran	Danger	GHS02, GHS07	H225-H302-H319-H335-H351	P210-P261-P305+P351+P338
Thioctic acid	Warning	GHS07	H315-H319-H335	P305+P351+P338
Ascorbic acid	Not hazardous substance			
Bovine serum albumin	Not hazardous substance			
Dextran sulfate sodium salt	Not hazardous substance			
Dulbecco's Modified Eagles Medium	Not hazardous substance			
Fetal bovine serum	Not hazardous substance			
Phosphate buffered saline	Not hazardous substance			
Poly(sodium 4-styrenesulfonate)	Not hazardous substance			
Polyethylene terephthalate filament	Not hazardous substance			
Potassium phosphate monobasic	Not hazardous substance			
Sodium chloride	Not hazardous substance			
Sodium phosphate dibasic	Not hazardous substance			
Trisodium citrate dihydrate	Not hazardous substance			

References

[1] O.C. Farokhzad, R. Langer, Impact of nanotechnology on drug delivery, Acs Nano 3(1) (2009) 16-20.

[2] J. Shi, P.W. Kantoff, R. Wooster, O.C. Farokhzad, Cancer nanomedicine: progress, challenges and opportunities, Nature reviews cancer 17(1) (2017) 20-37.

[3] D. Rosenblum, N. Joshi, W. Tao, J.M. Karp, D. Peer, Progress and challenges towards targeted delivery of cancer therapeutics, Nat Commun 9(1) (2018) 1410.

[4] M.A. Beach, U. Nayanathara, Y. Gao, C. Zhang, Y. Xiong, Y. Wang, G.K. Such, Polymeric nanoparticles for drug delivery, Chemical Reviews 124(9) (2024) 5505-5616.

[5] A. Albanese, P.S. Tang, W.C. Chan, The effect of nanoparticle size, shape, and surface chemistry on biological systems, Annual review of biomedical engineering 14(1) (2012) 1-16.

[6] C.D. Walkey, W.C. Chan, Understanding and controlling the interaction of nanomaterials with proteins in a physiological environment, Chem Soc Rev 41(7) (2012) 2780-2799.

[7] R.A. Petros, J.M. DeSimone, Strategies in the design of nanoparticles for therapeutic applications, Nat Rev Drug Discov 9(8) (2010) 615-627.

[8] G. Sahay, D.Y. Alakhova, A.V. Kabanov, Endocytosis of nanomedicines, J Control Release 145(3) (2010) 182-195.

[9] L. Zhang, F. Gu, J. Chan, A. Wang, R. Langer, O. Farokhzad, Nanoparticles in medicine: therapeutic applications and developments, Clinical pharmacology & therapeutics 83(5) (2008) 761-769.

[10] A.C. Anselmo, S. Mitragotri, Nanoparticles in the clinic, Bioengineering & translational medicine 1(1) (2016) 10-29.

[11] S. Mura, J. Nicolas, P. Couvreur, Stimuli-responsive nanocarriers for drug delivery, Nature materials 12(11) (2013) 991-1003.

[12] S. Wilhelm, A.J. Tavares, Q. Dai, S. Ohta, J. Audet, H.F. Dvorak, W.C. Chan, Analysis of nanoparticle delivery to tumours, Nature reviews materials 1(5) (2016) 1-12.

[13] T.M. Allen, P.R. Cullis, Liposomal drug delivery systems: from concept to clinical applications, Adv Drug Deliver Rev 65(1) (2013) 36-48.

[14] R. Gref, Y. Minamitake, M.T. Peracchia, V. Trubetskoy, V. Torchilin, R. Langer, Biodegradable long-circulating polymeric nanospheres, Science 263(5153) (1994) 1600-1603.
[15] M. Liong, J. Lu, M. Kovochich, T. Xia, S.G. Ruehm, A.E. Nel, F. Tamanoi, J.I. Zink, Multifunctional inorganic nanoparticles for imaging, targeting, and drug delivery, Acs Nano 2(5) (2008) 889-896.
[16] Y. Wang, S. Sun, Z. Zhang, D. Shi, Nanomaterials for cancer precision medicine, Adv Mater 30(17) (2018) 1705660.
[17] S.O. Alhaj-Suliman, E.I. Wafa, A.K. Salem, Engineering nanosystems to overcome barriers to cancer diagnosis and treatment, Adv Drug Deliver Rev 189 (2022) 114482.
[18] G. Sierri, M. Patrucco, D. Ferrario, A. Renda, S. Comi, M. Ciprandi, V. Fontanini, F.S. Sica, S. Sesana, M. Costa Verdugo, Targeting specific brain districts for advanced nanotherapies: A review from the perspective of precision nanomedicine, Wiley Interdisciplinary Reviews: Nanomedicine and Nanobiotechnology 16(5) (2024) e1991.
[19] M.J. Mitchell, M.M. Billingsley, R.M. Haley, M.E. Wechsler, N.A. Peppas, R. Langer, Engineering precision nanoparticles for drug delivery, Nat Rev Drug Discov 20(2) (2021) 101-124.
[20] S. Pramanik, S. Mohanto, R. Manne, R.R. Rajendran, A. Deepak, S.J. Edapully, T. Patil, O. Katari, Nanoparticle-based drug delivery system: the magic bullet for the treatment of chronic pulmonary diseases, Molecular Pharmaceutics 18(10) (2021) 3671-3718.
[21] W. Park, K. Na, Advances in the synthesis and application of nanoparticles for drug delivery, Wiley Interdisciplinary Reviews: Nanomedicine and Nanobiotechnology 7(4) (2015) 494-508.
[22] Y. Cao, X. Zhao, Y. Miao, X. Wang, D. Deng, How the Versatile Self-Assembly in Drug Delivery System to Afford Multimodal Cancer Therapy?, Advanced Healthcare Materials 14(3) (2025) 2403715.
[23] K.R. Gajbhiye, R. Salve, M. Narwade, A. Sheikh, P. Kesharwani, V. Gajbhiye, Lipid polymer hybrid nanoparticles: a custom-tailored next-generation approach for cancer therapeutics, Molecular Cancer 22(1) (2023) 160.
[24] S. Wang, K. Cheng, K. Chen, C. Xu, P. Ma, G. Dang, Y. Yang, Q. Lei, H. Huang, Y. Yu, Nanoparticle-based medicines in clinical cancer therapy, Nano Today 45 (2022) 101512.

[25] A. Samad, Y. Sultana, M. Aqil, Liposomal drug delivery systems: an update review, Current drug delivery 4(4) (2007) 297-305.
[26] I. Yakavets, M. Ayachit, S. Kheiri, Z. Chen, F. Rakhshani, S. McWhirter, E.W. Young, G.C. Walker, E. Kumacheva, A microfluidic platform for evaluating the internalization of liposome drug carriers in tumor spheroids, ACS Applied Materials & Interfaces 16(8) (2024) 9690-9701.
[27] C.P. Pilkington, I. Gispert, S.Y. Chui, J.M. Seddon, Y. Elani, Engineering a nanoscale liposome-in-liposome for in situ biochemical synthesis and multi-stage release, Nature Chemistry 16(10) (2024) 1612-1620.
[28] R. Han, Z. Ren, Q. Wang, H. Zha, E. Wang, M. Wu, Y. Zheng, J.H. Lu, Synthetic Biomimetic Liposomes Harness Efferocytosis Machinery for Highly Efficient Macrophages-Targeted Drug Delivery to Alleviate Inflammation, Advanced Science 11(29) (2024) 2308325.
[29] J. Hammond, C.J. Richards, Y. Ko, T. Jonker, C. Åberg, W.H. Roos, R.B. Lira, Membrane Fusion-Based Drug Delivery Liposomes Transiently Modify the Material Properties of Synthetic and Biological Membranes, Small (2024) 2408039.
[30] B. Fonseca-Santos, M.P.D. Gremião, M. Chorilli, Nanotechnology-based drug delivery systems for the treatment of Alzheimer's disease, International Journal of nanomedicine (2015) 4981-5003.
[31] R. Alyautdin, I. Khalin, M.I. Nafeeza, M.H. Haron, D. Kuznetsov, Nanoscale drug delivery systems and the blood–brain barrier, International journal of nanomedicine (2014) 795-811.
[32] S.C. Semple, A. Akinc, J. Chen, A.P. Sandhu, B.L. Mui, C.K. Cho, D.W. Sah, D. Stebbing, E.J. Crosley, E. Yaworski, Rational design of cationic lipids for siRNA delivery, Nature biotechnology 28(2) (2010) 172-176.
[33] P.R. Cullis, M.J. Hope, Lipid nanoparticle systems for enabling gene therapies, Molecular Therapy 25(7) (2017) 1467-1475.
[34] J.A. Kulkarni, M.M. Darjuan, J.E. Mercer, S. Chen, R. Van Der Meel, J.L. Thewalt, Y.Y.C. Tam, P.R. Cullis, On the formation and morphology of lipid nanoparticles containing ionizable cationic lipids and siRNA, Acs Nano 12(5) (2018) 4787-4795.
[35] M. Yanez Arteta, T. Kjellman, S. Bartesaghi, S. Wallin, X. Wu, A.J. Kvist, A. Dabkowska, N. Székely, A. Radulescu, J. Bergenholtz, Successful reprogramming of cellular protein production through mRNA delivered by functionalized lipid

nanoparticles, Proceedings of the National Academy of Sciences 115(15) (2018) E3351-E3360.
[36] M. Jayaraman, S.M. Ansell, B.L. Mui, Y.K. Tam, J. Chen, X. Du, D. Butler, L. Eltepu, S. Matsuda, J.K. Narayanannair, Maximizing the potency of siRNA lipid nanoparticles for hepatic gene silencing in vivo, Angewandte Chemie International Edition 51(34) (2012) 8529-8533.
[37] A. Akinc, M.A. Maier, M. Manoharan, K. Fitzgerald, M. Jayaraman, S. Barros, S. Ansell, X. Du, M.J. Hope, T.D. Madden, The Onpattro story and the clinical translation of nanomedicines containing nucleic acid-based drugs, Nat Nanotechnol 14(12) (2019) 1084-1087.
[38] K.J. Hassett, K.E. Benenato, E. Jacquinet, A. Lee, A. Woods, O. Yuzhakov, S. Himansu, J. Deterling, B.M. Geilich, T. Ketova, Optimization of lipid nanoparticles for intramuscular administration of mRNA vaccines, Molecular therapy Nucleic acids 15 (2019) 1-11.
[39] Q. Cheng, T. Wei, L. Farbiak, L.T. Johnson, S.A. Dilliard, D.J. Siegwart, Selective organ targeting (SORT) nanoparticles for tissue-specific mRNA delivery and CRISPR–Cas gene editing, Nat Nanotechnol 15(4) (2020) 313-320.
[40] J. Heyes, L. Palmer, K. Bremner, I. MacLachlan, Cationic lipid saturation influences intracellular delivery of encapsulated nucleic acids, J Control Release 107(2) (2005) 276-287.
[41] M.M. Billingsley, N. Gong, A.J. Mukalel, A.S. Thatte, R. El-Mayta, S.K. Patel, A.E. Metzloff, K.L. Swingle, X. Han, L. Xue, In vivo mRNA CAR T cell engineering via targeted ionizable lipid nanoparticles with extrahepatic tropism, Small 20(11) (2024) 2304378.
[42] E.M. Clarissa, M. Karmacharya, H. Choi, S. Kumar, Y.K. Cho, Nature Inspired Delivery Vehicles for CRISPR-Based Genome Editing, Small (2025) 2409353.
[43] A. Kumari, S.K. Yadav, S.C. Yadav, Biodegradable polymeric nanoparticles based drug delivery systems, Colloids and surfaces B: biointerfaces 75(1) (2010) 1-18.
[44] N. Kamaly, B. Yameen, J. Wu, O.C. Farokhzad, Degradable controlled-release polymers and polymeric nanoparticles: mechanisms of controlling drug release, Chemical reviews 116(4) (2016) 2602-2663.

[45] F. Danhier, E. Ansorena, J.M. Silva, R. Coco, A. Le Breton, V. Préat, PLGA-based nanoparticles: an overview of biomedical applications, J Control Release 161(2) (2012) 505-522.
[46] R. Karnik, F. Gu, P. Basto, C. Cannizzaro, L. Dean, W. Kyei-Manu, R. Langer, O.C. Farokhzad, Microfluidic platform for controlled synthesis of polymeric nanoparticles, Nano letters 8(9) (2008) 2906-2912.
[47] S.B. Brown, L. Wang, R.R. Jungels, B. Sharma, Effects of cartilage-targeting moieties on nanoparticle biodistribution in healthy and osteoarthritic joints, Acta biomaterialia 101 (2020) 469-483.
[48] Z. Le, Y. Chen, H. Han, H. Tian, P. Zhao, C. Yang, Z. He, L. Liu, K.W. Leong, H.-Q. Mao, Hydrogen-bonded tannic acid-based anticancer nanoparticle for enhancement of oral chemotherapy, ACS applied materials & interfaces 10(49) (2018) 42186-42197.
[49] L. Zhang, A. Beatty, L. Lu, A. Abdalrahman, T.M. Makris, G. Wang, Q. Wang, Microfluidic-assisted polymer-protein assembly to fabricate homogeneous functionalnanoparticles, Materials Science and Engineering: C 111 (2020) 110768.
[50] K. Avgoustakis, A. Beletsi, Z. Panagi, P. Klepetsanis, A. Karydas, D. Ithakissios, PLGA–mPEG nanoparticles of cisplatin: in vitro nanoparticle degradation, in vitro drug release and in vivo drug residence in blood properties, J Control Release 79(1-3) (2002) 123-135.
[51] R. Duncan, Polymer conjugates as anticancer nanomedicines, Nature reviews cancer 6(9) (2006) 688-701.
[52] S. De Koker, L.J. De Cock, P. Rivera_Gil, W.J. Parak, R.A. Velty, C. Vervaet, J.P. Remon, J. Grooten, B.G. De Geest, Polymeric multilayer capsules delivering biotherapeutics, Adv Drug Deliver Rev 63(9) (2011) 748-761.
[53] M. Elsabahy, K.L. Wooley, Design of polymeric nanoparticles for biomedical delivery applications, Chem Soc Rev 41(7) (2012) 2545-2561.
[54] G. Gaucher, M.-H. Dufresne, V.P. Sant, N. Kang, D. Maysinger, J.-C. Leroux, Block copolymer micelles: preparation, characterization and application in drug delivery, J Control Release 109(1-3) (2005) 169-188.
[55] C. Vauthier, K. Bouchemal, Methods for the preparation and manufacture of polymeric nanoparticles, Pharmaceutical research 26 (2009) 1025-1058.

[56] B.M. Discher, Y.-Y. Won, D.S. Ege, J.C. Lee, F.S. Bates, D.E. Discher, D.A. Hammer, Polymersomes: tough vesicles made from diblock copolymers, Science 284(5417) (1999) 1143-1146.
[57] D.A. Christian, S. Cai, D.M. Bowen, Y. Kim, J.D. Pajerowski, D.E. Discher, Polymersome carriers: from self-assembly to siRNA and protein therapeutics, European Journal of Pharmaceutics and Biopharmaceutics 71(3) (2009) 463-474.
[58] H. Otsuka, Y. Nagasaki, K. Kataoka, PEGylated nanoparticles for biological and pharmaceutical applications, Adv Drug Deliver Rev 55(3) (2003) 403-419.
[59] Y. Miele, G. Holló, I. Lagzi, F. Rossi, Shape deformation, budding and division of giant vesicles and artificial cells: A review, Life 12(6) (2022) 841.
[60] T. Hamaguchi, Y. Matsumura, M. Suzuki, K. Shimizu, R. Goda, I. Nakamura, I. Nakatomi, M. Yokoyama, K. Kataoka, T. Kakizoe, NK105, a paclitaxel-incorporating micellar nanoparticle formulation, can extend in vivo antitumour activity and reduce the neurotoxicity of paclitaxel, British journal of cancer 92(7) (2005) 1240-1246.
[61] K. Kataoka, A. Harada, Y. Nagasaki, Block copolymer micelles for drug delivery: design, characterization and biological significance, Adv Drug Deliver Rev 64 (2012) 37-48.
[62] D.A. Tomalia, H. Baker, J. Dewald, M. Hall, G. Kallos, S. Martin, J. Roeck, J. Ryder, P. Smith, A new class of polymers: starburst-dendritic macromolecules, Polymer journal 17(1) (1985) 117-132.
[63] I.J. Majoros, A. Myc, T. Thomas, C.B. Mehta, J.R. Baker, PAMAM dendrimer-based multifunctional conjugate for cancer therapy: synthesis, characterization, and functionality, Biomacromolecules 7(2) (2006) 572-579.
[64] C. Kojima, B. Turkbey, M. Ogawa, M. Bernardo, C.A. Regino, L.H. Bryant Jr, P.L. Choyke, K. Kono, H. Kobayashi, Dendrimer-based MRI contrast agents: the effects of PEGylation on relaxivity and pharmacokinetics, Nanomedicine: Nanotechnology, Biology and Medicine 7(6) (2011) 1001-1008.
[65] O. Boussif, F. Lezoualc'h, M.A. Zanta, M.D. Mergny, D. Scherman, B. Demeneix, J.-P. Behr, A versatile vector for gene and oligonucleotide transfer into cells in culture and in vivo: polyethylenimine, Proceedings of the National Academy of Sciences 92(16) (1995) 7297-7301.
[66] D. Shcharbin, A. Janaszewska, B. Klajnert-Maculewicz, B. Ziemba, V. Dzmitruk, I. Halets, S. Loznikova, N. Shcharbina, K. Milowska, M. Ionov, How to study dendrimers

and dendriplexes III. Biodistribution, pharmacokinetics and toxicity in vivo, J Control Release 181 (2014) 40-52.
[67] J. Wankar, N.G. Kotla, S. Gera, S. Rasala, A. Pandit, Y.A. Rochev, Recent advances in host–guest self-assembled cyclodextrin carriers: Implications for responsive drug delivery and biomedical engineering, Adv Funct Mater 30(44) (2020) 1909049.
[68] M.I. Giannotti, O. Esteban, M. Oliva, M.F. García-Parajo, F. Sanz, pH-responsive polysaccharide-based polyelectrolyte complexes as nanocarriers for lysosomal delivery of therapeutic proteins, Biomacromolecules 12(7) (2011) 2524-2533.
[69] M.A. Mintzer, M.W. Grinstaff, Biomedical applications of dendrimers: a tutorial, Chem Soc Rev 40(1) (2011) 173-190.
[70] X. Huang, P.K. Jain, I.H. El-Sayed, M.A. El-Sayed, Gold nanoparticles: interesting optical properties and recent applications in cancer diagnostics and therapy, Nanomedicine-Uk 2(5) (2007) 681-693.
[71] C.J. Murphy, A.M. Gole, J.W. Stone, P.N. Sisco, A.M. Alkilany, E.C. Goldsmith, S.C. Baxter, Gold nanoparticles in biology: beyond toxicity to cellular imaging, Accounts of chemical research 41(12) (2008) 1721-1730.
[72] X. Huang, I.H. El-Sayed, W. Qian, M.A. El-Sayed, Cancer cell imaging and photothermal therapy in the near-infrared region by using gold nanorods, Journal of the American Chemical Society 128(6) (2006) 2115-2120.
[73] D.A. Giljohann, D.S. Seferos, W.L. Daniel, M.D. Massich, P.C. Patel, C.A. Mirkin, Gold nanoparticles for biology and medicine, Spherical nucleic acids (2020) 55-90.
[74] E.C. Dreaden, A.M. Alkilany, X. Huang, C.J. Murphy, M.A. El-Sayed, The golden age: gold nanoparticles for biomedicine, Chem Soc Rev 41(7) (2012) 2740-2779.
[75] L.C. Kennedy, L.R. Bickford, N.A. Lewinski, A.J. Coughlin, Y. Hu, E.S. Day, J.L. West, R.A. Drezek, A new era for cancer treatment: gold-nanoparticle-mediated thermal therapies, Small 7(2) (2011) 169-183.
[76] S. Laurent, D. Forge, M. Port, A. Roch, C. Robic, L. Vander Elst, R.N. Muller, Magnetic iron oxide nanoparticles: synthesis, stabilization, vectorization, physicochemical characterizations, and biological applications, Chemical reviews 108(6) (2008) 2064-2110.
[77] J. Wahsner, E.M. Gale, A. Rodríguez-Rodríguez, P. Caravan, Chemistry of MRI contrast agents: current challenges and new frontiers, Chemical reviews 119(2) (2018) 957-1057.

[78] A.C. Anselmo, S. Mitragotri, Nanoparticles in the clinic: An update, Bioengineering & translational medicine 4(3) (2019) e10143.
[79] F. Tang, L. Li, D. Chen, Mesoporous silica nanoparticles: synthesis, biocompatibility and drug delivery, Adv Mater 24(12) (2012) 1504-1534.
[80] X. Michalet, F.F. Pinaud, L.A. Bentolila, J.M. Tsay, S. Doose, J.J. Li, G. Sundaresan, A. Wu, S. Gambhir, S. Weiss, Quantum dots for live cells, in vivo imaging, and diagnostics, science 307(5709) (2005) 538-544.
[81] A.M. Smith, S. Nie, Semiconductor nanocrystals: structure, properties, and band gap engineering, Accounts of chemical research 43(2) (2010) 190-200.
[82] S.J. Soenen, P. Rivera-Gil, J.-M. Montenegro, W.J. Parak, S.C. De Smedt, K. Braeckmans, Cellular toxicity of inorganic nanoparticles: common aspects and guidelines for improved nanotoxicity evaluation, Nano Today 6(5) (2011) 446-465.
[83] S. Sharifi, S. Behzadi, S. Laurent, M.L. Forrest, P. Stroeve, M. Mahmoudi, Toxicity of nanomaterials, Chem Soc Rev 41(6) (2012) 2323-2343.
[84] S. Mitragotri, P.A. Burke, R. Langer, Overcoming the challenges in administering biopharmaceuticals: formulation and delivery strategies, Nat Rev Drug Discov 13(9) (2014) 655-672.
[85] M.A. Dobrovolskaia, S.E. McNeil, Understanding the correlation between in vitro and in vivo immunotoxicity tests for nanomedicines, J Control Release 172(2) (2013) 456-466.
[86] V.P. Torchilin, Multifunctional nanocarriers, Adv Drug Deliver Rev 58(14) (2006) 1532-1555.
[87] A.E. Nel, L. Mädler, D. Velegol, T. Xia, E.M. Hoek, P. Somasundaran, F. Klaessig, V. Castranova, M. Thompson, Understanding biophysicochemical interactions at the nano–bio interface, Nature materials 8(7) (2009) 543-557.
[88] W. Poon, B.R. Kingston, B. Ouyang, W. Ngo, W.C. Chan, A framework for designing delivery systems, Nat Nanotechnol 15(10) (2020) 819-829.
[89] E. Blanco, H. Shen, M. Ferrari, Principles of nanoparticle design for overcoming biological barriers to drug delivery, Nature biotechnology 33(9) (2015) 941-951.
[90] D.E. Owens III, N.A. Peppas, Opsonization, biodistribution, and pharmacokinetics of polymeric nanoparticles, International journal of pharmaceutics 307(1) (2006) 93-102.

[91] T. Cedervall, I. Lynch, M. Foy, T. Berggård, S.C. Donnelly, G. Cagney, S. Linse, K.A. Dawson, Detailed identification of plasma proteins adsorbed on copolymer nanoparticles, Angewandte Chemie International Edition 46(30) (2007) 5754-5756.
[92] S.E. Gratton, P.A. Ropp, P.D. Pohlhaus, J.C. Luft, V.J. Madden, M.E. Napier, J.M. DeSimone, The effect of particle design on cellular internalization pathways, Proceedings of the national academy of sciences 105(33) (2008) 11613-11618.
[93] Q. Sun, X. Sun, X. Ma, Z. Zhou, E. Jin, B. Zhang, Y. Shen, E.A. Van Kirk, W.J. Murdoch, J.R. Lott, Integration of nanoassembly functions for an effective delivery cascade for cancer drugs, Adv. Mater 26(45) (2014) 7615-7621.
[94] Q. Sun, Z. Zhou, N. Qiu, Y. Shen, Rational design of cancer nanomedicine: nanoproperty integration and synchronization, Adv Mater 29(14) (2017) 1606628.
[95] A.K. Varkouhi, M. Scholte, G. Storm, H.J. Haisma, Endosomal escape pathways for delivery of biologicals, J Control Release 151(3) (2011) 220-228.
[96] J. Gilleron, W. Querbes, A. Zeigerer, A. Borodovsky, G. Marsico, U. Schubert, K. Manygoats, S. Seifert, C. Andree, M. Stöter, Image-based analysis of lipid nanoparticle–mediated siRNA delivery, intracellular trafficking and endosomal escape, Nature biotechnology 31(7) (2013) 638-646.
[97] M.P. Stewart, A. Sharei, X. Ding, G. Sahay, R. Langer, K.F. Jensen, In vitro and ex vivo strategies for intracellular delivery, Nature 538(7624) (2016) 183-192.
[98] P. Li, J. Liu, Micro (nano) plastics in the human body: sources, occurrences, fates, and health risks, Environmental Science & Technology 58(7) (2024) 3065-3078.
[99] T. Eberhard, G. Casillas, G.M. Zarus, D.B. Barr, Systematic review of microplastics and nanoplastics in indoor and outdoor air: identifying a framework and data needs for quantifying human inhalation exposures, Journal of exposure science & environmental epidemiology 34(2) (2024) 185-196.
[100] Y. Yu, N. Craig, L. Su, A hidden pathway for human exposure to micro-and nanoplastics—the mechanical fragmentation of plastic products during daily use, Toxics 11(9) (2023) 774.
[101] R. Dris, J. Gasperi, V. Rocher, M. Saad, N. Renault, B. Tassin, Microplastic contamination in an urban area: a case study in Greater Paris, Environmental Chemistry 12(5) (2015) 592-599.
[102] Q. Zhang, Y. Zhao, F. Du, H. Cai, G. Wang, H. Shi, Microplastic fallout in different indoor environments, Environmental science & technology 54(11) (2020) 6530-6539.

[103] T. Yang, J. Luo, B. Nowack, Characterization of nanoplastics, fibrils, and microplastics released during washing and abrasion of polyester textiles, Environmental Science & Technology 55(23) (2021) 15873-15881.
[104] Y. Li, J. Fu, L. Peng, X. Sun, G. Wang, Y. Wang, L. Chen, A sustainable emulsion for separation and Raman identification of microplastics and nanoplastics, Chemical Engineering Journal 469 (2023) 143992.
[105] Z. Lett, A. Hall, S. Skidmore, N.J. Alves, Environmental microplastic and nanoplastic: Exposure routes and effects on coagulation and the cardiovascular system, Environmental Pollution 291 (2021) 118190.
[106] N. Ali, J. Katsouli, E.L. Marczylo, T.W. Gant, S. Wright, J.B. De La Serna, The potential impacts of micro-and-nano plastics on various organ systems in humans, EBioMedicine 99 (2024).
[107] S. Shan, Y. Zhang, H. Zhao, T. Zeng, X. Zhao, Polystyrene nanoplastics penetrate across the blood-brain barrier and induce activation of microglia in the brain of mice, Chemosphere 298 (2022) 134261.
[108] L. Lu, Z. Wan, T. Luo, Z. Fu, Y. Jin, Polystyrene microplastics induce gut microbiota dysbiosis and hepatic lipid metabolism disorder in mice, Science of the total environment 631 (2018) 449-458.
[109] X. Zhao, J. Sun, L. Zhou, M. Teng, L. Zhao, Y. Li, F. Wu, Defining the size ranges of polystyrene nanoplastics according to their ability to cross biological barriers, Environmental Science: Nano 10(10) (2023) 2634-2645.
[110] Y. Qi, Y. Chen, T. Xia, I. Lynch, S. Liu, Extra-pulmonary translocation of exogenous ambient nanoparticles in the human body, Acs Nano 17(1) (2022) 12-19.
[111] Y. Qi, S. Wei, T. Xin, C. Huang, Y. Pu, J. Ma, C. Zhang, Y. Liu, I. Lynch, S. Liu, Passage of exogeneous fine particles from the lung into the brain in humans and animals, Proceedings of the National Academy of Sciences 119(26) (2022) e2117083119.
[112] H. Jin, C. Yang, C. Jiang, L. Li, M. Pan, D. Li, X. Han, J. Ding, Evaluation of neurotoxicity in BALB/c mice following chronic exposure to polystyrene microplastics, Environmental health perspectives 130(10) (2022) 107002.
[113] Y. Zhou, Q. Wu, Y. Li, Y. Feng, Y. Wang, W. Cheng, Low-dose of polystyrene microplastics induce cardiotoxicity in mice and human-originated cardiac organoids, Environment international 179 (2023) 108171.

[114] S. Li, Y. Ma, S. Ye, S. Tang, N. Liang, Y. Liang, F. Xiao, Polystyrene microplastics trigger hepatocyte apoptosis and abnormal glycolytic flux via ROS-driven calcium overload, Journal of hazardous materials 417 (2021) 126025.
[115] F. Barbosa, J.A. Adeyemi, M.Z. Bocato, A. Comas, A. Campiglia, A critical viewpoint on current issues, limitations, and future research needs on micro-and nanoplastic studies: From the detection to the toxicological assessment, Environmental Research 182 (2020) 109089.
[116] Y. Yan, F. Zhu, C. Zhu, Z. Chen, S. Liu, C. Wang, C. Gu, Dibutyl phthalate release from polyvinyl chloride microplastics: Influence of plastic properties and environmental factors, Water Research 204 (2021) 117597.
[117] A.L. Dawson, S. Kawaguchi, C.K. King, K.A. Townsend, R. King, W.M. Huston, S.M. Bengtson Nash, Turning microplastics into nanoplastics through digestive fragmentation by Antarctic krill, Nat Commun 9(1) (2018) 1001.
[118] R. Ruivo, C. Anne, C. Sagné, B. Gasnier, Molecular and cellular basis of lysosomal transmembrane protein dysfunction, Biochimica et Biophysica Acta (BBA)-Molecular Cell Research 1793(4) (2009) 636-649.
[119] A. Gricajeva, A.K. Nadda, R. Gudiukaite, Insights into polyester plastic biodegradation by carboxyl ester hydrolases, Journal of Chemical Technology & Biotechnology 97(2) (2022) 359-380.
[120] S. Maity, S. Banerjee, C. Biswas, R. Guchhait, A. Chatterjee, K. Pramanick, Functional interplay between plastic polymers and microbes: a comprehensive review, Biodegradation 32(5) (2021) 487-510.
[121] I. Vital-Vilchis, E. Karunakaran, Using Insect Larvae and Their Microbiota for Plastic Degradation, Insects 16(2) (2025) 165.
[122] R.M. Hernández, G. Orive, A. Murua, J.L. Pedraz, Microcapsules and microcarriers for in situ cell delivery, Adv Drug Deliver Rev 62(7-8) (2010) 711-730.
[123] J. Mu, J. Lin, P. Huang, X. Chen, Development of endogenous enzyme-responsive nanomaterials for theranostics, Chem Soc Rev 47(15) (2018) 5554-5573.
[124] E. Donath, G.B. Sukhorukov, F. Caruso, S.A. Davis, H. Möhwald, Novel hollow polymer shells by colloid-templated assembly of polyelectrolytes, Angewandte Chemie International Edition 37(16) (1998) 2201-2205.
[125] S. De Koker, R. Hoogenboom, B.G. De Geest, Polymeric multilayer capsules for drug delivery, Chem Soc Rev 41(7) (2012) 2867-2884.

[126] F. Caruso, K. Niikura, D.N. Furlong, Y. Okahata, Ultrathin multilayer polyelectrolyte films on gold: construction and thickness determination, Langmuir 13(13) (1997) 3422-3426.
[127] G. Sukhorukov, E. Donath, S. Moya, A. Susha, A. Voigt, J. Hartmann, H. Mohwald, Microencapsulation by means of step-wise adsorption of polyelectrolytes, Journal of Microencapsulation 17(2) (2000) 177-185.
[128] V. Vergaro, F. Scarlino, C. Bellomo, R. Rinaldi, D. Vergara, M. Maffia, F. Baldassarre, G. Giannelli, X. Zhang, Y.M. Lvov, Drug-loaded polyelectrolyte microcapsules for sustained targeting of cancer cells, Adv Drug Deliver Rev 63(9) (2011) 847-864.
[129] G. Decher, Fuzzy nanoassemblies: toward layered polymeric multicomposites, science 277(5330) (1997) 1232-1237.
[130] P.T. Hammond, Building biomedical materials layer-by-layer, Materials Today 15(5) (2012) 196-206.
[131] A.P. Johnston, C. Cortez, A.S. Angelatos, F. Caruso, Layer-by-layer engineered capsules and their applications, Current opinion in colloid & interface science 11(4) (2006) 203-209.
[132] P.F. Kiser, G. Wilson, D. Needham, Lipid-coated microgels for the triggered release of doxorubicin, J Control Release 68(1) (2000) 9-22.
[133] G.B. Sukhorukov, M. Brumen, E. Donath, H. Möhwald, Hollow polyelectrolyte shells: exclusion of polymers and donnan equilibrium, The Journal of Physical Chemistry B 103(31) (1999) 6434-6440.
[134] B.G. De Geest, C. Déjugnat, G.B. Sukhorukov, K. Braeckmans, S.C. De Smedt, J. Demeester, Self-rupturing microcapsules, Adv Mater 17(19) (2005) 2357-2360.
[135] C.S. Peyratout, L. Dähne, Tailor-made polyelectrolyte microcapsules: from multilayers to smart containers, Angewandte Chemie International Edition 43(29) (2004) 3762-3783.
[136] D.V. Volodkin, A.I. Petrov, M. Prevot, G.B. Sukhorukov, Matrix polyelectrolyte microcapsules: new system for macromolecule encapsulation, Langmuir 20(8) (2004) 3398-3406.
[137] F. Caruso, M. Spasova, A. Susha, M. Giersig, R.A. Caruso, Magnetic nanocomposite particles and hollow spheres constructed by a sequential layering approach, Chemistry of Materials 13(1) (2000) 109-116.

[138] V. Mamaeva, J.M. Rosenholm, L.T. Bate-Eya, L. Bergman, E. Peuhu, A. Duchanoy, L.E. Fortelius, S. Landor, D.M. Toivola, M. Lindén, Mesoporous silica nanoparticles as drug delivery systems for targeted inhibition of Notch signaling in cancer, Molecular Therapy 19(8) (2011) 1538-1546.
[139] W. Tong, X. Song, C. Gao, Layer-by-layer assembly of microcapsules and their biomedical applications, Chem Soc Rev 41(18) (2012) 6103-6124.
[140] M. Tsirigotis-Maniecka, L. Szyk-Warszyńska, Ł. Lamch, J. Weżgowiec, P. Warszyński, K.A. Wilk, Benefits of pH-responsive polyelectrolyte coatings for carboxymethyl cellulose-based microparticles in the controlled release of esculin, Materials Science and Engineering: C 118 (2021) 111397.
[141] T.A. Kolesnikova, A.G. Skirtach, H. Möhwald, Red blood cells and polyelectrolyte multilayer capsules: natural carriers versus polymer-based drug delivery vehicles, Expert opinion on drug delivery 10(1) (2013) 47-58.
[142] H. Zhu, S. Nawar, J.G. Werner, J. Liu, G. Huang, Y. Mei, D.A. Weitz, A.A. Solovev, Hydrogel micromotors with catalyst-containing liquid core and shell, Journal of Physics: Condensed Matter 31(21) (2019) 214004.
[143] J.J. Richardson, J. Cui, M. Bjornmalm, J.A. Braunger, H. Ejima, F. Caruso, Innovation in layer-by-layer assembly, Chemical reviews 116(23) (2016) 14828-14867.
[144] J. Li, B.V. Parakhonskiy, A.G. Skirtach, A decade of developing applications exploiting the properties of polyelectrolyte multilayer capsules, Chemical Communications 59(7) (2023) 807-835.
[145] A. Yashchenok, B. Parakhonskiy, S. Donatan, D. Kohler, A. Skirtach, H. Möhwald, Polyelectrolyte multilayer microcapsules templated on spherical, elliptical and square calcium carbonate particles, J Mater Chem B 1(9) (2013) 1223-1228.
[146] G. Acharya, C.S. Shin, M. McDermott, H. Mishra, H. Park, I.C. Kwon, K. Park, The hydrogel template method for fabrication of homogeneous nano/microparticles, J Control Release 141(3) (2010) 314-319.
[147] G.B. Sukhorukov, E. Donath, H. Lichtenfeld, E. Knippel, M. Knippel, A. Budde, H. Mohwald, Layer-by-layer self assembly of polyelectrolytes on colloidal particles, Colloids And Surfaces A-Physicochemical And Engineering Aspects 137(1-3) (1998) 253-266.
[148] G. Ibarz, L. Dähne, E. Donath, H. Möhwald, Smart micro-and nanocontainers for storage, transport, and release, Adv Mater 13(17) (2001) 1324-1327.

[149] T. Boudou, P. Kharkar, J. Jing, R. Guillot, I. Pignot-Paintrand, R. Auzely-Velty, C. Picart, Polyelectrolyte multilayer nanoshells with hydrophobic nanodomains for delivery of Paclitaxel, J Control Release 159(3) (2012) 403-412.
[150] S. De Koker, B.G. De Geest, C. Cuvelier, L. Ferdinande, W. Deckers, W.E. Hennink, S. De Smedt, N. Mertens, In vivo cellular uptake, degradation, and biocompatibility of polyelectrolyte microcapsules, Adv Funct Mater 17(18) (2007) 3754-3763.
[151] H. Ejima, J.J. Richardson, K. Liang, J.P. Best, M.P. van Koeverden, G.K. Such, J. Cui, F. Caruso, One-step assembly of coordination complexes for versatile film and particle engineering, Science 341(6142) (2013) 154-157.
[152] H. Wang, H. Liu, F. He, W. Chen, X. Zhang, M. Zhao, L. Wang, J. Qin, Flexible generation of multi-aqueous core hydrogel capsules using microfluidic aqueous two-phase system, Advanced Materials Technologies 5(6) (2020) 2000045.
[153] Y. Wu, X. Lin, Z. Wu, H. Möhwald, Q. He, Self-propelled polymer multilayer Janus capsules for effective drug delivery and light-triggered release, ACS applied materials & interfaces 6(13) (2014) 10476-10481.
[154] Y. Niu, X. Zhang, Y. Kang, P. Sun, H. Liu, Z. Xiao, D. Zhao, Magnetic microcapsules based on Fe3O4 nanoparticles: Preparation, properties, and applications, Materials Today Communications (2024) 108660.
[155] H. Gao, A.V. Sapelkin, M.M. Titirici, G.B. Sukhorukov, In situ synthesis of fluorescent carbon dots/polyelectrolyte nanocomposite microcapsules with reduced permeability and ultrasound sensitivity, Acs Nano 10(10) (2016) 9608-9615.
[156] X.Q. Liu, C. Picart, Layer-by-Layer assemblies for cancer treatment and diagnosis, Adv Mater 28(6) (2016) 1295-1301.
[157] W.-C. Liao, M. Riutin, W.J. Parak, I. Willner, Programmed pH-responsive microcapsules for the controlled release of CdSe/ZnS quantum dots, Acs Nano 10(9) (2016) 8683-8689.
[158] D. Zhu, L. Feng, N. Feliu, A.H. Guse, W.J. Parak, Stimulation of Local Cytosolic Calcium Release by Photothermal Heating for Studying Intra- and Intercellular Calcium Waves, Adv Mater 33(24) (2021) 2008261.
[159] S. Roy, D. Zhu, W.J. Parak, N. Feliu, Lysosomal proton buffering of poly (ethylenimine) measured in situ by fluorescent pH-sensor microcapsules, Acs Nano 14(7) (2020) 8012-8023.

[160] M. Rubart, Two-photon microscopy of cells and tissue, Circulation research 95(12) (2004) 1154-1166.
[161] P. Luu, S.E. Fraser, F. Schneider, More than double the fun with two-photon excitation microscopy, Communications biology 7(1) (2024) 364.
[162] W. Denk, J.H. Strickler, W.W. Webb, Two-photon laser scanning fluorescence microscopy, Science 248(4951) (1990) 73-76.
[163] F. Helmchen, W. Denk, Deep tissue two-photon microscopy, Nature methods 2(12) (2005) 932-940.
[164] K. Svoboda, R. Yasuda, Principles of two-photon excitation microscopy and its applications to neuroscience, Neuron 50(6) (2006) 823-839.
[165] U.K. Tirlapur, K. König, Targeted transfection by femtosecond laser, Nature 418(6895) (2002) 290-291.
[166] A. Hopt, E. Neher, Highly nonlinear photodamage in two-photon fluorescence microscopy, Biophysical journal 80(4) (2001) 2029-2036.
[167] W.R. Zipfel, R.M. Williams, R. Christie, A.Y. Nikitin, B.T. Hyman, W.W. Webb, Live tissue intrinsic emission microscopy using multiphoton-excited native fluorescence and second harmonic generation, Proceedings of the National Academy of Sciences 100(12) (2003) 7075-7080.
[168] G.H. Patterson, D.W. Piston, Photobleaching in two-photon excitation microscopy, Biophysical journal 78(4) (2000) 2159-2162.
[169] V.E. Centonze, J.G. White, Multiphoton excitation provides optical sections from deeper within scattering specimens than confocal imaging, Biophysical journal 75(4) (1998) 2015-2024.
[170] A. Dvornikov, L. Malacrida, E. Gratton, The DIVER microscope for imaging in scattering media, Methods and protocols 2(2) (2019) 53.
[171] V. Crosignani, A. Dvornikov, J.S. Aguilar, C. Stringari, R. Edwards, W.W. Mantulin, E. Gratton, Deep tissue fluorescence imaging and in vivo biological applications, Journal of biomedical optics 17(11) (2012) 116023-116023.
[172] F. Jia, X.P. Liu, L.H. Li, S. Mallapragada, B. Narasimhan, Q. Wang, Multifunctional nanoparticles for targeted delivery of immune activating and cancer therapeutic agents, J Control Release 172(3) (2013) 1020-1034.

[173] J. Cao, D. Huang, N.A. Peppas, Advanced engineered nanoparticulate platforms to address key biological barriers for delivering chemotherapeutic agents to target sites, Adv Drug Deliver Rev 167 (2020) 170-188.
[174] M.S. de Almeida, E. Susnik, B. Drasler, P. Taladriz-Blanco, A. Petri-Fink, B. Rothen-Rutishauser, Understanding nanoparticle endocytosis to improve targeting strategies in nanomedicine, Chem Soc Rev 50(9) (2021) 5397-5434.
[175] L. Wang, S. Quine, A.N. Frickenstein, M.C. Lee, W. Yang, V.M. Sheth, M.D. Bourlon, Y.X. He, S. Lyu, L. Garcia-Contreras, Y.D. Zhao, S. Wilhelm, Exploring and Analyzing the Systemic Delivery Barriers for Nanoparticles, Adv Funct Mater (2023).
[176] P. Makvandi, M.L. Chen, R. Sartorius, A. Zarrabi, M. Ashrafizadeh, F.D. Moghaddam, J.Z. Ma, V. Mattoli, F.R. Tay, Endocytosis of abiotic nanomaterials and nanobiovectors: Inhibition of membrane trafficking, Nano Today 40 (2021).
[177] N. Brkovic, L. Zhang, J.N. Peters, S. Kleine-Doepke, W.J. Parak, D. Zhu, Quantitative Assessment of Endosomal Escape of Various Endocytosed Polymer-Encapsulated Molecular Cargos upon Photothermal Heating, Small 16(46) (2020) 2003639.
[178] Z.X. Zhou, X.R. Liu, D.C. Zhu, Y. Wang, Z. Zhang, X.F. Zhou, N.S. Qiu, X.S. Chen, Y.Q. Shen, Nonviral cancer gene therapy: Delivery cascade and vector nanoproperty integration, Adv Drug Deliver Rev 115 (2017) 115-154.
[179] K.I. Cupic, J.J. Rennick, A.P.R. Johnston, G.K. Such, Controlling endosomal escape using nanoparticle composition: current progress and future perspectives, Nanomedicine-Uk 14(2) (2019) 215-223.
[180] F. Ledesma, B. Ozcan, X.Q. Sun, S.M. Medina, M.P. Landry, Nanomaterial Strategies for Delivery of Therapeutic Cargoes, Adv Funct Mater 32(4) (2022).
[181] J.J. Rennick, A.P.R. Johnston, R.G. Parton, Key principles and methods for studying the endocytosis of biological and nanoparticle therapeutics, Nat Nanotechnol 16(3) (2021) 266-276.
[182] S. Narum, B. Deal, H. Ogasawara, J.N. Mancuso, J.H. Zhang, K. Salaita, An Endosomal Escape Trojan Horse Platform to Improve Cytosolic Delivery of Nucleic Acids, Acs Nano 18(8) (2024) 6186-6201.
[183] S.L.Y. Teo, J.J. Rennick, D. Yuen, H. Al-Wassiti, A.P.R. Johnston, C.W. Pouton, Unravelling cytosolic delivery of cell penetrating peptides with a quantitative endosomal escape assay, Nat Commun 12(1) (2021).

[184] P. Niekamp, F. Scharte, T. Sokoya, L. Vittadello, Y. Kim, Y.Q. Deng, E. Südhoff, A. Hilderink, M. Imlau, C.J. Clarke, M. Hensel, C.G. Burd, J.C.M. Holthuis, Ca-activated sphingomyelin scrambling and turnover mediate ESCRT-independent lysosomal repair, Nat Commun 13(1) (2022).
[185] Y.R. Jia, X.G. Wang, L.W. Li, F.Z. Li, J.C. Zhang, X.J. Liang, Lipid Nanoparticles Optimized for Targeting and Release of Nucleic Acid, Adv Mater 36(4) (2024).
[186] H. Ma, F. Xing, Y.X. Zhou, P.Y. Yu, R. Luo, J.W. Xu, Z. Xiang, P.M. Rommens, X. Duan, U. Ritz, Design and fabrication of intracellular therapeutic cargo delivery systems based on nanomaterials: current status and future perspectives, J Mater Chem B (2023).
[187] W. He, X.Y. Xing, X.L. Wang, D. Wu, W. Wu, J.L. Guo, S. Mitragotri, Nanocarrier-Mediated Cytosolic Delivery of Biopharmaceuticals, Adv Funct Mater 30(37) (2020).
[188] C.E. Probst, P. Zrazhevskiy, V. Bagalkot, X.H. Gao, Quantum dots as a platform for nanoparticle drug delivery vehicle design, Adv Drug Deliver Rev 65(5) (2013) 703-718.
[189] T.F. Martens, K. Remaut, J. Demeester, S.C. De Smedt, K. Braeckmans, Intracellular delivery of nanomaterials: How to catch endosomal escape in the act, Nano Today 9(3) (2014) 344-364.
[190] S. Puri, M. Mazza, G. Roy, R.M. England, L.P. Zhou, S. Nourian, J.A. Subramony, Evolution of nanomedicine formulations for targeted delivery and controlled release, Adv Drug Deliver Rev 200 (2023).
[191] S. Zhao, F. Caruso, L. Dähne, G. Decher, B.G. De Geest, J. Fan, N. Feliu, Y. Gogotsi, P.T. Hammond, M.C. Hersam, A. Khademhosseini, N. Kotov, S. Leporatti, Y. Li, F. Lisdat, L.M. Liz-Marzán, S. Moya, P. Mulvaney, A.L. Rogach, S. Roy, D.G. Shchukin, A.G. Skirtach, M.M. Stevens, G.B. Sukhorukov, P.S. Weiss, Z. Yue, D. Zhu, W.J. Parak, The Future of Layer-by-Layer Assembly: A Tribute to ACS Nano Associate Editor Helmuth Möhwald, Acs Nano 13(6) (2019) 6151-6169.
[192] X.R. Wang, W.X. Wang, Cellular journey of nanomaterials: Theories, trafficking, and kinetics, Aggregate 4(6) (2023).
[193] Q. Dai, C. Walkey, W.C.W. Chan, Polyethylene Glycol Backfilling Mitigates the Negative Impact of the Protein Corona on Nanoparticle Cell Targeting, Angew Chem Int Edit 53(20) (2014) 5093-5096.

[194] H.-H. Deng, X.-Q. Shi, F.-F. Wang, H.-P. Peng, A.-L. Liu, X.-H. Xia, W. Chen, Fabrication of Water-Soluble, Green-Emitting Gold Nanoclusters with a 65% Photoluminescence Quantum Yield via Host–Guest Recognition, Chemistry of Materials 29(3) (2017) 1362-1369.
[195] G. Pramanik, A. Keprova, J. Valenta, V. Bocan, K. Kvaková, L. Libusova, P. Cigler, Synthesis of Near-Infrared Emitting Gold Nanoclusters for Biological Applications, Jove-J Vis Exp (157) (2020).
[196] M. Rafipoor, C. Schmidtke, C. Wolter, C. Strelow, H. Weller, H. Lange, Clustering of CdSe/CdS Quantum Dot/Quantum Rods into Micelles Can Form Bright, Non-blinking, Stable, and Biocompatible Probes, Langmuir 31(34) (2015) 9441-9447.
[197] A. Feld, R. Koll, L.S. Fruhner, M. Krutyeva, W. Pyckhout-Hintzen, C. Weiss, H. Heller, A. Weimer, C. Schmidtke, M.S. Appavou, E. Kentzinger, J. Allgaier, H. Weller, Nanocomposites of Highly Monodisperse Encapsulated Superparamagnetic Iron Oxide Nanocrystals Homogeneously Dispersed in a Poly(ethylene Oxide) Melt, Acs Nano 11(4) (2017) 3767-3775.
[198] M. Rafipoor, R. Koll, J.P. Merkl, L.S. Fruhner, H. Weller, H. Lange, Resonant Energy Transfer can Trigger Multiexciton Recombination in Dense Quantum Dot Ensembles, Small 15(5) (2019) e1803798.
[199] H.K. Yuan, C.G. Khoury, H. Hwang, C.M. Wilson, G.A. Grant, T. Vo-Dinh, Gold nanostars: surfactant-free synthesis, 3D modelling, and two-photon photoluminescence imaging, Nanotechnology 23(7) (2012).
[200] M.J. Abraham, T. Murtola, R. Schulz, S. Páll, J.C. Smith, B. Hess, E. Lindahl, GROMACS: High performance molecular simulations through multi-level parallelism from laptops to supercomputers, SoftwareX 1 (2015) 19-25.
[201] M. Zgarbová, J. Sponer, M. Otyepka, T.E. Cheatham, R. Galindo-Murillo, P. Jurecka, Refinement of the Sugar-Phosphate Backbone Torsion Beta for AMBER Force Fields Improves the Description of Z- and B-DNA, J Chem Theory Comput 11(12) (2015) 5723-5736.
[202] W. Humphrey, A. Dalke, K. Schulten, VMD: Visual molecular dynamics, J Mol Graph Model 14(1) (1996) 33-38.
[203] L. Martínez, R. Andrade, E.G. Birgin, J.M. Martínez, PACKMOL: A Package for Building Initial Configurations for Molecular Dynamics Simulations, J Comput Chem 30(13) (2009) 2157-2164.

[204] M. Ochs, S. Carregal-Romero, J. Rejman, K. Braeckmans, S.C. De Smedt, W.J. Parak, Light-Addressable Capsules as Caged Compound Matrix for Controlled Triggering of Cytosolic Reactions, Angew Chem Int Edit 52(2) (2013) 695-699.
[205] J. Schindelin, I. Arganda-Carreras, E. Frise, V. Kaynig, M. Longair, T. Pietzsch, S. Preibisch, C. Rueden, S. Saalfeld, B. Schmid, Fiji: an open-source platform for biological-image analysis, Nature methods 9(7) (2012) 676-682.
[206] E.A. Mun, C. Hannell, S.E. Rogers, P. Hole, A.C. Williams, V.V. Khutoryanskiy, On the role of specific interactions in the diffusion of nanoparticles in aqueous polymer solutions, Langmuir 30(1) (2014) 308-317.
[207] D.M. Mitrano, P. Wick, B. Nowack, Placing nanoplastics in the context of global plastic pollution, Nature Nanotechnology 16(5) (2021) 491-500.
[208] L.H. Nguyen, B.-S. Nguyen, D.-T. Le, T.S. Alomar, N. AlMasoud, S. Ghotekar, R. Oza, P. Raizada, P. Singh, V.-H. Nguyen, A concept for the biotechnological minimizing of emerging plastics, micro-and nano-plastics pollutants from the environment: A review, Environmental Research 216 (2023) 114342.
[209] J.C. Prata, J.P. da Costa, I. Lopes, A.L. Andrady, A.C. Duarte, T. Rocha-Santos, A One Health perspective of the impacts of microplastics on animal, human and environmental health, Science of the Total Environment 777 (2021) 146094.
[210] A.D. Vethaak, J. Legler, Microplastics and human health, Science 371(6530) (2021) 672-674.
[211] E. Winiarska, M. Jutel, M. Zemelka-Wiacek, The potential impact of nano-and microplastics on human health: Understanding human health risks, Environmental Research (2024) 118535.
[212] P. Shieh, W. Zhang, K.E. Husted, S.L. Kristufek, B. Xiong, D.J. Lundberg, J. Lem, D. Veysset, Y. Sun, K.A. Nelson, Cleavable comonomers enable degradable, recyclable thermoset plastics, Nature 583(7817) (2020) 542-547.
[213] L. Wimberger, G. Ng, C. Boyer, Light-driven polymer recycling to monomers and small molecules, Nature Communications 15(1) (2024) 2510.
[214] S.Y. Choi, Y. Lee, H.E. Yu, I.J. Cho, M. Kang, S.Y. Lee, Sustainable production and degradation of plastics using microbes, Nature Microbiology 8(12) (2023) 2253-2276.
[215] N. Mohanan, Z. Montazer, P.K. Sharma, D.B. Levin, Microbial and enzymatic degradation of synthetic plastics, Frontiers in Microbiology 11 (2020) 580709.

[216] M. Spínola-Amilibia, R. Illanes-Vicioso, E. Ruiz-López, P. Colomer-Vidal, F. Rodriguez-Ventura, R. Peces Pérez, C.F. Arias, T. Torroba, M. Solà, E. Arias-Palomo, Plastic degradation by insect hexamerins: Near-atomic resolution structures of the polyethylene-degrading proteins from the wax worm saliva, Science Advances 9(38) (2023) eadi6813.
[217] S. Yoshida, K. Hiraga, T. Takehana, I. Taniguchi, H. Yamaji, Y. Maeda, K. Toyohara, K. Miyamoto, Y. Kimura, K. Oda, A bacterium that degrades and assimilates poly (ethylene terephthalate), Science 351(6278) (2016) 1196-1199.
[218] V. Tournier, S. Duquesne, F. Guillamot, H. Cramail, D. Taton, A. Marty, I. André, Enzymes' power for plastics degradation, Chemical Reviews 123(9) (2023) 5612-5701.
[219] Q. Liu, Y. Chen, Z. Chen, F. Yang, Y. Xie, W. Yao, Current status of microplastics and nanoplastics removal methods: Summary, comparison and prospect, Science of The Total Environment 851 (2022) 157991.
[220] N. Singh, N. Khandelwal, R. Nakajima, A.K. Stoddart, G.A. Gagnon, Nanoplastic mitigation technologies: challenges and sustainability considerations, Current Opinion in Chemical Engineering 48 (2025) 101107.
[221] M.-K. Nguyen, Plastic Waste as a Challenge Cannot Be Ignored: Characteristics, Sources, Impacts, and Unveiling Potential Solutions through Photocatalysis for Environmental Sustainability, Plastic Degradation and Conversion by Photocatalysis (Volume 2): From Waste to Wealth, ACS Publications2024, pp. 249-265.
[222] G. Nie, K. Hu, W. Ren, P. Zhou, X. Duan, L. Xiao, S. Wang, Mechanical agitation accelerated ultrasonication for wastewater treatment: Sustainable production of hydroxyl radicals, Water Research 198 (2021) 117124.
[223] Q. Zhou, Y. Liu, G. Yu, F. He, K. Chen, D. Xiao, X. Zhao, Y. Feng, J. Li, Degradation kinetics of sodium alginate via sono-Fenton, photo-Fenton and sono-photo-Fenton methods in the presence of TiO2 nanoparticles, Polymer degradation and stability 135 (2017) 111-120.
[224] X. Chen, D. Sun-Waterhouse, W. Yao, X. Li, M. Zhao, L. You, Free radical-mediated degradation of polysaccharides: Mechanism of free radical formation and degradation, influence factors and product properties, Food Chemistry 365 (2021) 130524.
[225] R.A. Sheldon, J.M. Woodley, Role of biocatalysis in sustainable chemistry, Chemical reviews 118(2) (2018) 801-838.

[226] C.O. Okoye, C.I. Addey, O. Oderinde, J.O. Okoro, J.Y. Uwamungu, C.K. Ikechukwu, E.S. Okeke, O. Ejeromedoghene, E.C. Odii, Toxic chemicals and persistent organic pollutants associated with micro-and nanoplastics pollution, Chemical Engineering Journal Advances 11 (2022) 100310.
[227] A. Saravanan, P.S. Kumar, D.-V.N. Vo, S. Jeevanantham, S. Karishma, P. Yaashikaa, A review on catalytic-enzyme degradation of toxic environmental pollutants: Microbial enzymes, Journal of Hazardous Materials 419 (2021) 126451.
[228] P. Demarche, C. Junghanns, R.R. Nair, S.N. Agathos, Harnessing the power of enzymes for environmental stewardship, Biotechnology Advances 30(5) (2012) 933-953.
[229] R.R. Klauer, D.A. Hansen, D. Wu, L.M.O. Monteiro, K.V. Solomon, M.A. Blenner, Biological upcycling of plastics waste, Annual Review of Chemical and Biomolecular Engineering 15 (2024).
[230] L.M. Johnson, J.B. Mecham, S.A. Krovi, M.M.M. Caffaro, S. Aravamudhan, A.L. Kovach, T.R. Fennell, N.P. Mortensen, Fabrication of polyethylene terephthalate (PET) nanoparticles with fluorescent tracers for studies in mammalian cells, Nanoscale Advances 3(2) (2021) 339-346.
[231] B.V. Parakhonskiy, W.J. Parak, D. Volodkin, A.G. Skirtach, Hybrids of Polymeric Capsules, Lipids, and Nanoparticles: Thermodynamics and Temperature Rise at the Nanoscale and Emerging Applications, Langmuir 35 (2019) 8574−8583.
[232] Y. Wang, A.S. Angelatos, F. Caruso, Template synthesis of nanostructured materials via layer-by-layer assembly, Chemistry Of Materials 20(3) (2008) 848-858.
[233] M.R. Chaves, M.L. Lima, L. Malafatti-Picca, D.A. De Angelis, A.M.d. Castro, É. Valoni, A.J. Marsaioli, A practical fluorescence-based screening protocol for polyethylene terephthalate degrading microorganisms, Journal of the Brazilian Chemical Society 29(6) (2018) 1278-1285.
[234] L. Pfaff, D. Breite, C.P. Badenhorst, U.T. Bornscheuer, R. Wei, Fluorimetric high-throughput screening method for polyester hydrolase activity using polyethylene terephthalate nanoparticles, Methods in enzymology, Elsevier2021, pp. 253-270.
[235] R.J. Müller, H. Schrader, J. Profe, K. Dresler, W.D. Deckwer, Enzymatic degradation of poly (ethylene terephthalate): rapid hydrolyse using a hydrolase from T. fusca, Macromolecular rapid communications 26(17) (2005) 1400-1405.

[236] I. Taniguchi, S. Yoshida, K. Hiraga, K. Miyamoto, Y. Kimura, K. Oda, Biodegradation of PET: current status and application aspects, Acs Catalysis 9(5) (2019) 4089-4105.
[237] H. Zhang, R.F. Dierkes, P. Perez-Garcia, E. Costanzi, J. Dittrich, P.A. Cea, M. Gurschke, V. Applegate, K. Partus, C. Schmeisser, The metagenome-derived esterase PET40 is highly promiscuous and hydrolyses polyethylene terephthalate (PET), The FEBS Journal 291(1) (2024) 70-91.
[238] C. Fang, N. Bhattarai, C. Sun, M. Zhang, Functionalized nanoparticles with long-term stability in biological media, Small (Weinheim an der Bergstrasse, Germany) 5(14) (2009) 1637.
[239] T.L. Moore, L. Rodriguez-Lorenzo, V. Hirsch, S. Balog, D. Urban, C. Jud, B. Rothen-Rutishauser, M. Lattuada, A. Petri-Fink, Nanoparticle colloidal stability in cell culture media and impact on cellular interactions, Chem Soc Rev 44(17) (2015) 6287-305.
[240] A.T. Jones, M. Gumbleton, R. Duncan, Understanding endocytic pathways and intracellular trafficking: a prerequisite for effective design of advanced drug delivery systems, Adv Drug Deliver Rev 55(11) (2003) 1353-1357.
[241] D. Zhu, S. Roy, Z. Liu, H. Weller, W. Parak, N. Feliu, Remotely controlled opening of delivery vehicles and release of cargo by external triggers, Adv Drug Deliver Rev 138 (2019) 117-132.
[242] C. Kirchner, A.M. Javier, A.S. Susha, A.L. Rogach, O. Kreft, G.B. Sukhorukov, W.J. Parak, Cytotoxicity of nanoparticle-loaded polymer capsules, Talanta 67 (2005) 486-491.
[243] Z. Liu, A. Escudero, C. Carrillo-Carrion, I. Chakraborty, D. Zhu, M. Gallego, W.J. Parak, N. Feliu, Biodegradation of Bi-Labeled Polymer-Coated Rare-Earth Nanoparticles in Adherent Cell Cultures, Chemistry of Materials 32 (2020) 245-254.
[244] Z. Liu, A. Zimpel, U. Lächelt, M. Pozzi, M.G. Gonzalez, I. Chakraborty, S. Wuttke, N. Feliu, W.J. Parak, Uptake and Intracellular Fate of Fluorophore Labeled Metal–Organic-Framework (MOF) Nanoparticles, Environment & Health 1 (2023) 270–277.
[245] X. Sun, M. Gamal, P. Nold, A. Said, I. Chakraborty, B. Pelaz, F. Schmied, K.v. Pückler, J. Figiel, Y. Zhao, C. Brendel, M. Hassan, W.J. Parak, N. Feliu, Tracking stem cells and macrophages with gold and iron oxide nanoparticles – The choice of the best suited particles, Applied Materials Today 15 (2019) 267-279.

[246] Y. Kang, L.M. Nack, Y. Liu, B. Qi, Y. Huang, Z. Liu, I. Chakraborty, F. Schulz, A.A.A. Ahmed, M.C. Poveda, F. Hafizi, S. Roy, M. Mutas, M. Holzapfel, C. Sanchez-Cano, K.D. Wegner, N. Feliu, W.J. Parak, Quantitative considerations about the size dependence of cellular entry and excretion of colloidal nanoparticles for different cell types, ChemTexts 8 (2022) 9.

[247] M. Djapovic, D. Milivojevic, T. Ilic-Tomic, M. Lješević, E. Nikolaivits, E. Topakas, V. Maslak, J. Nikodinovic-Runic, Synthesis and characterization of polyethylene terephthalate (PET) precursors and potential degradation products: Toxicity study and application in discovery of novel PETases, Chemosphere 275 (2021) 130005.